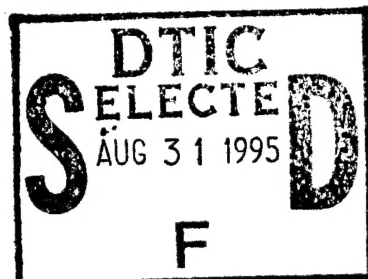


NAVAL POSTGRADUATE SCHOOL

Monterey, California



"Original contains color plates: All DTIC reproductions will be in black and white."

DISSERTATION

KINEMATICS AND DYNAMICS OF A CYCLONIC
EDDY OFF PT. ARENA, CALIFORNIA

by

Rogério Paulo Antunes Chumbinho

December 1994

Thesis Advisor:

Robert L. Haney

Approved for public release; distribution is unlimited

19950830 055

DTIC QUALITY INSPECTED 5

REPORT DOCUMENTATION PAGE

**Form Approved
OMB No. 0704-0188**

Public reporting burden for this collection of information is estimated to average 1 hour per response, including the time for reviewing instructions, searching existing data sources, gathering and maintaining the data needed, and completing and reviewing the collection of information. Send comments regarding this burden estimate or any other aspect of this collection of information, including suggestions for reducing this burden, to Washington Headquarters Services, Directorate for Information Operations and Reports, 1215 Jefferson Davis Highway, Suite 1204, Arlington, VA 22202-4302, and to the Office of Management and Budget, Paperwork Reduction Project (0704-0188), Washington, DC 20503.

1. AGENCY USE ONLY (Leave blank)		2. REPORT DATE December 1994		3. REPORT TYPE AND DATES COVERED Doctoral Dissertation	
4. TITLE AND SUBTITLE KINEMATICS AND DYNAMICS OF A CYCLONIC EDDY OFF Pt. ARENA, CALIFORNIA			5. FUNDING NUMBERS		
6. AUTHOR(S) Rogério Paulo Antunes Chumbinho			8. PERFORMING ORGANIZATION REPORT NUMBER		
7. PERFORMING ORGANIZATION NAME(S) AND ADDRESS(ES) Naval Postgraduate School Monterey, CA 93943-5000			10. SPONSORING/MONITORING AGENCY REPORT NUMBER		
9. SPONSORING/MONITORING AGENCY NAME(S) AND ADDRESSE(S)			12b. DISTRIBUTION CODE		
11. SUPPLEMENTARY NOTES The views expressed in this thesis are those of the author and do not reflect the official policy or position of the Department of Defense or the U.S. Government.			12a. DISTRIBUTION/AVAILABILITY STATEMENT Approved for public release; distribution is unlimited		
13. ABSTRACT (maximum 200 words) In situ hydrographic data and remotely sensed sea surface temperature data were analyzed to describe the kinematics and dynamics of a cyclonic eddy observed off Point Arena, California, in May 1993. The hydrographic data were first objectively analyzed using multiquadric-biharmonic interpolation (MQ-B) to obtain a three-dimensional field of density. This was then used in a primitive equation (PE) model with a digital filter initialization method to arrive at the dynamically balanced three-dimensional velocity field, including the vertical motion. Several aspects related to geostrophic adjustment, to data analysis and to the lack of exact synopticity in the observations were examined; these include the effects of internal tides, eddy rotation and MQ-B parameters sensitivity analysis. The results reveal a cyclonic circulation with meanders in the otherwise nearly circular flow, and maximum horizontal speeds of about 40–50 cm/s at the surface. The meanders have associated patterns of radially aligned patches of sinking and rising motion, extending coherently to about 500 m depth, with maximum vertical velocities of 20–22 m/day between 100 and 150 m depth. Because of the strong horizontal currents and the short horizontal length scales involved, the particle vertical excursions are very small.					
14. SUBJECT TERMS Vertical Velocity, Primitive Equation Modeling, Digital Filter Initialization, Quasigeostrophic Theory, Omega Equation, Multiquadric-Biharmonic Interpolation.			15. NUMBER OF PAGES 98		
16. PRICE CODE					
17. SECURITY CLASSIFICATION OF REPORT Unclassified		18. SECURITY CLASSIFICATION OF THIS PAGE Unclassified		19. SECURITY CLASSIFICATION OF ABSTRACT Unclassified	
19. LIMITATION OF ABSTRACT UL					

UNCLASSIFIED

SECURITY CLASSIFICATION OF THIS PAGE

13. ABSTRACT (continued)

The vertical motion in the domain was also diagnosed from the analyzed density field using the quasigeostrophic (QG) omega equation. The resulting vertical velocities are in good agreement with those from the initialized PE model except that the QG values were about 30 percent stronger in magnitude. These discrepancies were shown to be caused by the neglect of ageostrophic advection in the QG system.

Accesion For	
NTIS	CRA&I
DTIC	TAB
Unannounced	
Justification	
By	
Distribution /	
Availability Codes	
Dist	Avail and/or Special
A-1	

Approved for public release; distribution is unlimited

KINEMATICS AND DYNAMICS OF A CYCLONIC EDDY
OFF PT. ARENA, CALIFORNIA

Rogério Paulo Antunes Chumbinho
Lieutenant, Portuguese Navy
M.S., Naval Postgraduate School, 1993

DOCTOR OF PHILOSOPHY IN PHYSICAL OCEANOGRAPHY

from the

NAVAL POSTGRADUATE SCHOOL
December 1994

Author:

Rogério P. Antunes Chumbinho

Rogério Paulo Antunes Chumbinho

Approved by:

Roland W. Garwood, Jr.

Roland W. Garwood, Jr.
Committee Chairman

Newell Garfield

Newell Garfield
Professor of Oceanography

Peter C. Chu

Peter C. Chu
Professor of Oceanography

Steven R. Ramp

Steven R. Ramp
Professor of Oceanography

Charles W. Therrien

Charles W. Therrien
Professor of Elec. Engineering

Robert L. Haney

Robert L. Haney
Professor of Meteorology
Dissertation Supervisor

Approved by:

Robert H. Bourke

Robert H. Bourke, Chairman, Department of Oceanography

Approved by:

Richard S. Elster

Richard S. Elster, Dean of Instruction

ABSTRACT

In situ hydrographic data and remotely sensed sea surface temperature data were analyzed to describe the kinematics and dynamics of a cyclonic eddy observed off Point Arena, California, in May 1993. The hydrographic data were first objectively analyzed using multiquadric-biharmonic interpolation (MQ-B) to obtain a three-dimensional field of density. This was then used in a primitive equation (PE) model with a digital filter initialization method to arrive at the dynamically balanced three-dimensional velocity field, including the vertical motion. Several aspects related to geostrophic adjustment, to data analysis and to the lack of exact synopticity in the observations were examined; these include the effects of internal tides, eddy rotation and MQ-B parameters sensitivity analysis.

The results reveal a cyclonic circulation with meanders in the otherwise nearly circular flow, and maximum horizontal speeds of about 40–50 cm/s at the surface. The meanders have associated patterns of radially aligned patches of sinking and rising motion, extending coherently to about 500 m depth, with maximum vertical velocities of 20–22 m/day between 100 and 150 m depth. Because of the strong horizontal currents and the short horizontal length scales involved, the particle vertical excursions are very small.

The vertical motion in the domain was also diagnosed from the analyzed density field using the quasigeostrophic (QG) omega equation. The resulting vertical velocities are in good agreement with those from the initialized PE model except that the QG values were about 30 percent stronger in magnitude. These discrepancies were shown to be caused by the neglect of ageostrophic advection in the QG system.

The views expressed in this dissertation are those of the author and do not reflect the official policy or position of the Department of Defense or the U. S. Government.

TABLE OF CONTENTS

I. INTRODUCTION	1
II. DATA.....	5
A. DATA DESCRIPTION	5
1. Satellite imagery	5
2. Hydrographic data	7
B. DATA ANALYSIS.....	11
1. Multiquadric–biharmonic interpolation method.....	12
2. Data interpolation	15
a. Temperature interpolation	15
b. Salinity interpolation	17
3. Analyzed three-dimensional density field	18
III. METHODS	19
A. CIRCULATION MODEL	19
1. Description	19
2. Initial conditions	20
3. Boundary conditions.....	21
4. Digital filter initialization	23
B. QUASIGEOSTROPHIC OMEGA EQUATION.....	26
IV. RESULTS AND DISCUSSION.....	31
A. CIRCULATION MODEL RESULTS.....	31
1. Horizontal and vertical velocity	31
2. Geostrophic adjustment.....	40
3. Data related problems.....	49
a. Internal tides	50

b. Eddy rotation	56
c. Interpolation parameters	59
B. QUASIGEOSTROPHIC OMEGA EQUATION RESULTS	60
V. CONCLUSIONS.....	71
LIST OF REFERENCES.....	75
INITIAL DISTRIBUTION LIST	81

LIST OF FIGURES

1. National Oceanic and Atmospheric Administration (NOAA) Satellite Image, Obtained From Channel 4 of the Advanced Very High Resolution Radiometer (AVHRR), of the Sea Surface Temperature (SST) off Point Arena, on 22 May 1993, 23 GMT.	6
2. Position and Number of CTD Stations.	9
3. Wind Direction and Speed During May, 1993 off Pt. Arena.	10
4. Schematic Representation of the 2-D Temperature Interpolation at Each Level.	17
5. Example of the DFI Procedure Applied to a Typical Vertical Velocity Time Series...	24
6. Frequency Response of a Lowpass Filter With Cutoff Period 24 h, Sampling Period 300 s (Lanczos window).	25
7. Horizontal Cross Section of the Dynamically Balanced Horizontal Velocity Field at a Depth of 100 m.	32
8. Horizontal Cross Section of the Dynamically Balanced Horizontal Velocity Field at a Depth of 100 m, With Superimposed ADCP Horizontal Velocities.	34
9. Horizontal Cross Section of the Dynamically Balanced Vertical Velocity Field at a Depth of 100 m.	35
10. Meandering Jet With Alternating Patterns of Negative and Positive Vorticity.....	36
11. Vertical Cross Section of the Dynamically Balanced Vertical Velocity in the Along-shore Direction.....	38
12. Vertical Cross Section of the Dynamically Balanced Vertical Velocity in the Across Shore Direction.	39
13. Relation Between the Mass and Velocity Fields During the Geostrophic Adjustment, According to the Length Scale.....	42
14. Normalized Modal Shapes for Vertical Velocity From the Mean Stratification.	44
15. Same as Figure 9, but Obtained With an Initial Velocity Field With No Vertical Shear.	46

16. Same as Figure 11, but Obtained With an Initial Velocity Field With No Vertical shear.....	47
17. Same as Figure 12, but Obtained With an Initial Velocity Field With No Vertical shear.....	48
18. Cumulative Time Interval Between CTD Stations.....	50
19. Predicted Sea Level at the San Francisco Bay Entrance, for May 1993.....	52
20. Alongshore Vertical Cross Section of Temperature (°C) From Raw CTD Data.....	53
21. Relationship Between the Phase and Group Velocities and the Velocity Vector in a Propagating Internal Wave.	54
22. Field of Q -vectors Computed From the Analyzed Density Field in Part of the Domain, at 100 m.	62
23. Horizontal Cross Section of the Quasigeostrophic Vertical Velocity Field at 100 m Depth.....	64
24. Same as Figure 23, but Obtained From the Dynamically Balanced (DFI) Density Field.	65
25. Field of Ageostrophic Velocity Vectors at 100 m Depth, For the Same Part of the Domain as in Figure 22.....	67
26. Vertical Cross Section of the Quasigeostrophic Vertical Velocity Field in the Alongshore Direction.....	69
27. Vertical Cross Section of the Quasigeostrophic Vertical Velocity Field in the Across Shore Direction.	70

ACKNOWLEDGEMENTS

I wish to express my appreciation to the persons who, at some point during this study, added insight into the current research through their valuable comments or other help. Therefore, I am thankful to Dr. Steven Ramp (ONR), for making the hydrographic data available for this study; to Dr. Wendell Nuss (NPS) for providing the code that served as a basis for the three-dimensional multiquadric-biharmonic (MQ-B) interpolation code that was developed here; to Dr. Supachai (Pom) Sirayanone (NPS, visiting) for the many helpful comments on the MQ-B interpolation; to Dr. Patricia Pauley, for providing an omega equation solver that served as a basis for the solver developed here; to Dr. Leslie Rosenfeld (NPS/MBARI) for her help in the analysis of the internal tides. I am also thankful to Mr. Paul Jessen (NPS), for his prompt reply to my data demands, and to Mr. Robert Hale, for his help with the computer programming aspects of the primitive equations model.

I am grateful to my Doctoral Committee, especially to its Chairman, Dr. Roland Garwood, for their support during the course of this work and during my stay at the Naval Postgraduate School.

None of the work developed and presented in this dissertation would have been possible without the watchful guidance and infinite patience of Dr. Robert Haney. I am very thankful for his friendship and for all that I have learned from his vast knowledge of oceanic and atmospheric sciences.

This work was sponsored by the Physical Oceanography Division (Code 322PO) of the Office of Naval Research, whose support is gratefully acknowledged. The author was partly supported by the Fundação Calouste Gulbenkian, Lisbon, and by the Portuguese Navy's Instituto Hidrográfico, Lisbon.

Lastly, but by no means the least, I am indebted to my wife, São, for her constant love and encouragement. This work is dedicated to her.

I. INTRODUCTION

The large scale and the mesoscale circulation in eastern boundary currents (EBC) are becoming well established areas of active research. This is particularly true in the coastal zone, where the interaction between the eastern boundary currents and the boundary is strongest. Consequently, a series of research experiments designed to study the dynamics of these regions are being carried out. An area that has seen a great deal of research is off the west coast of the United States, mainly the Oregonian and Northern Californian coasts (California Cooperative Oceanic Fisheries Investigation, Coastal Ocean Dynamics Experiment, Coastal Transition Zone experiments, among others).

An extensive work describing the circulation of the California Current System, assembling results from various early experiments, is found in Hickey (1979). This study documents the existence of a broad, slow southward flow offshore, with strong coastal upwelling in selected areas during periods of strong northerly wind events. The study also describes an undercurrent flowing poleward and the reversal of the inshore surface current, that flows poleward when the wind relaxes.

The early interest in eastern boundary currents was indeed linked to the study of upwelling, an important phenomenon that takes place over large areas of western continental margins and which contributes to the enhancement of the nutrient content of coastal waters (e.g. Huyer, 1983 and Huyer, 1984). It was later recognized, mainly with the availability of satellite imagery (Rienecker and Mooers, 1989; Pares-Sierra *et al.*, 1993), that eastern boundary currents, once considered slow and steady flows, are in fact very rich in mesoscale features mainly resulting from the interaction of the currents with the coast, bottom, and local winds. From this interaction there results an intricate circulation where cold filaments extending offshore and permanent and recurring eddies are common features.

With the identification of these mesoscale features, the ocean sciences community started to investigate reasons for their formation and development. This led to a wealth of observational programs utilizing a variety of remotely sensed and *in situ* techniques, not only off the west coast of the United States but also in other eastern boundary current regions (e.g., Ramp *et al.*, 1991; Sousa, 1992; Le Groupe Tourbillon, 1983). The

importance of mesoscale eddies in the transport of heat, salt and other bio-physical properties in the coastal ocean is also being investigated.

It now seems clear that coastal upwelling, mesoscale eddies and cold filaments are closely related. An equatorward coastal jet will develop meanders by virtue of instabilities in the flow, associated with vorticity and curvature mechanisms. The mean relative vorticity of the jet increases toward the coast, and the ocean depth decreases in this direction, assuming a sloping bottom. This causes the mean potential vorticity to increase towards the coast, so the meandering of the jet behaves like a planetary Rossby wave, propagating upstream relative to the flow. This propagation speed can be of the same order of magnitude as the mean equatorward jet speed, and thus some meanders can become stationary. This effect, in conjunction with local topographic features such as capes, which tend to induce their own vorticity effects in the flow and also cause appreciable local wind changes, is a good scenario for the appearance of permanent or recurrent eddies at certain locations along the coast. These mechanisms may produce the offshore surface flow of recently upwelled waters, that tends to be stronger just south of the capes. In this situation, an eddy could entrain and advect offshore the upwelled coastal waters.

The eddies will not remain stationary once generated. According to the analytical theory of Nof (1981, 1984), the eddies will propagate westward, away from the boundary. Although Nof's analyses are based on somewhat strong assumptions, the general results are valid in a qualitative point of view and have been shown to be in good agreement with some physical cases (Bowman, 1985; Andrews and Scully-Power, 1976). This westward propagation could contribute to the formation of the filaments observed in the vicinity of capes; the filaments often have two or more coupled eddies at their extremity.

A useful technique for the study of eddies and cold filaments is numerical simulation (e.g. Haidvogel *et al.*, 1991; Batteen *et al.*, 1992; Pares-Sierra *et al.*, 1993). In the California Current region, Paduan and Niiler (1990) and Swenson *et al.* (1992) applied quasigeostrophic theory to the motion of clusters of surface drifters. Their results suggest that meanders in the seaward flowing jets and filaments have secondary circulations and vertical motions of 10–20 m/day at the base of the surface mixed layer. Walstad *et al.* (1991) used a quasigeostrophic model to study the California coastal jet observed during the 1987 Coastal Transition Zone (CTZ) program. The focus of this study was to determine the rotational (nondivergent) part of the currents including the “level of no motion” which was found to be shallower toward the coast. It is important to note that all of the previous efforts to analyze the structure and dynamics of the California coastal jet and eddies have

been based on quasigeostrophic theory, and most of the studies such as those based on surface drifters, have been restricted to only the upper mixed layer.

Other authors have used quasigeostrophic theory to analyze similar situations in other ocean areas. In the study of vertical motion near the Gulf Stream, Lindstrom and Watts (1994) used the quasigeostrophic vorticity equation, among other methods, to compute vertical motion making direct use of observed data, since their data had sufficient temporal resolution. Henrick *et al.* (1979) made use of an analytical model based on the quasigeostrophic potential vorticity balance to predict perturbations of pressure, density and velocities in mesoscale eddies. Arhan and Colin de Verdiere (1985) used data collected during the Tourbillon experiment to do a statistical fit of streamfunction and quasigeostrophic vorticity fields, and then to describe the dynamics of an anticyclonic eddy. The vertical motion in this case was not well described. A number of other studies present only a description of data collected in the vicinity of eddies, without attempting to go beyond basic analyses.

The study described here deals with such an eddy observed offshore of Pt. Arena, California. The eddy is about 90 km in diameter and 1000 m depth. The eddy was observed between 22 and 25 May, 1993, during a cruise on board the R/V Point Sur. The processes described above are particularly significant in the area where the eddy was observed; the region between Pt. Arena and Pt. Reyes has the most favorable upwelling conditions of the entire coast (Huyer, 1984). A study of the California Current System off Oregon and Northern California by Ikeda and Emery (1984) includes satellite imagery showing filaments and eddies offshore of Pt. Arena in the summer of 1982, suggesting the recurrent nature of the eddy observed in May 1993.

The objective of this study is to describe the complete three-dimensional circulation associated with a closed cyclonic eddy that was observed in the California coastal region. The description is accomplished by assimilating a unique data set into a primitive equation numerical model. The methodology used is to objectively analyze the quasi-synoptic hydrographic data collected during a recent Eastern Boundary Current (EBC) research program, and satellite sea surface temperature data, and then to use the analyzed density field as input to the model. The use of a new initialization procedure yields dynamically balanced velocity and mass fields that are used in the description of the eddy and its dynamics. This methodology is not restrictive to the application above (description of the observed cyclonic eddy) or to the California coast. It can be applied in other areas of the world ocean where mesoscale vertical motion has been poorly or not determined at all,

as long as the available data has enough spatial resolution. These areas include, for example, other eastern boundary current regions (e.g., the Eastern Atlantic Current along the coast of Portugal). Other possible applications are the study of the three-dimensional circulation associated with coastal jets and filaments, and frontal zones.

The interpretation of the results from the model includes a discussion of aliasing or distortion in the data caused by processes with temporal and spatial scales of the same order of magnitude of the spacing of the hydrographic stations. Other important questions addressed in this study are whether internal tides were present during the collection of the hydrographic data, and what their effect might be, and also the distortion effects related to the rotation of the cyclonic eddy during the CTD sampling.

In addition to presenting a complete description of the eddy, the hypothesis that the dynamics of the eddy can be interpreted within the framework of quasigeostrophic theory was also tested; quasigeostrophic theory describes adequately the dynamics of systems with small Rossby numbers. Attention was focused on the vertical motion, for several reasons. First, it is an important quantity that has not been measured directly in the EBC program; secondly, it is responsible for the vertical advection of important tracers and it influences biological productivity; thirdly, it is related to departures from geostrophy and secondary circulations; finally, it is essential in some conceptual models of vorticity in meandering jets and eddies.

This study is organized as follows: Chapter II has two parts; in the first part the available data is described, including hydrographic and moored data; the second part presents the data analysis, including the interpolation to a regular grid for model applications. Chapter III describes the methods used for the computation of the vertical velocity, namely the circulation model initialized in such a way as to isolate the slow mode captured by the data, and the quasigeostrophic omega equation. Chapter IV has two parts: the first part presents and discusses the results obtained with these methods and describes the physical features of the eddy. It also includes discussions on the initialization and geostrophic adjustment, and potential data related problems such as the effect of internal tides, eddy rotation and sensitivity to data interpolation. The second part presents and discusses the results obtained with the quasigeostrophic omega equation. Finally, Chapter V gives conclusions and final recommendations.

II. DATA

A. DATA DESCRIPTION

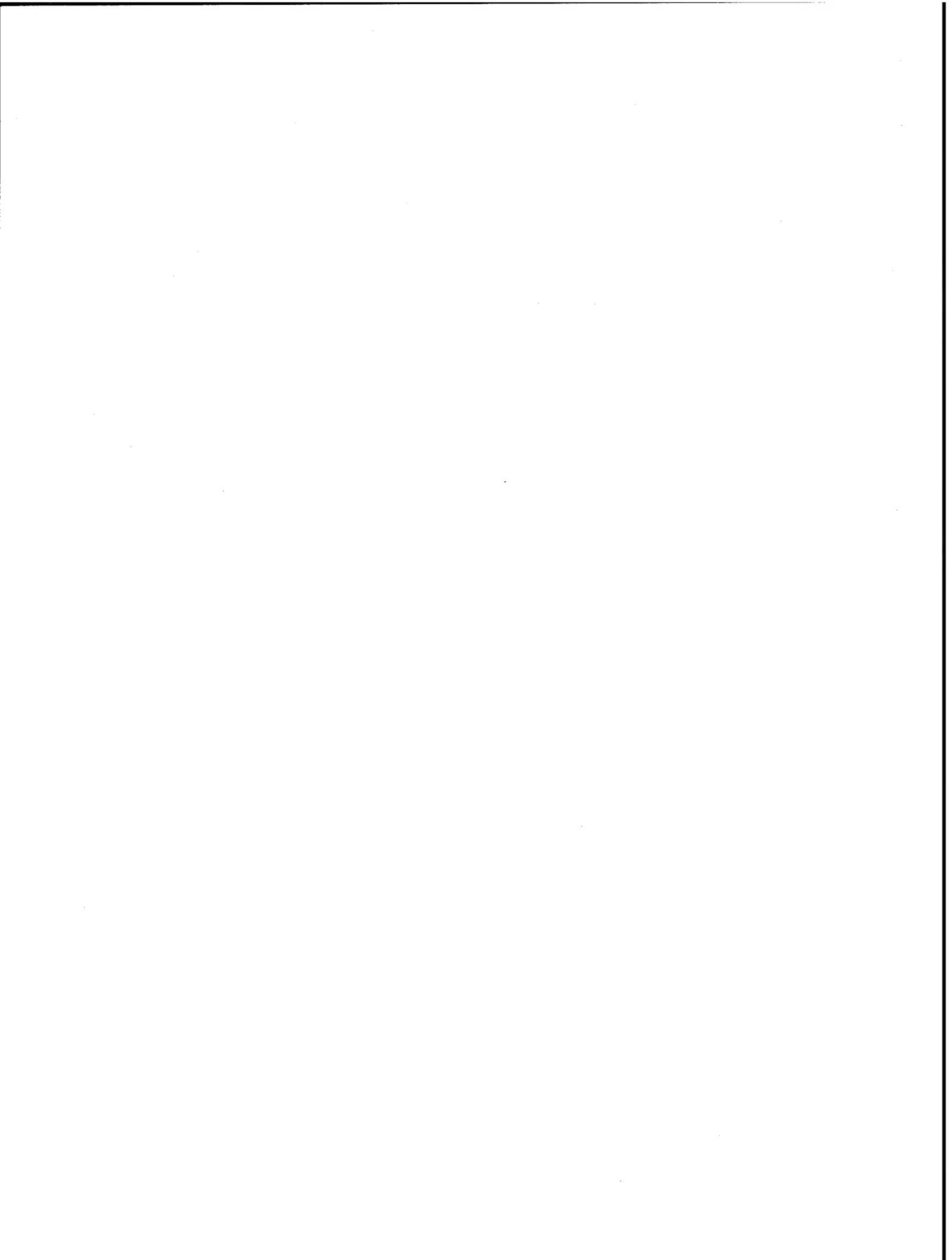
The data used in this study consists of satellite data and hydrographic data from a quasi-synoptic Eastern Boundary Current (EBC) CTD survey off Pt. Arena, California, in May 1993. The objective of the survey was to observe and resolve eddies and filaments that had been seen off Pt. Arena in earlier studies such as the Coastal Transition Zone (CTZ) program in 1987–1988. As shown below, the survey was successful in mapping a very large fraction of a closed cyclonic eddy that had just cut off and separated from the coast.

1. Satellite imagery

The satellite data used in this work consists of images obtained at the Naval Postgraduate School. The raw images contain all five channels of the Advanced Very High Resolution Radiometer (AVHRR) flying on the National Oceanic and Atmospheric Administration (NOAA) series of Earth observing satellites. This sensor observes the surface of the Earth in the visible and infrared (IR) regions, using wavelengths between 3.7 and 11.5 μm . The sea surface temperatures (SST) were computed by means of a multispectral algorithm that converts brightness temperatures to sea surface temperature and corrects for the effect of the atmospheric water vapor on the observed radiances.

The images were processed using software developed at the University of Miami. This processing consisted of correcting the images for appropriate navigation (geographical correction) and of remapping the entire image into the region of interest, centered at a point off Point Arena, California. The ground resolution depends on the distance between each particular pixel and the satellite nadir and is estimated in the range of 1 to 3 km.

Most of the images collected during the period of the cruise contained large amounts of cloud cover; for this reason, only the images for 21 and 22 May 1993 (23:00 Greenwich Mean Time) were suitable to be used in this work. An example of an image from 22 May, obtained from only the channel four of the AVHRR, containing also information on the area covered by the model domain (see Chapter III) and hydrographic stations (see section II.A.2), is given in Figure 1.



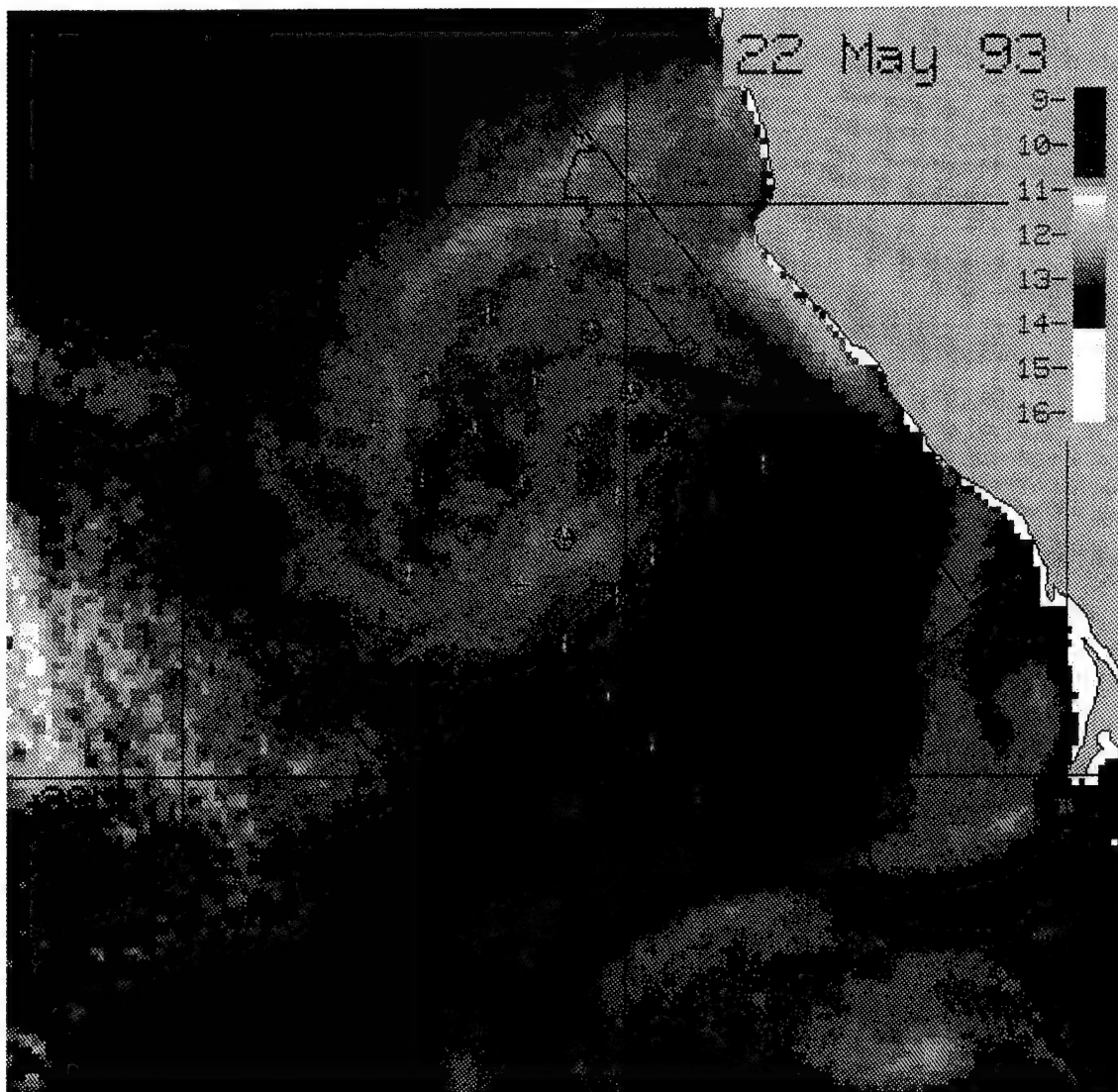
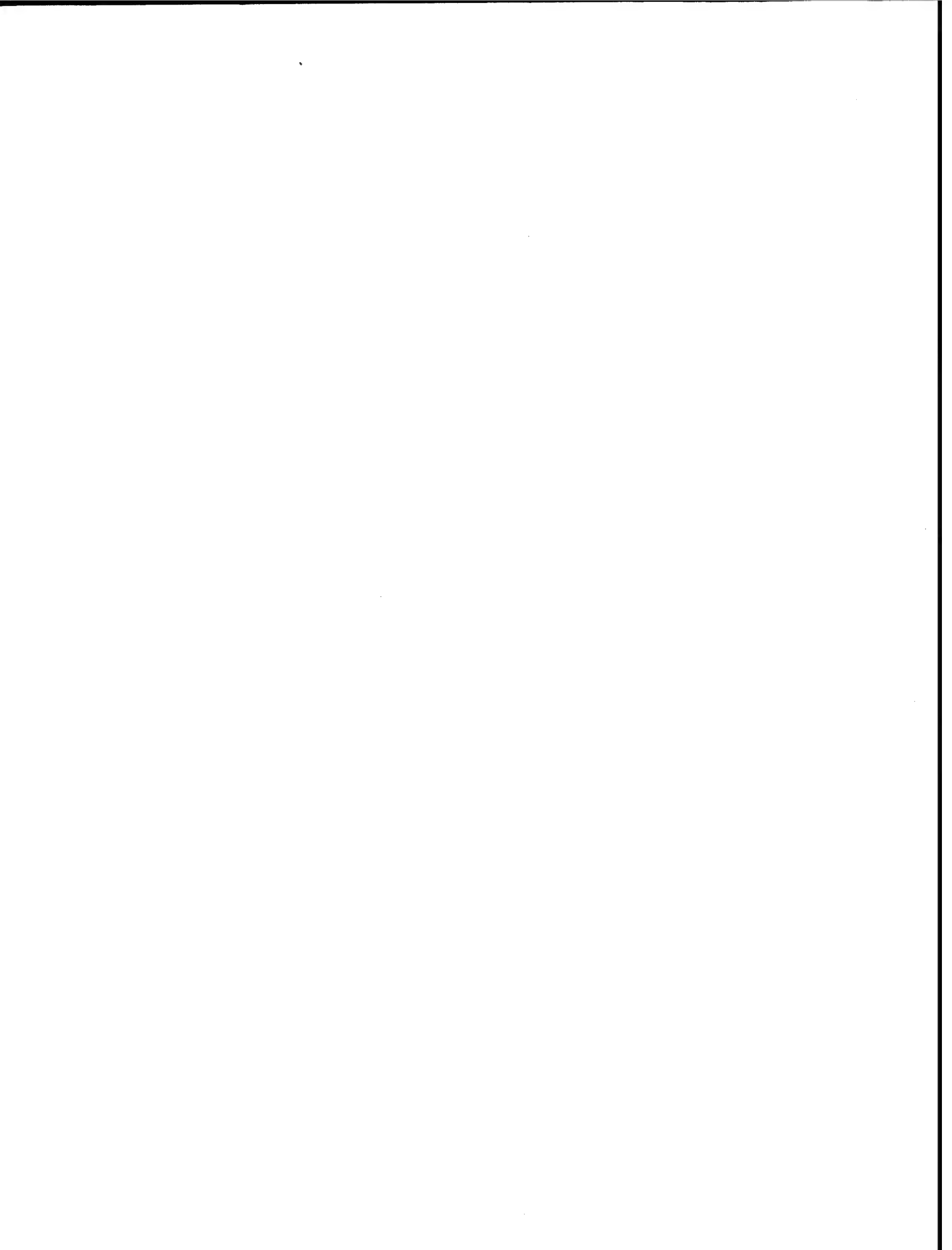


Figure 1. National Oceanic and Atmospheric Administration (NOAA) satellite image, obtained from Channel 4 of the Advanced Very High Resolution Radiometer (AVHRR), of the Sea Surface Temperature (SST) off Point Arena, on 22 May 1993, 23 GMT. The crosses represent the positions of the CTD stations; also shown is the area of study (model domain). Temperatures are in degrees Celsius.



A surface temperature map was obtained by sampling the multispectral image of May 22, 23:00 GMT at the same horizontal positions of the grid used in the model, thus providing a grid of satellite-derived SST used later in the data interpolation (see section II.B.a).

2. Hydrographic data

The hydrographic data used in this study were collected during a Naval Postgraduate School cruise on board R/V Point Sur, between 21 and 25 May, 1993, using a Neil Brown Mark III Conductivity, Temperature and Depth (CTD) instrument. The CTD casts were performed at an array of stations listed in Table 1. The column labeled *MAX Z* means the maximum depth attained in the cast; the column labeled *DEPTH* is the depth to the bottom at the station. See also Figures 1 and 2.

<i>LONG (W)</i>	<i>LAT (N)</i>	<i>Sta No</i>	<i>DATE</i>	<i>TIME (h)</i>	<i>MAX Z (m)</i>	<i>DEPTH (m)</i>
-123.697	38.546	1	22	23.9	479	500
-123.779	38.643	2	22	22.7	419	460
-123.857	38.750	3	22	21.4	371	410
-123.951	38.859	4	22	20.0	415	455
-124.027	38.970	5	22	18.5	471	530
-124.176	38.889	6	23	10.6	2253	2420
-124.080	38.782	7	23	8.3	2041	2110
-123.984	38.675	8	23	6.0	1959	1965
-123.917	38.587	9	23	4.0	1933	1940
-123.811	38.478	10	23	1.8	1623	1630
-123.940	38.393	11	23	24.0	2191	2280
-124.026	38.493	12	23	21.2	3111	3125
-124.100	38.591	13	23	18.8	2443	2500
-124.212	38.700	14	23	16.1	3197	3200
-124.313	38.808	15	23	12.8	3257	3260

Table 1. Characteristics of the CTD Stations

<i>LONG (W)</i>	<i>LAT (N)</i>	<i>Sta No</i>	<i>DATE</i>	<i>TIME (h)</i>	<i>MAX Z (m)</i>	<i>DEPTH (m)</i>
-124.456	38.703	16	24	11.4	2041	3500
-124.332	38.595	17	24	9.1	2035	3445
-124.239	38.507	18	24	6.4	3411	3430
-124.131	38.414	19	24	4.2	2033	3430
-124.027	38.318	20	24	2.0	2031	3430
-124.149	38.236	21	25	11.6	2031	3600
-124.248	38.338	22	25	9.4	2035	3670
-124.356	38.422	23	25	0.6	3563	3650
-124.467	38.525	24	24	22.0	2029	3605
-124.574	38.621	25	24	19.6	2037	3660
-124.787	38.807	26	24	14.5	2035	3610
-124.681	38.714	27	24	16.9	2033	3650
-124.498	38.356	28	25	3.8	2033	3760
-124.629	38.282	29	25	6.0	2033	3840
-124.049	38.150	30	25	13.6	2033	3610
-123.948	38.061	31	25	15.7	2031	3510
-123.842	37.966	32	25	17.9	2049	3480

Table 1. Characteristics of the CTD Stations (Continued)

The instrument's pressure, temperature and conductivity sensors were calibrated prior to and after the cruise. A General Oceanics rosette sampler was used to collect water samples *in situ* for conductivity calibration after the cruise. The CTD sampling rate was 32 Hz. The raw data were collected and processed using a software package developed at EG&G Marine Instruments. The processing done at this level consisted of removing bad data points (outliers) using a first difference criteria to detect suspicious data points and linear interpolation to perform the correction. The data were then averaged to every 2 dbar and recorded in files for later data analysis.

An underway data acquisition loop was active during the cruise, automatically recording averages of temperature and salinity (among other data) at a depth of 2 m every

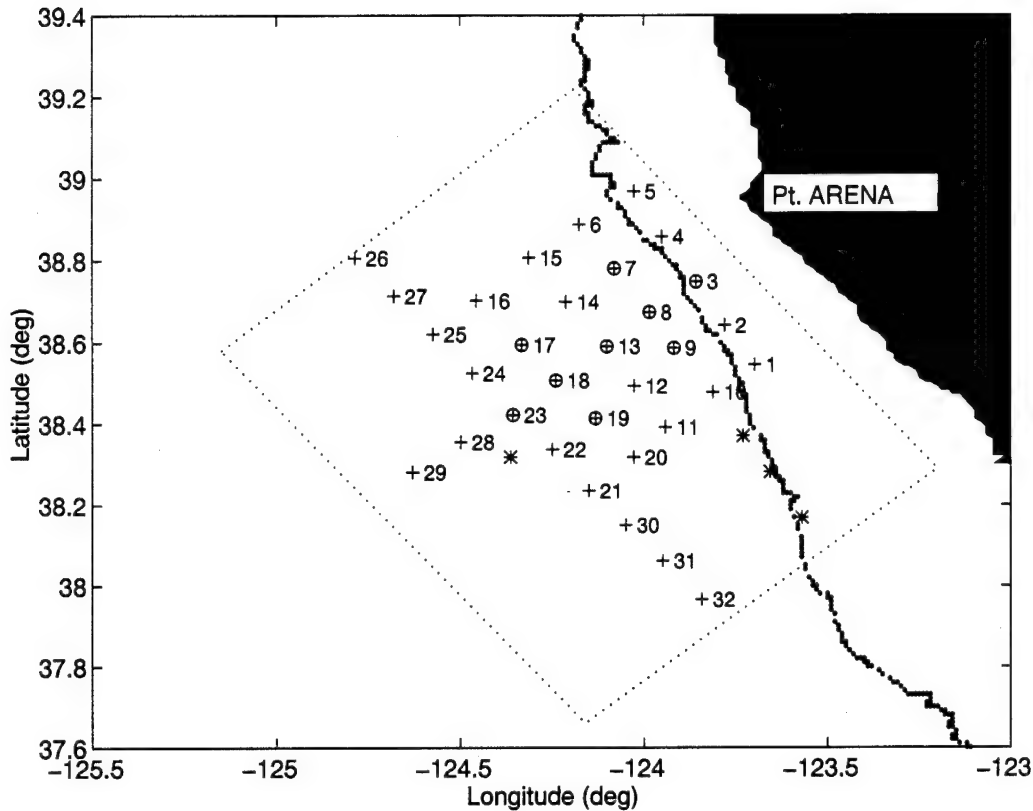


Figure 2. Position and number of CTD stations. Current meter moorings are indicated by the symbol \oplus . Also shown are SAIL stations (symbol *), the 1000 m isobath and the area of study (model domain).

30 seconds (Ship's Data Acquisition System, SDAS). These surface data were used to help fill data void areas in the interpolation phase, and will be referred to hereafter as *SAIL* data (from Serial Ascii Interface Loop). *SAIL* data were selected at four positions (*SAIL* stations) separated by approximately the same spacing of the CTD stations, which is about 14 km (see Figure 2).

The SDAS also recorded wind speed and wind direction. Figure 3 shows the wind conditions during the cruise. Although there was considerable wind variability during the survey period, there is no indication that it was in a scale, in space or time, comparable to the observed ocean eddy. Thus, although they may be important in the early eddy formation stages, the local effects of wind and surface heat flux forcing are neglected in this study.

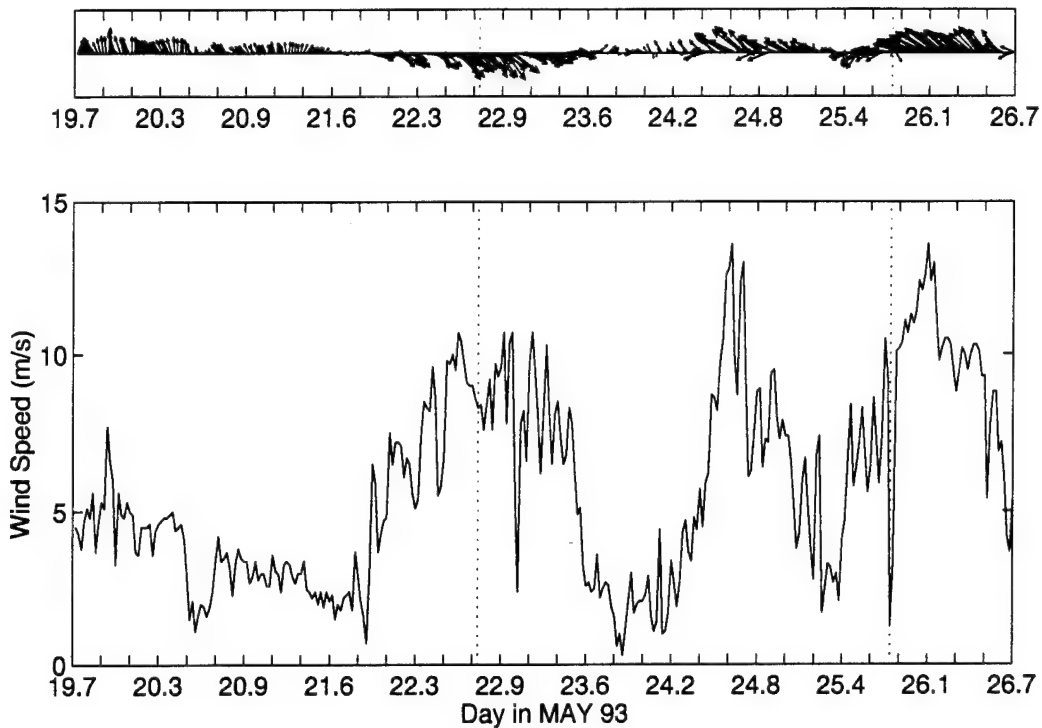


Figure 3. Top: wind vector (direction in degrees true); Bottom: wind speed in m/s during May, 1993 off Pt. Arena. The vertical dotted lines mark the beginning and end of the cruise.

A hull-mounted ADCP looking downward recorded velocity data continuously following the track of the ship, using accurate navigational information from the Global Positioning System (GPS) to compute the absolute velocity. The ADCP is able to measure the three components of the current using an array of four acoustic beams; the Doppler shift induced in the returning echoes by the moving column of water is processed to compute the absolute three dimensional current vector. An appropriate time gating of the echo yields a profile of the velocity field in the vertical at several depth bins (for more details on the ADCP instrument, see Acoustic Doppler Current Profilers, 1989).

In addition to the ADCP current observations, moored current meters (conventional rotor meters) were also deployed at station numbers 3, 7, 8, 9, 13, 17, 18, 19 and 23 (see Figure 2). These instruments were deployed at 100, 150, 300 and 600 m. One mooring also had an instrument at 1800 m. Only current meter data from stations 7, 8, 9 and 13 were available for this study. The remaining instruments were recovered at a later time and their

data are still being processed elsewhere (Scripps Institution of Oceanography and Oregon State University). Table 2 lists the vertical distribution of instruments by mooring, identified by CTD station number.

STATION NUMBER	DEPTH (m)				
	100	150	300	600	1800
3		X	X		
7	X	X	X	X	
8	X	X	X	X	X
9	X	X	X		
13	X	X	X	X	

Table 2. Spatial Distribution of Current Meters

It is assumed that the uncertainty associated with ADCP velocity measurements, which can be as large as 10 to 15% of the mean horizontal current (e.g., Smith and Morrison, 1989; Geyer and Signell, 1990), is well beyond the typical magnitude of low frequency vertical motions, thus large enough to disregard the use of ADCP vertical velocity estimates in this study. However, the observed horizontal velocities from both the ADCP and the current meters were used to define the level of known motion (see section III.A.2) and to compare model results with observations (see section IV.A.1). Time series of temperature and velocity data collected by the current meters were also used in estimating the effect of internal tides on the results (section IV.A.3.a).

B. DATA ANALYSIS

An inspection of the maximum depth attained on each CTD station in Table 1, "Characteristics of the CTD Stations", shows that whereas the deeper stations can be referenced to a common depth of 2000 m, the shallower stations (1 to 5, 8 to 10) do not reach that depth due to the shoaling bottom. For reasons that will become clear further on (section III.A), a similarity method was used here to extend those stations' profiles down to 2000 m, to achieve a regular three-dimensional, flat bottom domain. This method searches for temperatures in the nearest complete profile equal to the deepest temperature in the profile to be extended. After the match is found, the lower part of the former is copied

to the latter. The similarity method is attributed to Helland-Hansen, but no citation was found.

The now complete (common depth) CTD data were then analyzed using an optimal interpolation method first introduced by Hardy (1971), the multiquadric–biharmonic (MQ-B) interpolation method, that has seen several recent applications in meteorology (Nuss and Titley, 1994) and oceanography (Chumbinho, 1993). Other authors have applied this method to other fields of research, including the one for which the method was initially designed, the representation of topography. This method has been studied by several authors (Hardy, 1990; Sirayanone, 1988; Nuss, 1994), who believe that it presents advantages over other common interpolation schemes (e.g., Barnes and Cressman objective analyses) in applications where irregularly spaced, scattered data must be mapped into a regular grid. The method behaves very benignly in data void areas, that is, it does not introduce unrealistic scales in these areas, as well as it does not introduce scales smaller than the spacing between data points. Moreover, the simplest form of MQ-B interpolation (the collocation mode, after Hardy, 1990) is of very simple implementation.

The purpose of using this method in the data analysis was to combine the CTD data below the surface with the satellite data at the surface, and to extend the observed gradients horizontally outside the CTD area to fill the model domain. However, preference is given to the horizontal density gradients because they determine the vertical shear of the currents; this limits somewhat the propagation of surface temperatures to deeper levels, which is also desirable. The satellite-derived SST are representative of the surface skin depth only, and thus may not be related to the temperatures at deeper levels. Haney *et al.* (1995) show, in a study that attempted to recover temperature profiles from shallow CTD profiles using empirical orthogonal functions, that CTD casts to shallow depths less than 100 m are not capable of representing the whole water column. Thus, the main result of this MQ-B analysis is the correct representation of the horizontal density gradients determining the vertical shear.

1. Multiquadric–biharmonic interpolation method

This section gives a description of the MQ-B method, following closely that provided by Nuss (1993). Consider a three-dimensional irregular surface containing a field sampled at N observation points. For each observation point we know the location, (x,y,z) , and the value of the field, H . This irregular surface can represent any scalar (and, in more

recent applications, also vector) field. The purpose is to reconstruct the irregular surface based on the observed data.

The interpolation of the field value in any arbitrary point X is based on a weighted sum of radial basis functions:

$$H(X) = \sum_{i=1}^N a_i Q(X - X_i), \quad (2.1)$$

where a_i is the weight of the *kernel* function Q whose argument is the radial distance between the field point X and the observation point X_i . In the multiquadric–biharmonic interpolation method, the kernel function is a quadric function:

$$Q(X - X_i) = [(X - X_i)^2 + c^2]^{1/2}. \quad (2.2)$$

The constant c is a small arbitrary number to keep the function from vanishing at the observation points. For the three-dimensional interpolation case, the kernel function is therefore:

$$Q(X - X_i) = [(x - x_i)^2 + (y - y_i)^2 + (z - z_i)^2 + c^2]^{1/2}. \quad (2.3)$$

To solve for the weights, we apply Equation 2.1 to all N observation points, resulting in a set of N equations with N unknowns:

$$H(X_j) = \sum_{i=1}^N a_i Q_i(x_j, y_j, z_j). \quad (2.4)$$

In matrix notation, the solution is given by:

$$\mathbf{a} = \mathbf{Q}^{-1} \bullet \mathbf{H}_f \quad (2.5)$$

where \mathbf{Q} is the square matrix of equation coefficients and \mathbf{H}_f is a vector of the observed field values. This matrix can be inverted using any of the mathematical routines available for solutions of linear systems of equations (e.g., Linpack, 1978, or Matlab, 1994).

Once the weights are known, the interpolated solution to any point in the field (in usual applications, regularly spaced grid points) is then given in matrix notation by:

$$\mathbf{H}_g = \mathbf{Q}_g \bullet \mathbf{a}, \quad (2.6)$$

where:

$$\mathbf{Q}_g = [(x_g - x_i)^2 + (y_g - y_i)^2 + (z_g - z_i)^2 + c^2]^{1/2}, \quad (2.7)$$

(x_g, y_g, z_g) being the coordinates of each desired field point. The matrix on the left hand side of Equation 2.7 has as many rows as there are field (grid) points, but the number of columns is always equal to the number of observation points N . In other words, the solution depends only on the number of observation points available and is independent of the size of the grid to be interpolated. The two-dimensional problem is just a particular case of the more general three-dimensional case, with all z coordinates set to zero.

The condition that the sum of the weights be equal to zero (Hardy, 1990) is implemented by adding an extra row and column to \mathbf{Q} as follows:

$$\mathbf{Q}' = \begin{bmatrix} \mathbf{Q} & \begin{bmatrix} 1 \\ \dots \\ 1 \end{bmatrix} \\ \begin{bmatrix} 1 & \dots & 1 \end{bmatrix} & 0 \end{bmatrix}, \quad (2.8)$$

where the vectors have length N , and by appending a zero to the data vector \mathbf{H}_f . This, in turn, introduces a new term a_0 in the weight vector:

$$\mathbf{a} = [a_1 \ a_2 \ \dots \ a_N \ a_0]^T. \quad (2.9)$$

The new term a_0 represents the average value of the entire observation data and thus must be added to the final interpolated field. The multiquadric matrix in Equation 2.6 maintains the dimensions mentioned above (i.e., $M \times N$, where M is the total number of grid points), since for the field interpolation only the first N weights are used. The MQ-B interpolation equations are:

$$\mathbf{H}_g = \mathbf{Q}_g \bullet \mathbf{a} + a_0, \quad (2.10)$$

with $i = 1, \dots, N$ and $g = 1, \dots, M$.

The method presented above is valid for noise-free observations. Unfortunately, real data include observational errors that must be taken into account. This is achieved through the introduction of an uncertainty parameter and a smoothing parameter (Nuss and Titley, 1993) in Equation 2.4. In matrix notation:

$$\mathbf{H}_f = [\mathbf{Q} + N\lambda\sigma^2 \cdot \delta_{ij}] \bullet \mathbf{a}, \quad (2.11)$$

where λ is the smoothing parameter, σ^2 is a vector of uncertainties in the observations (mean-squared observation error) and δ_{ij} is the Kronecker delta function. The difference now is that the diagonal elements of \mathbf{Q} are modified to include a factor involving those two parameters. Note that the uncertainties vector can have different values for different observation points, a useful property that gives the user of the method enough freedom to optimally set the parameters for best fitting any part of the grid.

2. Data interpolation

The multiquadric–biharmonic interpolation method described above was applied to the temperature and salinity data to obtain an analyzed three-dimensional density field in the model domain. Chumbinho (1993) presents some thoughts about the MQ-B method, namely the choice of the interpolation parameters c and λ , and the choice of an appropriate vertical scale exaggeration. The interpolation parameters were set to values close to those used in other applications of MQ-B (Nuss, 1994; Nuss and Titley, 1994), in a way that guarantees the best representation of local maxima and minima, without distortion of the interpolated field in regions where data is scarce or not available. The vertical exaggeration is necessary to emphasize the correct representation of the horizontal gradients over the vertical ones, which are usually much larger.

The number of temperature observations is much larger than the number of salinity observations because of the use of satellite-derived sea surface temperatures. As noted previously, these were used in an attempt to compensate for the lack of CTD data in several parts of the domain. For this reason, the data interpolation was carried out differently for these two state variables.

a. Temperature interpolation

The CTD temperature data were first decimated along each profile to the same 27 depth levels used by the circulation model (-3.5, -12.5, -24.3, -38.0, -54.9, -75.9, -101, -131, -166, -206, -252, -303, -360, -423, -493, -570, -653, -744, -842, -948, -1060, -1182, -1312, -1450, -1596, -1750 and -1916 m; also, see section III.A). This decimation was performed following the filtering criteria defined by Crochier and Rabiner (1983) for non-uniform decimation, and according to the idea that the MQ-B interpolation works best when the data points coincide with grid points (Hardy, 1990, p. 164). This resulted in 32 *in situ* temperature data points at each of the 27 vertical levels, for a total of 864 points.

The satellite-derived sea surface temperature data (SST) were sampled directly from the multispectral satellite image equivalent to the single-channel image in Figure 1, at a resolution of 48×39 points, respectively in the alongshore and cross-shore directions, covering the model domain represented by the rectangle in Figure 2, using a geographical to Universal Transverse Mercator (UTM) coordinates transformation and posterior rotation. The origin of the UTM coordinates is the northwestern corner (or lower left corner, in the figures). The total number of SST data points is thus 1872, which is much larger than the 32 temperature data points at the second level.

The MQ-B performs best when the data are irregularly spaced, without sharp contrasts in spatial data density (Hardy, 1990). This was readily observed in the first few interpolation runs without any pre-processing: the three-dimensionally interpolated temperature field presented severe distortions in the upper levels, caused by the contrast in the number of total data points at the surface and at the level immediately below. This problem lead to the necessity of pre-processing the temperature observations.

The SST data were thus two-dimensionally decimated by a factor of seven, resulting in a rectangular array of 8×7 data points covering the same area, again following the criteria defined by Crochiere and Rabiner (1983); at the same time, a two-dimensional MQ-B interpolation of temperature was carried out at each level, using very small parameters ($c=1 \times 10^{-4}$, λ infinitesimally small), to artificially increase the number of observations at depth from 25 to 64 (see below). The interpolation parameters mentioned above introduced no smoothing in the interpolated field, and caused the resulting field to follow the data points exactly (the interpolation results were checked using three-dimensional visualization of the data points against the interpolated field). Only the decimated temperature profiles corresponding to stations 1 to 25 were used in this two-dimensional interpolation, and the resulting field was mapped into a square 8×8 grid about the same size as the horizontal area occupied by these stations, as illustrated in Figure 4.

The last step in the temperature interpolation was to combine the 8×7 decimated SST, the $8 \times 8 \times 27$ two-dimensionally interpolated temperatures, and the 7×27 points from the remaining seven CTD stations (numbers 26 to 32) in a three-dimensional MQ-B interpolation, using $c=2 \times 10^{-4}$, $\lambda=1 \times 10^{-3}$ and an aspect ratio of about 1/60 (achieved by scaling the horizontal dimensions to unity and leaving the vertical dimension unaltered). The resulting three-dimensionally analyzed temperature field followed the data points closely; profiles of analyzed data were compared with nearby CTD profiles, showing a

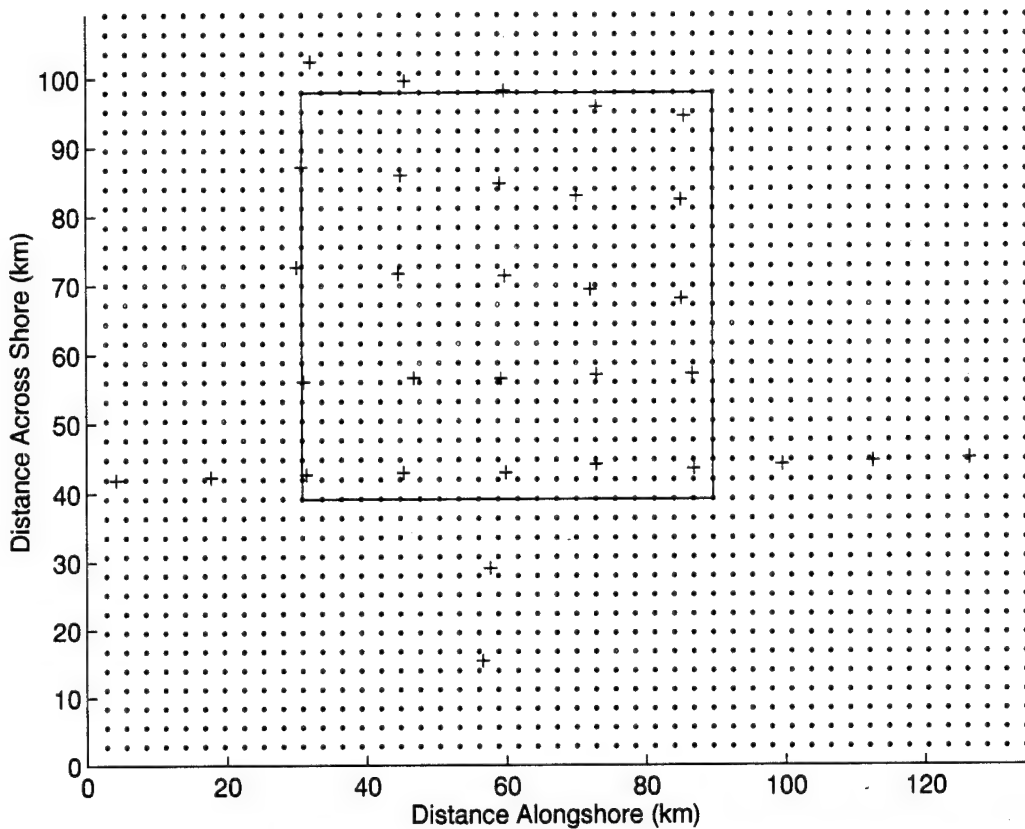


Figure 4. Schematic representation of the 2-D temperature interpolation at each level. The dots are the model domain grid points, the crosses are the CTD stations and the rectangle is the area covered in the 2-D interpolation, mapped by a 8×8 grid.

good match. The maximum differences between analyzed and observed global maximum and minimum temperatures were 0.11 and 0.07 degrees Celsius, respectively. This analyzed field had 48×39 points at each of the 27 levels.

b. Salinity interpolation

The MQ-B interpolation of salinity was considerably simpler than the interpolation of temperature, because there were no sharp contrasts in the number of observations between levels. The CTD salinity profiles were non-uniformly decimated in the vertical, in a manner similar to the temperature vertical decimation, to the same 27 depth levels, resulting in 32×27 observation points. Four other salinity observation points were included in the salinity data vector, corresponding to the SAIL stations, and surface

salinities were taken from an average of the first two CTD records on each profile. The total number of salinity observations was, therefore, 900 data points.

These observations were three-dimensionally MQ-B interpolated using $c=1\times10^{-4}$, $\lambda=1\times10^{-3}$ and an aspect ratio of about 1/60, similar to the temperature interpolation. The slightly different value for c yielded better results, maybe because of the different spatial distribution of salinity observation points compared to that of the temperature observations. The resulting three-dimensionally analyzed salinity field also followed the data points closely, with very good match between analyzed profiles and nearby CTD salinity profiles. The maximum differences between analyzed and observed global maximum and minimum salinities were 0.01 and 0.04 psu, respectively. The dimensions of this field were the same of the temperature field (48×39×27).

3. Analyzed three-dimensional density field

Once the temperature and salinity data, from the various sources described above, were interpolated and analyzed, the three-dimensional (48×39×27) density field was computed using the formulae for $\rho(S,T,p)$ in the International Equation of State (IES 80) found in Gill (1982). The values of density were then converted to sigma values:

$$\sigma(S, T, p) = [\rho(S, T, p) - 1000] \quad (2.12)$$

where S is salinity, T is temperature and p is pressure.

The result was a three-dimensional, analyzed density field from which the three-dimensional currents were diagnosed using the primitive equation model, and the quasigeostrophic vertical motion was computed from the quasigeostrophic omega equation. An implicit assumption of synopticity in the data was made throughout the analysis. The hydrographic data were collected during a period of three days, during which several processes can act to distort the sampled field. Among these are the rotation and translation of the nearly circular eddy (Figure 1), and the propagation of internal waves in the domain sampled by the CTD. The most important internal waves that could be present are internal tides, which have been known to contaminate data sets in other areas. The possible effects of these processes are analyzed and discussed in section IV.A.3.a.

III. METHODS

After the data were analyzed and the three-dimensional density field computed, a field of dynamically balanced currents in the area of study was obtained by initializing a primitive equation model. To help interpret the results, the vertical velocity was also diagnosed from the (quasigeostrophic) omega equation. Both the primitive equation model and the quasigeostrophic omega equation were applied in the volume defined by the analyzed density field (48×39×27, respectively alongshore, cross-shore and in the vertical) whose horizontal extension is depicted in Figure 1 (hereafter *domain*). This domain was chosen to cover a larger horizontal area than the domain defined by the CTD stations to allow for model boundary effects and possible eddy translation.

This chapter describes several aspects relevant to each of these solution methods.

A. CIRCULATION MODEL

The objectively analyzed density field was used in a circulation model for the diagnostic computation and analysis of the dynamically balanced, three-dimensional velocity and density fields corresponding to the *slow mode* assumed captured in the observations.

1. Description

The model used in this study is the multi-level, primitive equation model presented by Haney (1974); it utilizes a B grid in the horizontal and sigma coordinates in the vertical, with vertical staggering of the vertical component of velocity. The inviscid, hydrostatic and Boussinesq assumptions are used to simplify the set of governing equations. This means that the ocean is considered incompressible, and density is replaced by a constant except where it is multiplied by the acceleration of gravity.

This model has been improved with the modifications introduced in the convective adjustment algorithm by Adamec *et al.* (1981) and in the numerical computation of the pressure gradient force in sigma coordinates and in the vertical discretization scheme by Haney (1991). The convective adjustment scheme imposes dynamic stability by using an algorithm that conserves heat and momentum and mixes these two properties between

levels at the same ratio, requiring a final Richardson number (after the scheme has been applied) greater than the critical value of 0.25. The new vertical discretization and pressure gradient force computation were designed to improve this computation over steep topography.

In this study, the dynamics of the observed eddy will be studied under the working hypothesis that surface forcing (wind stress and buoyancy fluxes) and variations in bottom topography can be neglected. This simplifies the model by permitting the use of a single thermodynamic variable, σ , given in Equation 2.12, and a flat bottom. The possible effects of these assumptions will be discussed in Chapter V.

2. Initial conditions

To achieve dynamic initialization of the primitive equation model, information on the initial mass and velocity fields is needed. The former is the objectively analyzed density, or σ ; the latter can be set in one of two ways, if no direct current observations are available in the model domain. The initial shear velocity field can either be set to zero, implying that no *a priori* knowledge of the initial velocities is available, or it can be specified from the initial mass field using the hydrostatic and geostrophic relations. These two initial velocity fields have different implications in the final balanced slow mode solution, as will be seen in section IV.A.2.

The depth averaged flow is also computed from the hydrostatic and geostrophic relations, assuming a level of known motion determined by the current meter data. The resulting vertically averaged flow, being nondivergent, is then used to compute a streamfunction for the vertically averaged velocities. This streamfunction is then kept constant during the short model initialization run.

The level of known motion was chosen to be 2000 m, with a current of 2 cm/s directed alongshore to the northwest, based on current meter data. This apparently simple method was preferred over a more complex method of determining a level of known motion by using the horizontal ADCP currents. This approach would have required an objective analysis of the ADCP currents and the solution of a Poisson equation for the rotational part of the velocity field with consequent specification of boundary conditions for the streamfunction. The correct determination of the depth averaged flow is important because of its effect in the advection of relative vorticity perturbations; however, it will be shown that the solution is barely sensitive to variations in the setting of the bottom current.

3. Boundary conditions

The model has open lateral boundaries governed by modified Ross and Orlanski (1982) radiation conditions, hereafter *RO boundary conditions*. This modified scheme serves to radiate away from the domain any outgoing waves (mainly gravity waves), and to include inward advection of properties specified at the boundaries. The RO scheme can be summarized in three steps:

- computation of a normalized phase velocity δ for propagating waves (see Equation 3.5 below);
- for inflow points ($\delta \leq 0$), the vorticity, divergence and density are set to the observed boundary values;
- for outflow points ($\delta > 0$), the vorticity, divergence and density are advected from the interior using equations of the type:

$$\frac{\partial \xi}{\partial t} + \delta \frac{\partial \xi}{\partial n} = 0 \quad (3.1)$$

In Equation 3.1, ξ is either divergence, vorticity or density, and the spatial derivative is taken along an outward normal n to the boundary. Once the values of divergence and vorticity are known at the boundaries, their definitions are used to compute the normal and tangential components of the baroclinic horizontal velocity. For outflow, density is also advected along the boundary with an equation similar to Equation 3.1, with the spatial derivative generalized to include its tangential counterpart, and a new phase velocity δ_2 computed as the spatial four-way average of the surrounding tangential velocities at each boundary point.

The boundary equations for vorticity and divergence in the outflow case were modified from the original equations given in RO, since their equations were mainly designed to deal with gravity waves, with divergence waves propagating faster than vorticity waves. RO use the phase speed δ to advect vorticity, and $\Delta x/\Delta t$ to advect divergence, where Δx is the grid spacing and Δt is the time increment. This means that the divergence at the boundary is set equal to the value at the adjacent interior point, computed from the prognostic equations governing the interior.

The velocity field in the model initialization runs described below presents noticeable inertial oscillations, where divergence and vorticity waves propagate at comparable speeds. The different advection speeds for one and the other in the RO method caused the components of horizontal velocity to become excessively large on the boundaries. Because of this it was necessary to include the inertial terms and a damping

term in the vorticity and divergence equations at the boundaries (Equation 3.1). These terms follow from taking the curl and the divergence of the inertial balance, resulting in:

$$\begin{aligned}\frac{\partial D}{\partial t} + \delta \frac{\partial D}{\partial n} &= f\zeta - \gamma D \\ \frac{\partial \zeta}{\partial t} + \delta \frac{\partial \zeta}{\partial n} &= -fD - \gamma \zeta\end{aligned}\quad (3.2)$$

where D is the divergence and ζ is the vertical component of relative vorticity:

$$D = \frac{\partial u}{\partial x} + \frac{\partial v}{\partial y}, \quad \zeta = \frac{\partial v}{\partial x} - \frac{\partial u}{\partial y}. \quad (3.3)$$

The damping coefficient was specified to be proportional to the effective gravity wave phase speed (C_a , see below), normalized by the grid size:

$$\gamma = C_a \frac{1}{\Delta x} \quad (3.4)$$

The computation of an appropriate phase speed δ was also revised from RO. Following the work of Durran et al. (1993), the computation of the phase speed was changed to:

$$\delta = C_a + \mathbf{V} \bullet \mathbf{n} \quad (3.5)$$

where \mathbf{V} is the velocity vector at the boundary, \mathbf{n} is an outward unit vector, and C_a is a constant, set as to guarantee propagation of waves out of the domain during most of the integration time (equivalent to the shallow water phase speed of gravity waves). $\mathbf{V} \bullet \mathbf{n}$ is a four-way average of the *normal* velocity; for instance, for the western boundary $\mathbf{V} \bullet \mathbf{n}$ is computed as:

$$\mathbf{V} \bullet \mathbf{n} = -\frac{1}{4} [u_{2,j}^{(n)} + u_{2,j-1}^{(n)} + u_{1,j}^{(n)} + u_{1,j-1}^{(n)}] \quad (3.6)$$

The superscript (n) means values of the variables at time n . This makes the advection-type Equation 3.1 a completely forward-in-time scheme (as it is), which is acceptable for upstream advections (it is used to compute unknown points at the boundary from known interior points, in outflow situations). The final vorticity and divergence equations are, respectively (in finite differences form):

$$\begin{aligned}\zeta_B^{(n+1)} &= \zeta_B^{(n)} - \delta \frac{|\Delta t|}{\Delta x} [\zeta_{B+1}^{(n)} - \zeta_B^{(n)}] - f \Delta t D_B^{(n+1)} - \gamma |\Delta t| \zeta_B^{(n)} \\ D_B^{(n+1)} &= D_B^{(n)} - \delta \frac{|\Delta t|}{\Delta x} [D_{B+1}^{(n)} - D_B^{(n)}] + f \Delta t \zeta_B^{(n+1)} - \gamma |\Delta t| D_B^{(n)}\end{aligned}\quad (3.7)$$

where the superscripts (n) and $(n+1)$ mean time level n and time level $n+1$, respectively, and the subscripts B and $B+1$ mean the boundary point and the adjacent interior point.

Note that because Equation 3.7 uses implicit time differencing for the Coriolis terms, it has to be solved simultaneously for the new time levels. This is done at each time step along all four boundaries, except in the corners. The vorticity and divergence in the corners are set equal to the average of the two adjacent points that have already been computed by advection normal to their boundaries.

For use in the case of inflow at the lateral boundaries, the vorticity was specified from its initial value and the divergence (also from its initial value) was zero. These conditions were held constant during the short model initialization runs.

The boundary conditions for the vertical velocity in this study were zero at the bottom and at the surface.

4. Digital filter initialization

The objectively analyzed density field and geostrophically balanced currents were used as initial conditions in the model. Separate initialization runs were also made with the initial currents at rest. These fields are not in balance, or at least not in the state of near balance that characterizes a quasigeostrophic ocean. A digital filter initialization (DFI) procedure introduced by Lynch and Huang (1992) was used to arrive at a dynamically balanced field of density and currents. The DFI procedure, which removes high-frequency oscillations from the model fields, consists of performing two short (12 h), adiabatic (physics turned off), forward and backward integrations of the equations, starting with the same initial conditions. The resulting model variables at each time step from $t = -12$ h to $t = 12$ h are multiplied by a spatially uniform, time varying weight. The time series of weights corresponds to the coefficients of a digital lowpass filter effectively being applied to the computed fields, i.e.:

$$\hat{q}(n) = \sum_{k=-N}^N q(k) h(n-k) \quad (3.8)$$

applied only for n equal to zero. In the equation above, q is any of the variables u, v or σ , while $h(n)$ is the sequence of filter coefficients, and N is the number of time steps (equal to the integration time forward or backward divided by the time step, which was 300 seconds). This procedure is illustrated in Figure 5. The figure shows an example of a time

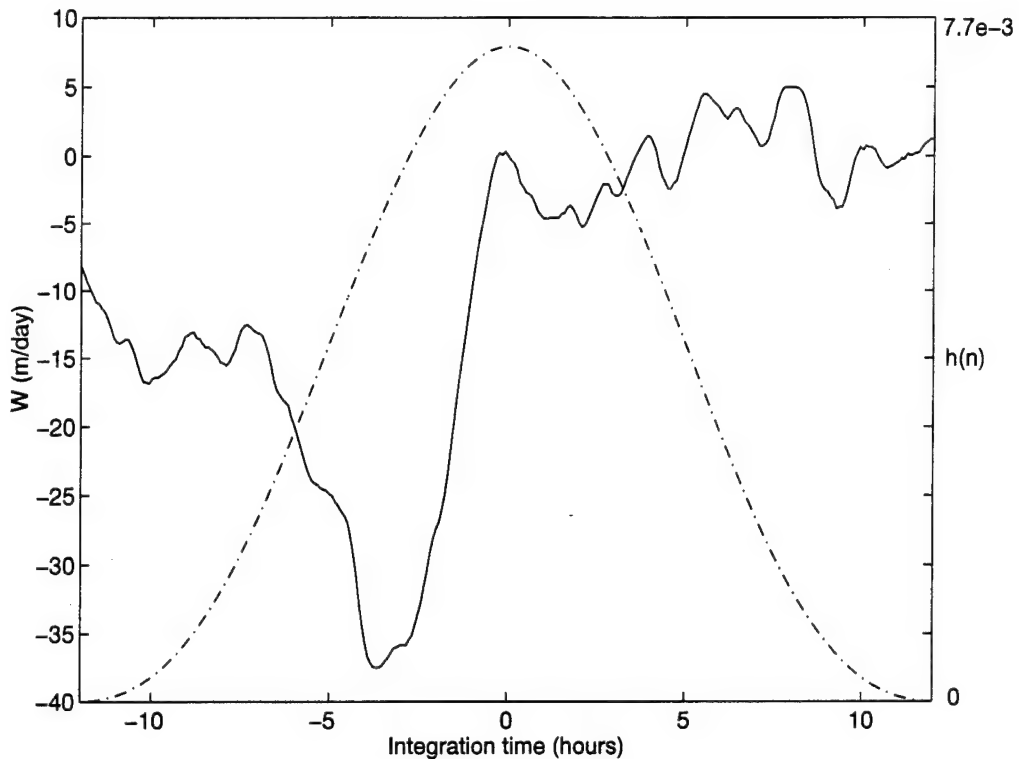


Figure 5. Example of the DFI procedure applied to a typical vertical velocity time series. The solid line is vertical velocity in m/day; the dash-dot line is the sequence of filter coefficients (scale on the right) multiplying that time series.

series of q , in this case the vertical velocity, at one of the grid points, and the time filter that is to be applied to it. The output from Equation 3.8 is $\hat{q}(0)$, the filtered vertical velocity at time zero at that grid point.

The digital filter utilized by Lynch and Huang (1992) consists of a simple lowpass prototype multiplied by a Lanczos window to reduce truncation effects. The same authors have already proposed other filter design techniques (Huang and Lynch, 1993). The possibilities in this area are broad, since various filter responses and designs can be tested, as demonstrated by Viudez *et al.* (1994). In the present study, the filter was implemented as in Lynch and Huang (1992):

$$h(n) = \frac{\sin [n\pi/(N+1)]}{n\pi/(N+1)} \frac{\sin (n\theta_c)}{n\pi} \quad (3.9)$$

where θ_c is the cutoff digital frequency. When this filter is used with a cutoff period equal to the total time spanned by the two integrations (24 hours) and a time step of 300 seconds, the magnitude of the frequency response shown in Figure 6 is obtained. It is seen that the

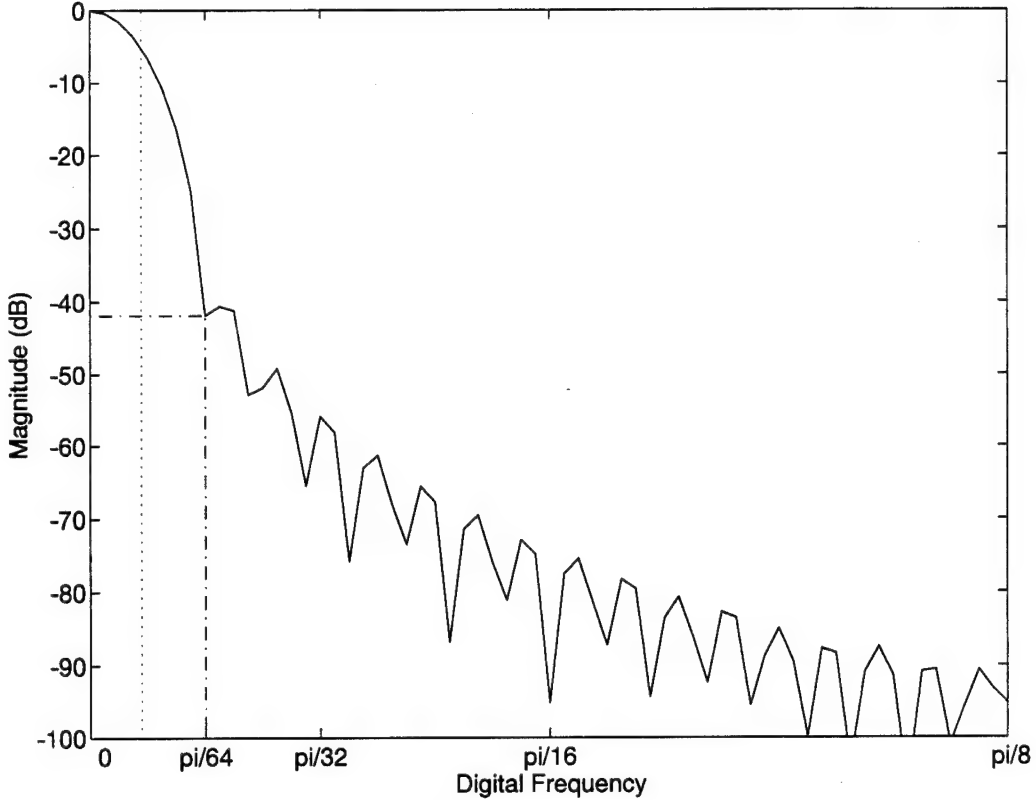


Figure 6. Frequency response of a lowpass filter with cutoff period 24 h, sampling period 300 s (Lanczos window). The dotted line marks the digital cutoff frequency. The dash-dot line marks the response for a period of 12 h.

cutoff period is damped by about 5 dB. It is possible to design more efficient filters that would achieve better frequency responses with fewer coefficients. As explained above in Equation 3.8, the number of coefficients in the filter is directly related to the length of the forward and backward integrations. Thus, fewer coefficients means less computer time in the initialization process. On the other hand, it also means less time for ageostrophic spin-up (development of secondary circulations from the unbalanced mass and velocity fields; see section IV.A.2). A more efficient filter design (for example, using Butterworth or elliptic lowpass filters) would have to take this constraint into account in the computation

of the coefficients to allow enough integration time for spin-up (usually no less than 3 to 6 hours, setting a minimum limit of 36 to 72 coefficients for a finite impulse response filter).

The application of the filter to the model output does not need to be done within the circulation model, as long as enough computer storage space is available to save the model output at each time step. In addition to using different filters, the idea of using the dynamically balanced (filtered) mass and velocity fields as initial conditions for a second DFI (integration-filter) procedure is being tested and verified with model generated data, in a separate study.

In the original paper, Lynch and Huang (1992) show that the DFI procedure is equivalent to a nonlinear normal mode initialization, with the advantage of having a much simpler implementation. The normal mode initialization compares the magnitude of the modes resolvable by a model through long-term integrations (gravity wave modes versus Rossby modes); the same modes are fitted to the analyzed data, and the components that have negligible contributions to the long-term solution (i.e., the gravity waves) are removed from the data. The nonlinear variant of the normal mode initialization takes care of the re-generation of high frequencies that takes place even after those frequencies have been removed from the data, because of the nonlinear terms in the model equations. Therefore, the model is initialized with the slowly varying, almost nondivergent basic state captured in the data. The DFI procedure removes the high frequency modes with the application of the filter. The lowpass filtered fields then represent the dynamically balanced slow mode at the time of the observations.

Horizontal and vertical diffusion was turned off to enable the short backward and forward integrations centered at time zero. When compared to advective processes in regions of strong mean flows, such diffusion is negligible, as noted by Schmitz and Vastano (1975) in a numerical study of Gulf Stream rings over time scales of two months.

B. QUASIGEOSTROPHIC OMEGA EQUATION

The second method of dynamical analysis, which was used to diagnose only the vertical velocity from the data, was to solve the quasigeostrophic (QG) omega equation. The assumptions allowing the simplification of the complete set of equations governing geophysical fluid dynamics into QG equations on a f -plane are the following:

- Hydrostatic balance;
- Geostrophic velocity and vorticity are used everywhere except in the divergence term in the vorticity equation;

- Adiabatic flow;
- Neglect of the vertical advection of vorticity and the tilting of vorticity;
- Relative vorticity much less than planetary vorticity in the divergence term;
- Planetary vorticity is constant;
- Static stability is a function of z (depth) only.

An important concept in QG theory is that vertical motion is entirely due to the ageostrophic part of the currents, because the geostrophic currents are nondivergent. Thus, using the assumptions above, information on the vertical motion is contained in the vorticity equation relating local changes to vorticity advection by the geostrophic flow:

$$\frac{\partial \zeta_g}{\partial t} = - \mathbf{V}_g \bullet \nabla \zeta_g - f_0 \nabla \bullet \mathbf{V}, \quad (3.10)$$

where ζ_g is the vertical component of the geostrophic relative vorticity defined as:

$$\zeta_g = \frac{\partial v_g}{\partial x} - \frac{\partial u_g}{\partial y} = \frac{1}{f_0 \rho_0} \nabla^2 p \quad (3.11)$$

(the last equality follows from the curl of the geostrophic balance), g being the acceleration of gravity and f the planetary vorticity ($2\Omega \sin \phi$).

Equation 3.10 has been used to estimate vertical motion after substituting the continuity equation for incompressible fluids

$$\nabla \bullet \mathbf{V} = - \frac{\partial w}{\partial z}, \quad (3.12)$$

for the horizontal divergence. The resulting equation for w requires knowledge of the local variation of vorticity with time, which is not always available. A more useful equation without any time derivatives (diagnostic equation) can be derived by combining Equation 3.10 with another equation relating vertical velocity to hydrostatic pressure perturbations, the buoyancy equation (Gill, 1982, page 529):

$$\rho_0 N^2 w + \left[\frac{\partial}{\partial t} + \mathbf{V}_g \bullet \nabla \right] \frac{\partial p}{\partial z} = 0 \quad (3.13)$$

where N^2 is the buoyancy frequency defined as:

$$N^2 = - \frac{g}{\rho_0} \frac{\partial \rho}{\partial z}, \quad (3.14)$$

where p is pressure, ρ is density, ρ_0 is a reference density, w is the vertical velocity, and \mathbf{V}_g is the geostrophic velocity vector. The Laplacian and *del* operators are two-dimensional

(horizontal). Equation 3.13 is the nonlinear QG version of the hydrostatic buoyancy equation.

With the help of the hydrostatic relation

$$\frac{\partial p}{\partial z} = -\rho g \quad (3.15)$$

the buoyancy equation can be written as:

$$g \frac{\partial \rho}{\partial t} = \rho_0 N^2 w - g \mathbf{V}_g \cdot \nabla \rho \quad (3.16)$$

From the thermal wind relations

$$\begin{aligned} \frac{\partial u_g}{\partial z} &= \frac{g}{\rho_0 f} \frac{\partial \rho}{\partial y} \\ \frac{\partial v_g}{\partial z} &= -\frac{g}{\rho_0 f} \frac{\partial \rho}{\partial x} \end{aligned} \quad (3.17)$$

an expression for the vertical derivative of geostrophic relative vorticity can be derived:

$$\frac{\partial \zeta_g}{\partial z} = -\frac{g}{\rho_0 f} \nabla^2 \rho \quad (3.18)$$

Taking the z -derivative of Equation 3.10, the horizontal Laplacian of Equation 3.16, using the results in Equations 3.12 and 3.18, rearranging terms to eliminate the time derivative and using the QG assumptions of constant planetary vorticity (f_0) and horizontally constant stability, the quasigeostrophic equation for vertical velocity is obtained (omega-equation):

$$\left[f_0^2 \frac{\partial^2}{\partial z^2} + N^2 \nabla^2 \right] w = f_0 \frac{\partial}{\partial z} (\mathbf{V}_g \cdot \nabla \zeta_g) + \frac{g}{\rho_0} \nabla^2 (\mathbf{V}_g \cdot \nabla \rho) \quad . \quad (3.19)$$

or, in terms of the geostrophic vorticity defined in Equation 3.11:

$$\left[f_0^2 \frac{\partial^2}{\partial z^2} + N^2 \nabla^2 \right] w = f_0 \frac{\partial}{\partial z} \left[\mathbf{V}_g \cdot \nabla \left(\frac{1}{f_0 \rho_0} \nabla^2 p \right) \right] + \frac{1}{\rho_0} \nabla^2 \left[\mathbf{V}_g \cdot \nabla \left(-\frac{\partial p}{\partial z} \right) \right] \quad . \quad (3.20)$$

Equation 3.20 shows that vertical motion can be diagnosed (no time derivatives) from the instantaneous pressure field only, since this variable determines both the geostrophic currents and the geostrophic relative vorticity in the QG framework. The term on the left hand side contains only second derivatives of vertical velocity; for disturbances

with wave-like character, it is proportional to $-w$. The contribution of each of the terms on the right hand side of this equation to the vertical motion will be discussed in section IV.B.

The data available for this study is a snapshot of the density field, with considerable detail in both the vertical and the horizontal (after the analysis described in section II.B). This is an ideal situation for the application of Equation 3.19 for the computation of vertical motion. However, it presents some problems because the forcing terms on the right hand side (differential vorticity advection and Laplacian of thickness advection) sometimes tend to cancel each other, leading to errors in the numerical procedure to compute the response on the left hand side. A more stable alternative, the \mathbf{Q} -vector form, was introduced by Hoskins *et al.* (1978):

$$(N^2 \nabla^2 + f_0^2 \frac{\partial^2}{\partial z^2}) w = 2 \nabla \cdot \mathbf{Q}, \quad (3.21)$$

where

$$\mathbf{Q} = \frac{g}{\rho_0} \begin{bmatrix} \frac{\partial \mathbf{V}_g}{\partial x} \cdot \nabla \rho \\ \frac{\partial \mathbf{V}_g}{\partial y} \cdot \nabla \rho \end{bmatrix}. \quad (3.22)$$

This form of the ω -equation (Equation 3.21 above is the so-called Trenberth form, where deformation terms arising from taking the Laplacian of a product have been neglected) shows that a convergent \mathbf{Q} -vector field implies upward vertical motion. Moreover, the vectors themselves are parallel to the ageostrophic velocities responsible for the vertical motion. This \mathbf{Q} -vector form presents additional advantages since the forcing term is exact within the QG context. Neglecting the deformation terms could be a source of error in the vicinity of strong jets or frontal systems (Carlson, 1991), however that is not a problem in the present case because even a coastal jet has sufficiently small velocity magnitudes in an eastern boundary current. The forcing functions can also be evaluated on a single level surface.

Several aspects of the QG assumptions can cause the results from the ω -equation to be either under- or over-estimated. The departures from QG arise in regions where: 1) diabatic effects are strong; 2) static stability is not constant in the horizontal; and 3) ageostrophic motions due to curvature are so strong that neglecting ageostrophic

advection becomes an important source of error. The relative importance of these terms will be considered in the discussion of the QG results (section IV.B).

The ω -equation was solved using both the original MQ-B analyzed density field, and the dynamically balanced density field resulting from the DFI procedure of section III.A.4, to compute the forcing (right hand side of Equation 3.21). In both solutions the condition of $w=0$ on all boundaries was used.

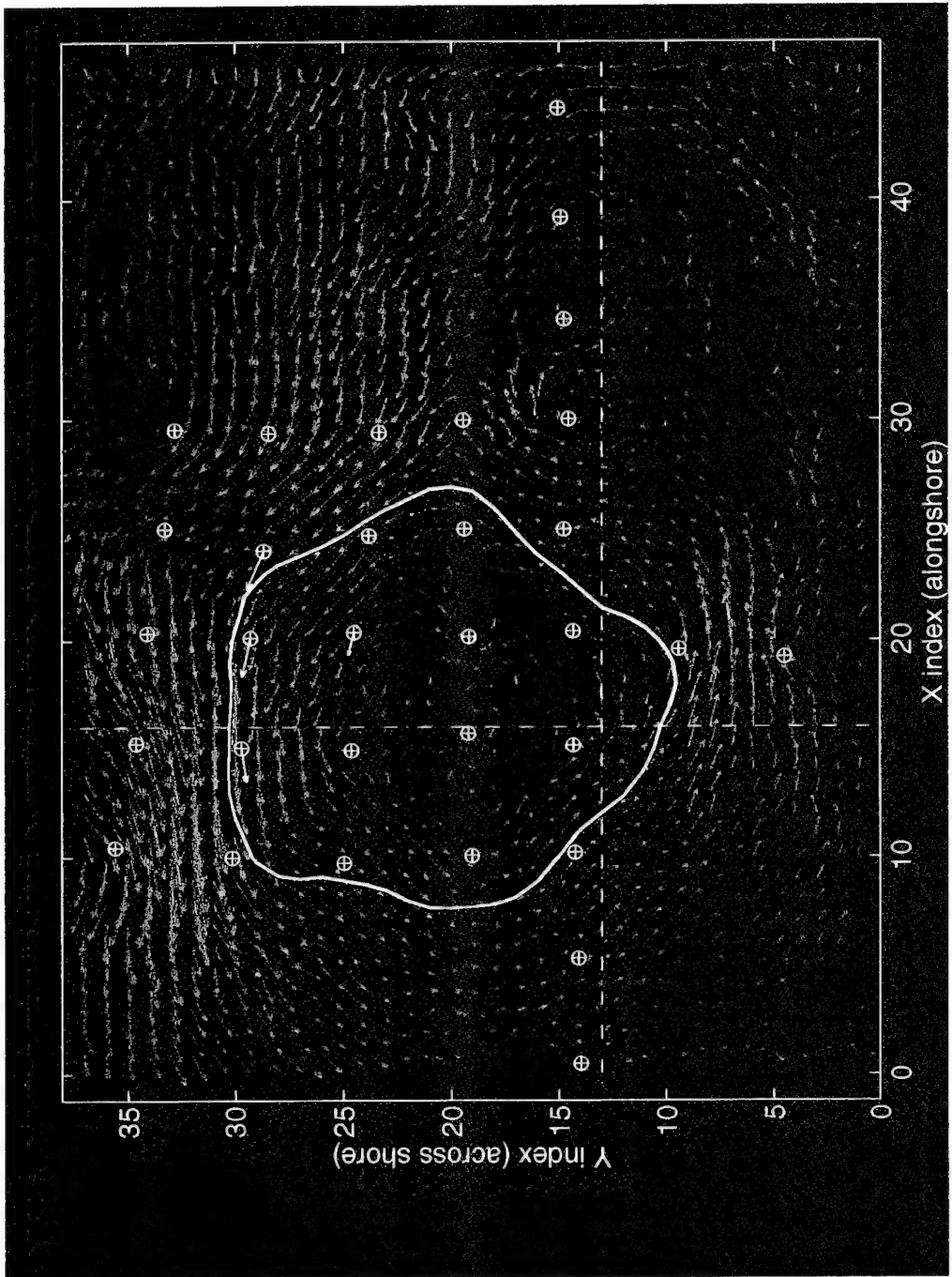


Figure 7. Horizontal cross section of the dynamically balanced horizontal velocity field at a depth of 100 m, in cm/s (red arrows). The longest arrow is about 50 cm/s. The symbol \oplus represents the CTD stations. The yellow arrows are the current vectors from the current meters at the same depth (stations 7, 8, 9 and 13). The white line is a streamline of the nondivergent component of the velocity. The dashed lines are included for reference and represent the vertical cross-sections shown in other figures.

The mean flow is not circular around an hypothetical eddy center; instead, it has meanders, with at least five well defined troughs. These smaller scale features (hereafter *sub-eddy* scales) have been found in other systems, particularly in frontal systems (e.g., Fiekas *et al.*, 1994) where submesoscale circulations are part of the mesoscale meandering of the front itself. This finding is partly corroborated by an inspection of Figure 1. This figure shows several feeder bands of water being entrained into the eddy circulation, suggesting that the pattern of motion around the eddy is not completely circular.

A comparison was made between the DFI solution of the horizontal velocities and the currents observed by the hull mounted ADCP (section II.A.2). Figure 8 shows a horizontal map of the dynamically balanced horizontal currents and the horizontal ADCP vectors for the bin centered at 100 m depth. In general, the DFI solution and the ADCP currents compare well in magnitude and direction. This is especially so in the northeast, northwest and southwest parts of the domain, even though the DFI solution in the northeastern part of the domain (upper side in Figure 8) presents some undesirable effects from the flat bottom assumption (see below). The region to the southeast of the eddy is an area where practically no CTD observations were made, and thus the solution is almost entirely dominated by the performance of the MQ-B method in data void areas, which was said earlier to be very benign. This means that the density gradients observed by the CTD stations at the southeast edge of the eddy become smaller and smaller as a function of distance from the eddy, and the general circulation will therefore tend to remain weakly cyclonic. An exception is the small anticyclonic feature centered at (31,15), which is persistent in the DFI results down to several hundred meters and was never sampled by the ADCP (results not shown). Since this position coincides with a CTD station, the resulting anticyclonic circulation is the response to the observed density gradients between stations 22, 21 and 30, extending quite deep.

In the analysis of Figure 8 it should also be kept in mind that the ADCP observes the total velocity with a measurement uncertainty that is highly variable and, in most cases, of the same order of magnitude of the signal that is being computed in the DFI solution (the ageostrophic part of the flow). Also, the DFI solution is representative of the slow mode at the time of the observations, whereas the ADCP is observing all frequencies. The ADCP data plotted in Figure 8 was spatially averaged, resulting in effective time averages that range from 15 minutes to about 2 hours.

The meanders in the mean flow have a distinct field of vertical motion associated with them. This is visible in Figure 9 which shows the vertical velocity at 100 m (colored

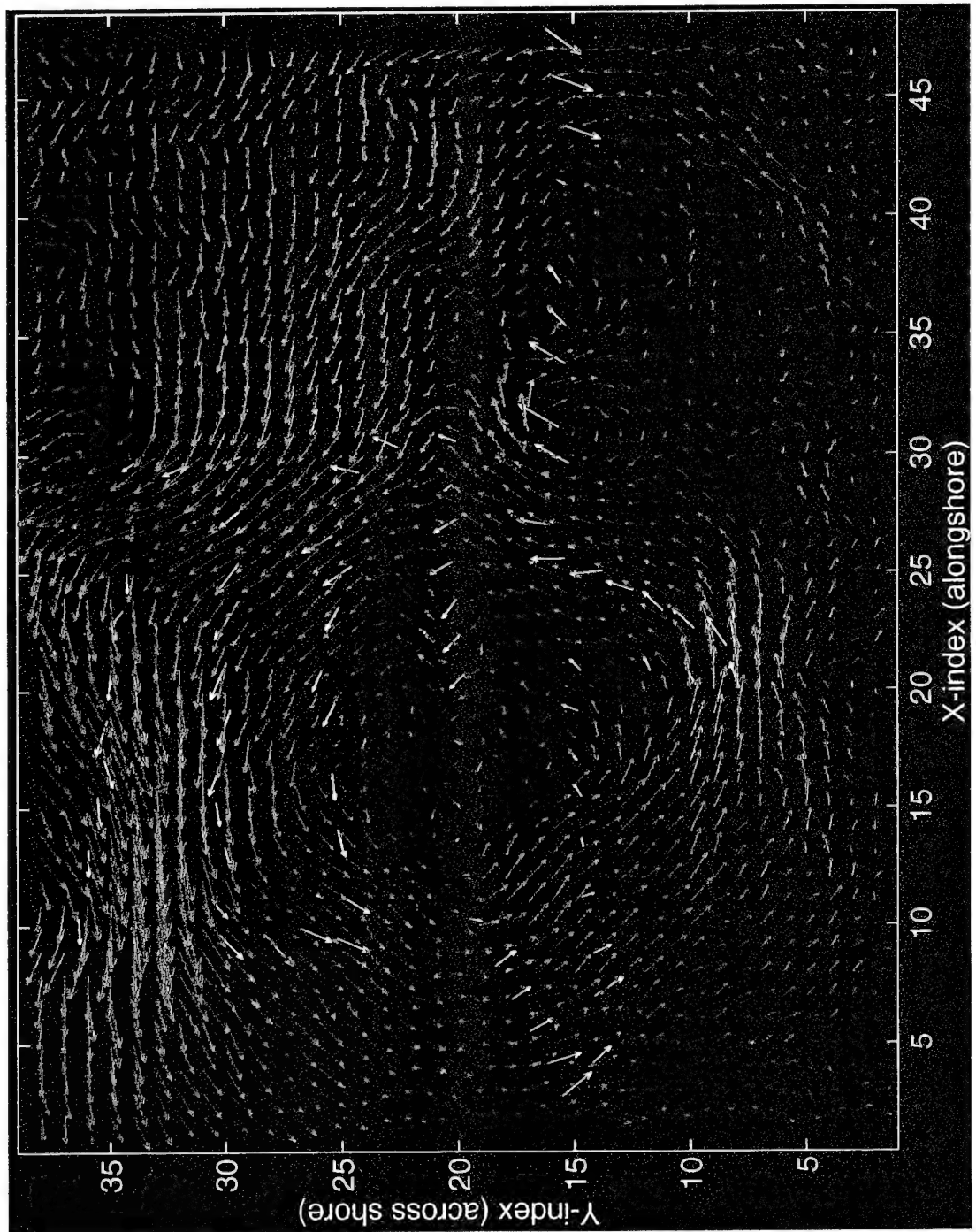


Figure 8. Horizontal cross section of the dynamically balanced horizontal velocity field at a depth of 100 m, in cm/s (red arrows), with superimposed ADCP horizontal velocities for the depth bin centered at 100 m (yellow arrows).

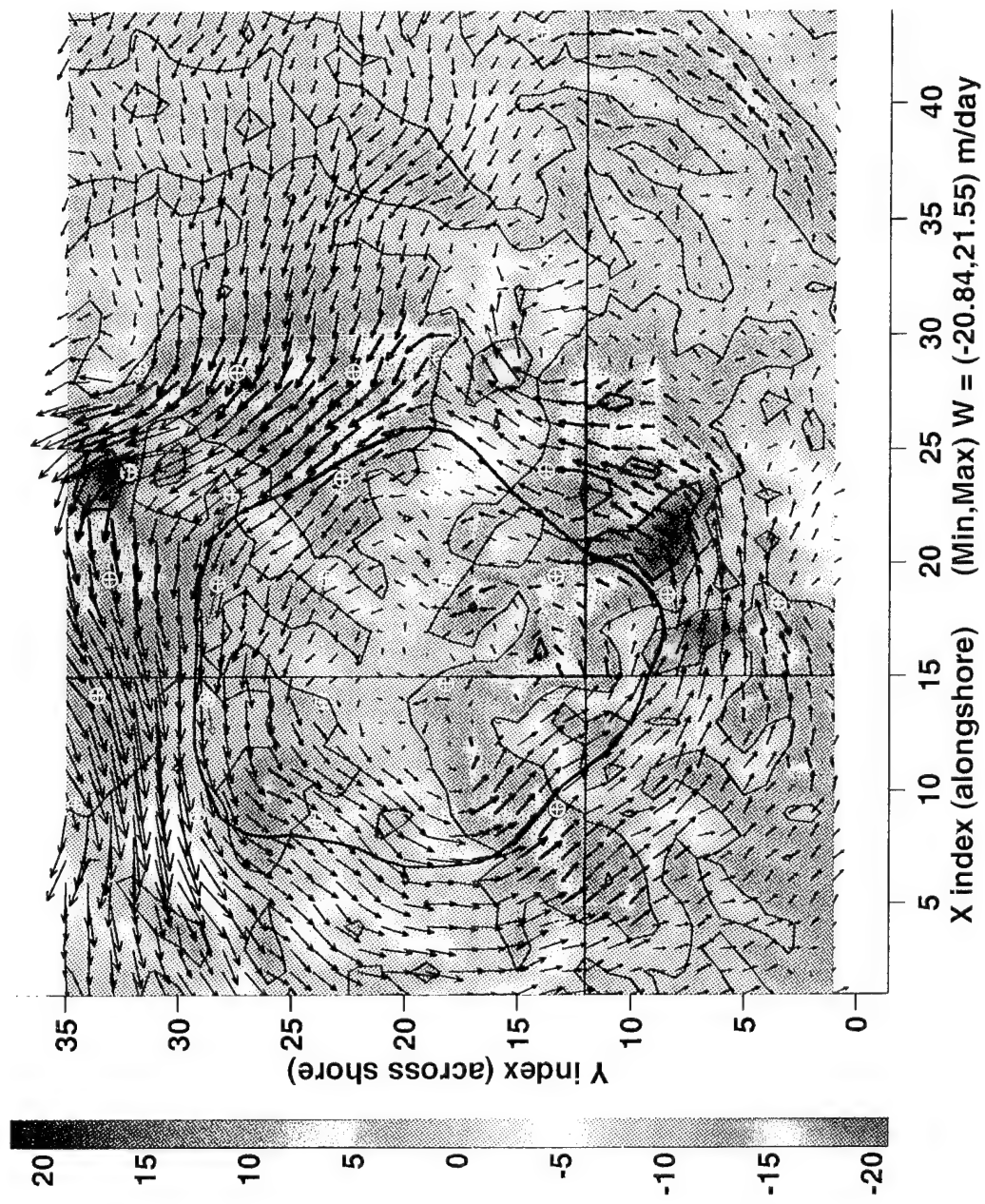


Figure 9. Horizontal cross section of the dynamically balanced vertical velocity field at a depth of 100 m, in m/day (colored field), with superimposed horizontal velocities at the same level. The symbol \oplus represents the CTD stations. The red arrows are the current vectors from the current meters at the same depth (stations 7, 8, 9 and 13). The black bold line is a streamline of the nondivergent component of the velocity. The black thin lines are included for reference and represent the vertical cross-sections shown in other figures.

field) with the horizontal velocity (black arrows) and the same streamline as in Figure 7 superimposed. The w field is distributed mostly around the eddy in patches of radially aligned, alternating upwelling and downwelling centers, with maximum vertical velocities at this level of about ± 20 m/day. The average vertical velocity within a radius of 35 km from the center of the eddy, however, is in the order of 0.1 m/day.

These sub-eddy scale patches of rising and sinking motion are related to meanders in the otherwise circular eddy and can be explained by QG theory by considering the changes of vorticity in a water parcel following the fluid through the meanders (Holton, 1979). Figure 10 shows a typical meandering system with cells of negative and positive

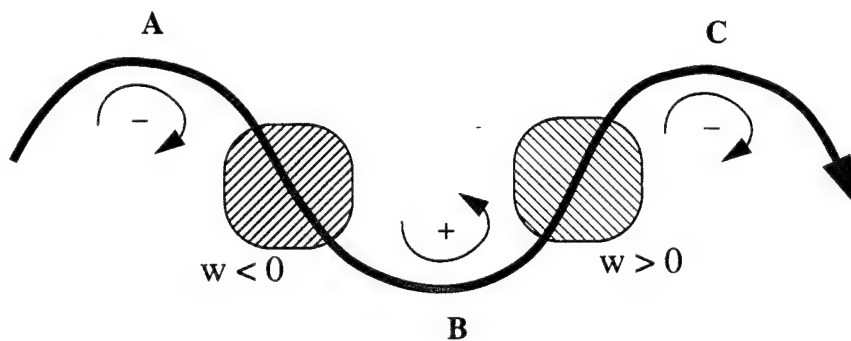


Figure 10. Meandering jet with alternating patterns of negative (regions A and C) and positive (region B) vorticity. The changes of vorticity going from A to B to C cause downwelling upstream of the trough and upwelling downstream of the trough.

vorticity. In region A , the parcel acquires negative relative vorticity; as it moves to region B , it encounters regions of increasing relative vorticity. The QG vorticity equation (Equation 3.10) can be written:

$$\frac{d\zeta}{dt} = -f \nabla \cdot \mathbf{V} = f \frac{\partial w}{\partial z}. \quad (4.2)$$

Hence, from A to B the left hand side of Equation 4.2 is positive; with zero boundary condition at the surface, the right hand side shows that w is negative at depth, that is, from A to B there is sinking motion. If the meander is not growing or decaying, the zero vertical velocity point will be exactly at the trough, because in this case the left hand side is zero there.

The opposite happens as the parcel moves from region *B* to region *C*; the change in the relative vorticity of the parcel is now from positive values to negative values, causing the left hand side of Equation 4.2 to be negative. Using the same boundary condition on the right hand side a positive value for the vertical velocity is now found at depth. Thus an upwelling cell lies between region *B* and region *C*. The flow is thus three-dimensional, with the particle describing not only the meanders in the mean flow but also some vertical excursion in both senses (up and down). In this simple but illustrative model the vertical displacement of the particle is:

- inversely proportional to the magnitude of the horizontal mean flow between *A* and *B* or between *B* and *C*;
- directly proportional to the magnitude of the vertical velocity.

The second factor is proportional to the rate of change of vorticity following the motion and the depth over which the vorticity change occurs. All else being equal, large vertical scales tend to have stronger vertical velocities. In the Gulf Stream meanders, for instance, vertical motions of 100 to 200 m/day have been found (Lindstrom and Watts, 1994). In this region the vertical motion may be enhanced by the large density gradients across the meanders, which cause the changes in vorticity to take place over appreciable changes in water column depth, even for small displacements from the jet axis. The rate of change of vorticity is largest in regions of strong changes in curvature, i.e., for smaller horizontal scales.

The upwelling and downwelling patterns described above can be identified in Figure 9. The patches of vertical motion are correlated with the meanders of the mean flow depicted by the streamline, with downwelling upstream and upwelling downstream of the troughs. Similar patterns of vertical motion have been identified in the meanders of the Gulf Stream (Leach, 1987; Bower and Rossby, 1989; Bower, 1989). The relative magnitudes of the horizontal and vertical velocities also show that the vertical excursion of the water parcels in these patches is small. A typical horizontal length scale for the patches is about 20–25 km. This distance is covered in about 15 hours at a speed of 40 cm/s; in 15 hours a parcel moving at this speed will be displaced a maximum of only 12 m in the vertical.

Another important aspect of the description of this eddy is its vertical extension. This can be appreciated in Figures 11 and 12. The former is a vertical cross-section of the vertical velocity along the x-axis (alongshore), corresponding to the horizontal line in Figure 7; the latter is a cross-section of the vertical velocity along the y-axis (across shore), corresponding to the vertical line in Figure 7. Both have units of m/day, although the color

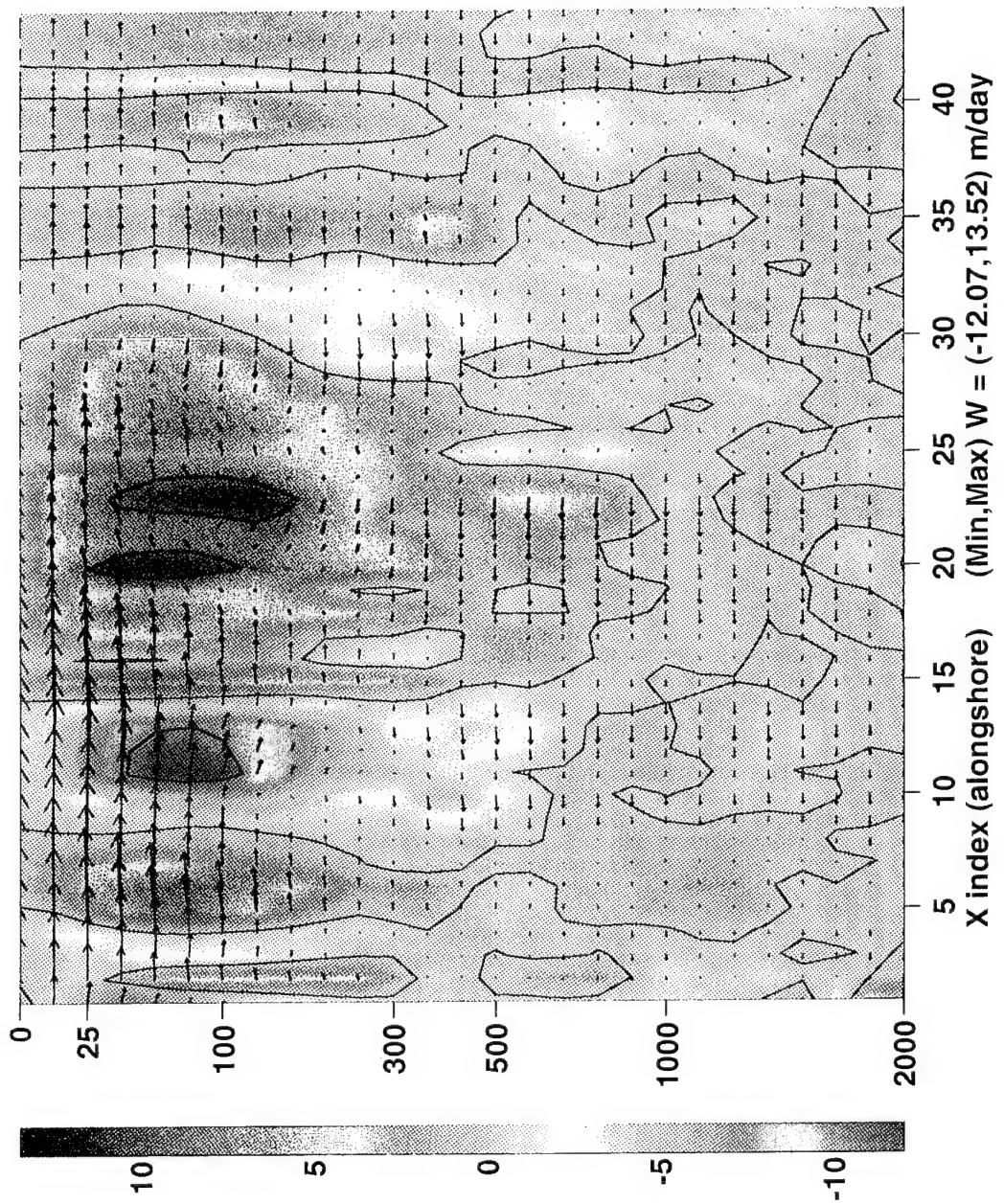


Figure 11. Vertical cross section of the dynamically balanced vertical velocity (colored field) in the alongshore direction (from the northwest (left) to the southeast (right)), in m/day, with depths in meters. Also shown are the two-dimensional (u, w) vectors in the same section (black arrows). Note that the vertical axis is not linear.

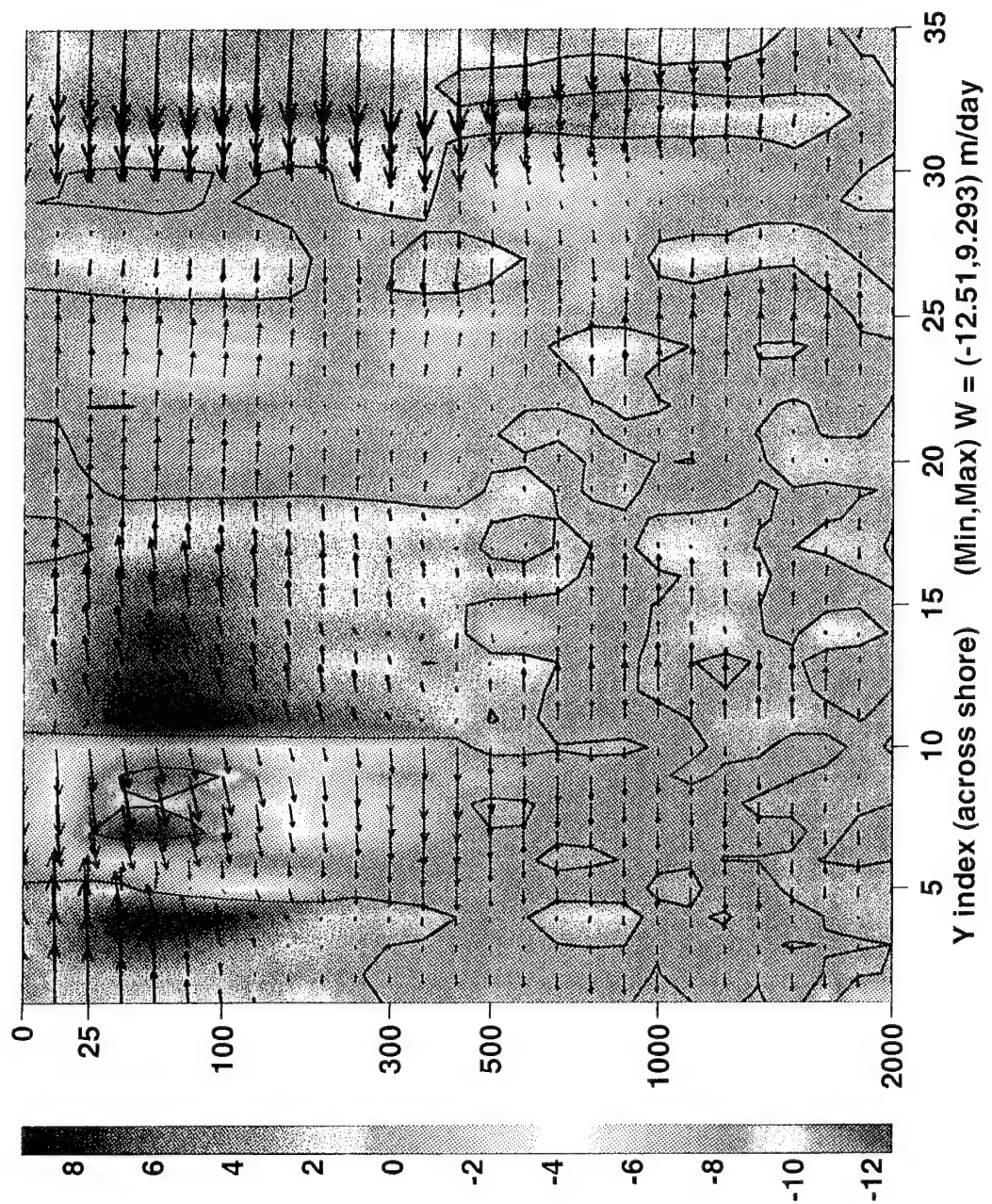


Figure 12. Vertical cross section of the dynamically balanced vertical velocity (colored field) in the across shore direction (offshore to the left), in m/day, with depths in meters. Also shown are the two-dimensional (v, w) vectors in the same section (black arrows). Note that the vertical axis is not linear.

scale is not the same in the two figures; also, note that the vertical axis is not linear (the top 500 m take about half the axis). The vertical extent of the eddy is shown to be about 500 m (extending in some points to almost 1000 m), with maximum vertical velocities occurring between 50 and 150 m depth. The patches of rising and sinking motion are not uniquely related to divergence and convergence of the along-section vectors superimposed on the figures because there may be compensation in the across section flow. However it can be seen that the strong local maxima of rising motion generally have associated with them divergence of the velocity vectors above and at the same level while the local minima are generally associated with convergence above and at the same level.

It is also noticeable that in Figure 12 there are large horizontal vectors in the far right of the figure, that is, the boundary of the model closer to shore. This northeastern boundary, and the northwestern boundary, are regions of strong tangential velocities, at least in the upper levels as can be seen in Figures 1 and 7. This causes some problems at the boundary, which use an advective velocity based only on the normal flow in the boundary condition (section III.A.3). Furthermore, this is also the region where the Helland-Hansen method was used to extend the inshore CTD profiles to a common maximum depth (section II.B), thus introducing horizontal density gradients that may not be real. These horizontal gradients cause unrealistic vertical shear in the horizontal velocities through the thermal wind relations. For these reasons, the model results in the northeastern part of the domain and closer to the shore may not be reliable, and the discussion is therefore limited to regions where the joint effect of boundary and missing topography is clearly nonexistent or minimized.

2. Geostrophic adjustment

It was mentioned in the preceding section that the results described above were obtained with the DFI procedure in a model whose initial baroclinic velocity field is geostrophic. Another possibility is to set the baroclinic currents to zero at the initial time. This different initial condition will also yield a final slow mode; the choice between one and the other is related to the process of geostrophic adjustment itself.

Geostrophic adjustment is the process by which an initial disturbance in a rotating fluid releases part of its potential energy into kinetic energy, until a steady equilibrium is achieved (Gill, 1982). The real ocean is in a constant process of geostrophic adjustment due to multiple forcing. In a simulated ocean without forcing, the geostrophic adjustment takes

place during the spin-up phase, where the imbalance between the initial density and mass fields is geostrophically adjusted. During the process, about one third of the released potential energy is converted to kinetic energy of the equilibrium solution, and the remaining two thirds are dissipated in inertial oscillations around the equilibrium state or propagated away in the form of gravity waves. This equilibrium state is an approximate geostrophic balance, that is, the equilibrium state is not found by solving the steady-state geostrophic equations. For a rotating eddy, the equilibrium is an approximate gradient balance between the Coriolis terms, the pressure gradient terms and the acceleration (curvature) terms.

The initial disturbance can be thought of as containing a variety of length scales; the way the geostrophic adjustment affects each of these scales is determined by an important horizontal length scale, the *Rossby radius of deformation* (Rossby radius), given by:

$$R_d = \frac{c}{|f|} \quad (4.3)$$

where c is the phase speed of the disturbance and f is the Coriolis parameter. For scales much smaller than the Rossby radius, rotation effects are negligible because the pressure gradient is much larger (short waves behave as gravity waves and disperse momentum rapidly from the initial disturbance), whereas for scales comparable to or larger than the Rossby radius, rotation effects are of the same order of magnitude of the pressure gradient (long waves become inertial oscillations and propagate much slower). The time scale of the adjustment process is the inertial period ($2\pi/f \approx 19$ h at 38.6°) at a distance from the initial disturbance comparable to the Rossby radius, but allowance has to be made for the oscillations about the equilibrium state.

The considerations above can be completed with an analysis of the non-dimensional potential vorticity associated with the initial disturbance (Gill, 1982):

$$\frac{\partial}{\partial t} \left(\frac{\zeta}{f} - \frac{\eta}{H} \right) = 0 \quad (4.4)$$

derived from the shallow water equations:

$$\begin{aligned} \frac{\partial u}{\partial t} &= -g \frac{\partial \eta}{\partial x} + fv \\ \frac{\partial v}{\partial t} &= -g \frac{\partial \eta}{\partial y} - fu \\ \frac{\partial \eta}{\partial t} + H \left(\frac{\partial u}{\partial x} + \frac{\partial v}{\partial y} \right) &= 0 \end{aligned} \quad (4.5)$$

where η is the surface elevation and H is the water column depth.

The Rossby radius is the length scale at which, for geostrophic motion, the potential vorticity terms in Equation 4.4 are of the same order of magnitude; short waves are dominated by the vorticity term, whereas long waves are dominated by the pressure perturbation term ($p' = g\rho\eta$). The term including η is related to changes in the mass (pressure) field; the term including ζ is related to changes in the velocity field. Therefore, for an initial potential vorticity that must be conserved during the adjustment, the process takes place differently, and the final state is different, depending on the scale of the disturbance compared to the Rossby radius. For scales smaller than the Rossby radius, where gravity is the main restoring force, the final relative vorticity dominates the potential vorticity, and the mass field adjusts to be in geostrophic balance with the resulting velocity field. For scales comparable to or larger than the Rossby radius, where rotation is comparable to gravity, the final mass field dominates the potential vorticity, and it is the velocity field that adjusts itself to a geostrophic balance with the mass field. This is illustrated in Figure 13.

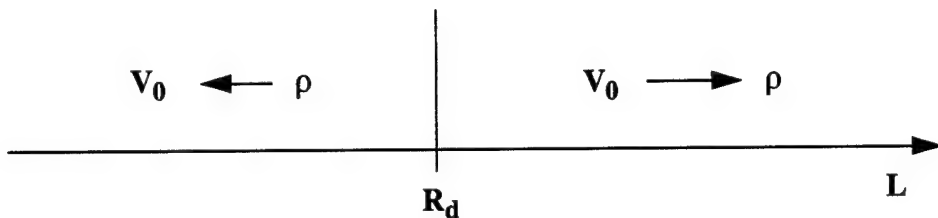


Figure 13. Relation between the mass and velocity fields during the geostrophic adjustment, according to the length scale (L) relative to the Rossby radius of deformation (R_d). V_o is the initial velocity field and ρ is the initial mass field.

Thus it is seen that the choice of the initial velocity field is an important issue for scales smaller than the Rossby radius. The density field is not the proper information with which to describe these scales, because it adjusts to the velocity field. Observations of the velocity field at small scales must be available if these scales are to be initialized in a circulation model. For scales comparable to or larger than the Rossby radius, description of the mass field is sufficient information, and the velocities adjust to reach geostrophic equilibrium with the observed mass field. Selecting an initial velocity field is not critical for these scales; the difference between starting with geostrophic initial velocities or zero

initial velocities is reflected only in some damping of the density field in the latter case, because more energy is extracted from the initial disturbance to spin-up the velocity field.

The DFI results reveal meanders with horizontal length scales of 20 to 25 km; to determine whether they are influenced by the specification of the initial velocity field or not, an estimate of the Rossby radius is needed. In a continuously stratified fluid, with a vertical scale much smaller than the horizontal scale and no variations in bottom topography, the *normal modes* solution to the motion can be applied, based on a separation of variables between depth independent horizontal information and horizontally independent vertical structure. Each normal mode has its own vertical structure and behaves like an equivalent homogeneous system with depth H_e (equivalent depth).

The first mode (or mode zero) is the barotropic mode with equivalent depth equal to the total depth of the water column. For systems predominantly baroclinic, the vertical structure of the higher order modes is more useful. The normal modes (barotropic and baroclinic) can be found by solving the following eigenvalue problem (Kundu, 1990):

$$\frac{d}{dz} \left(\frac{1}{N^2} \frac{d\psi_n}{dz} \right) + \frac{1}{c_n^2} \psi_n = 0 \quad (4.6)$$

where N^2 is the depth dependent buoyancy frequency, ψ_n is the vertical structure function of any variable, c_n^2 is a separation constant with units of velocity (reciprocal of the eigenvalues) and n is the mode number. This equation was solved for the normal modes of vertical velocity, using an average profile for the buoyancy frequency computed from all the CTD casts in the cruise assuming a maximum common depth of 2000 m, with specification of appropriate boundary conditions for the vertical function (rigid lid at the surface and bottom):

$$\psi_n = 0, \quad z = 0, -H. \quad (4.7)$$

The modal shapes for the first four baroclinic modes for vertical velocity are shown in Figure 14. The first mode contains about 20% of the total fit distributed by all the resolved modes (250). The other modes contribute less than 6% to the total fit. A comparison of Figure 14 with Figure 11 shows that the first mode describes well the region of maximum vertical velocities between 50 and 300 m; a combination of the remaining modes can account for the maximum extension of the eddy, varying from 500 to about 1000 m.

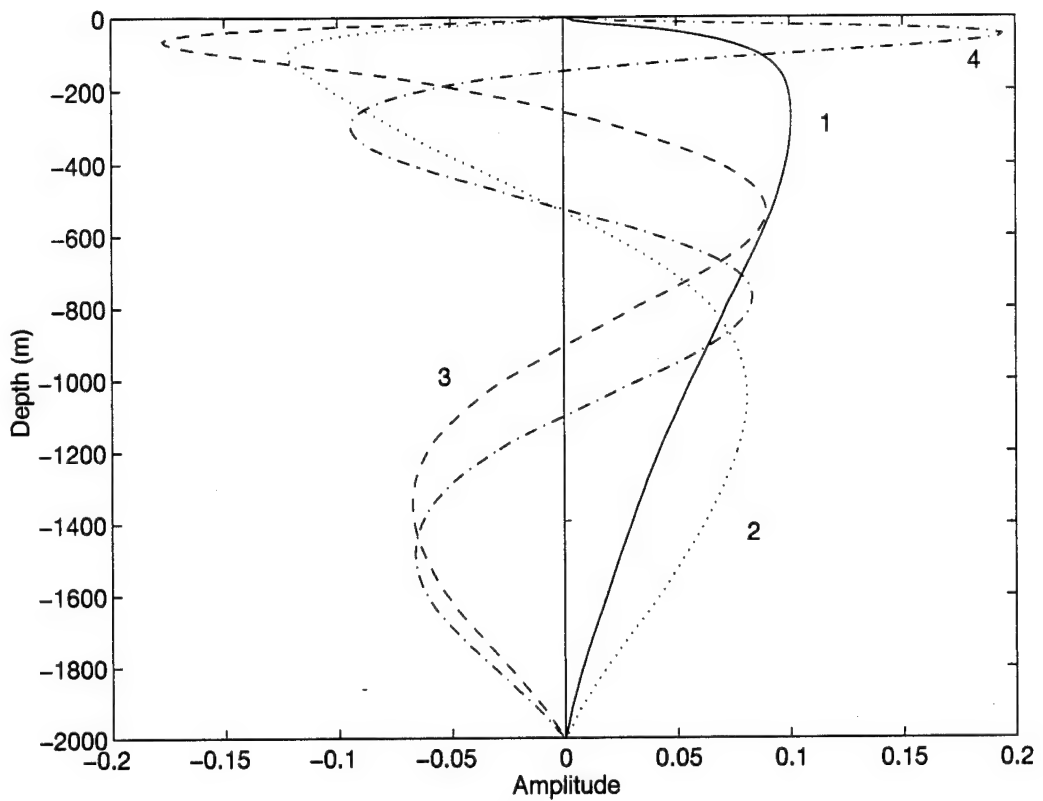


Figure 14. Normalized modal shapes for vertical velocity computed from the mean stratification.

Each of the resolved modes has a corresponding eigenvalue ($\lambda = 1/c_n^2$) from which the associated internal Rossby radius can be computed:

$$R_d = \frac{c_n}{f}. \quad (4.8)$$

Table 3 lists the results for the first three baroclinic modes.

Mode No.	λ	C_n (m/s)	R_d (km)
1	0.235	2.06	23
2	1.070	0.97	11
3	2.474	0.64	7

Table 3. Characteristics of the First Three Baroclinic Modes

The first internal or baroclinic Rossby radius of deformation is the horizontal length scale associated with coastal phenomena, such as upwelling and meandering jets, and eddies (Gill, 1982). These results are in good agreement with the estimates of the Rossby radius off the coast of Oregon, given in Kundu *et al.* (1975), obtained with a similar method to the one described above (decomposition into normal modes).

It follows from the above that it is reasonable to assume that the vertical motion associated with the meanders observed in the mean flow has a vertical structure dominated by the first mode, which has a Rossby radius of 23 km. The length scales of the up- and downwelling patterns shown in Figure 9 are comparable to the Rossby radius. Thus, during the model initialization, it is the velocity field that primarily adjusts to the observed density field at the scales of the meanders.

Therefore, the choice of the initial condition for the velocity field is not critical to achieve the same qualitative results from the model (meandering of the mean flow, with associated patches of rising and sinking motion). This is illustrated in Figure 15, which shows the vertical velocity at 100 m depth, obtained with zero vertical shear in the initial velocity field as opposed to the geostrophic shear used to obtain the results shown earlier. Comparing this figure with Figure 9, it is seen that the same patterns of vertical motion are found with the different initial velocity field, as expected. Another result that is consistent with the considerations above is the weaker magnitudes of the motion, which are decreased by more than 50 % at this level relative to the results in Figure 9. Figures 16 and 17 show that the vertical extent of the vertical motion cells is also somewhat smaller when the initial velocity field has no shear. The same qualitative agreement with the corresponding Figures 11 and 12 is clear, but the regions of rising and sinking motion now show weaker maximum and minimum vertical velocities in each section.

The question then arises as to which set of initial conditions yields results closer to reality, from a quantitative point of view. The results obtained when the initial velocity field is assumed geostrophic show a better agreement with observed currents. To set the initial shear velocities to zero is equivalent to saying that no *a priori* knowledge is available about the expected velocities in the eddy. However, scaling arguments can show that the eddy should be in a quasigeostrophic balance with the observed mass field (the Rossby number is of order 0.1), therefore since no detailed observations of the initial velocity field are available, assuming initial geostrophically balanced currents seems the better assumption.

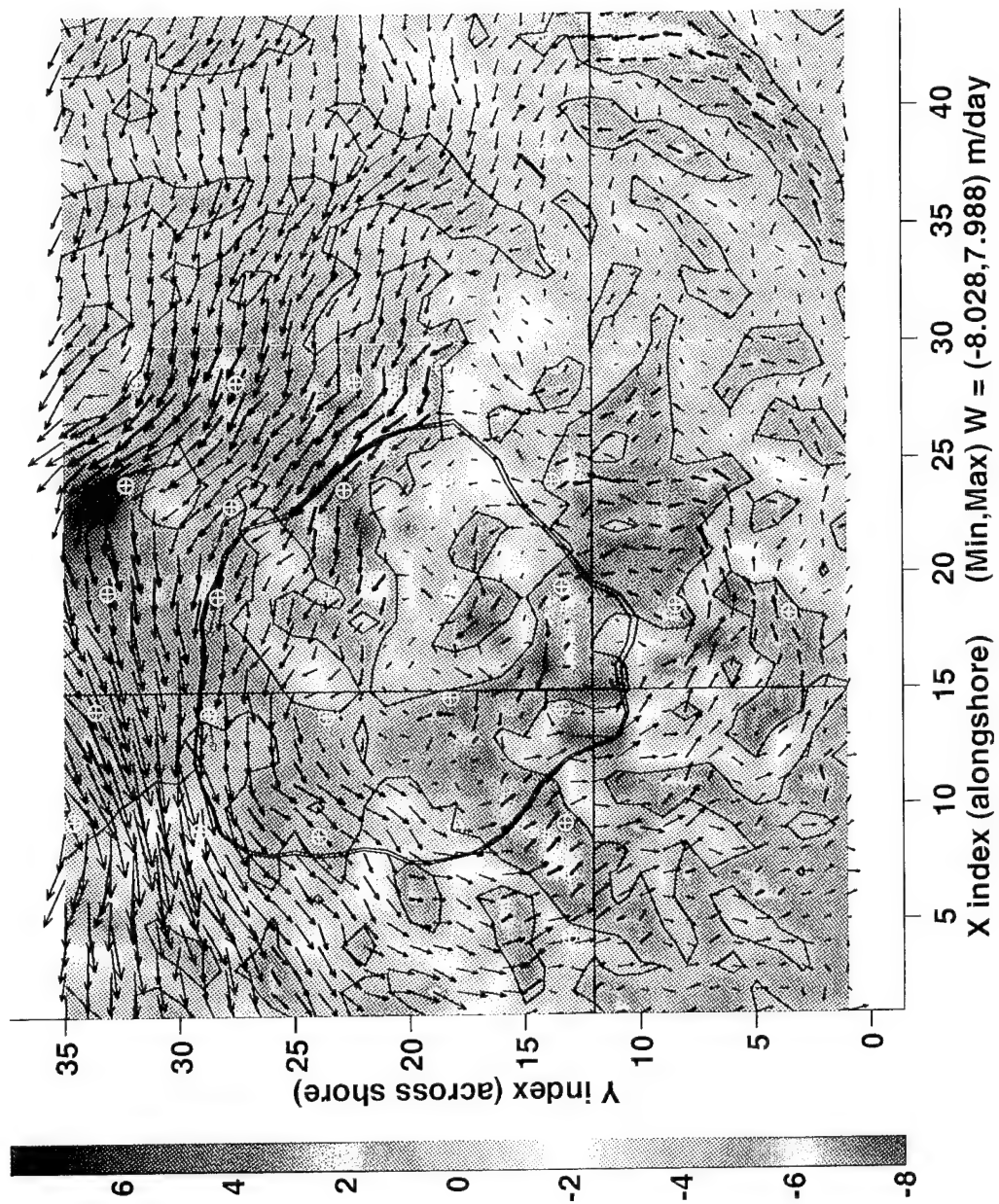


Figure 15. Same as Figure 9, but obtained with an initial velocity field with no vertical shear.

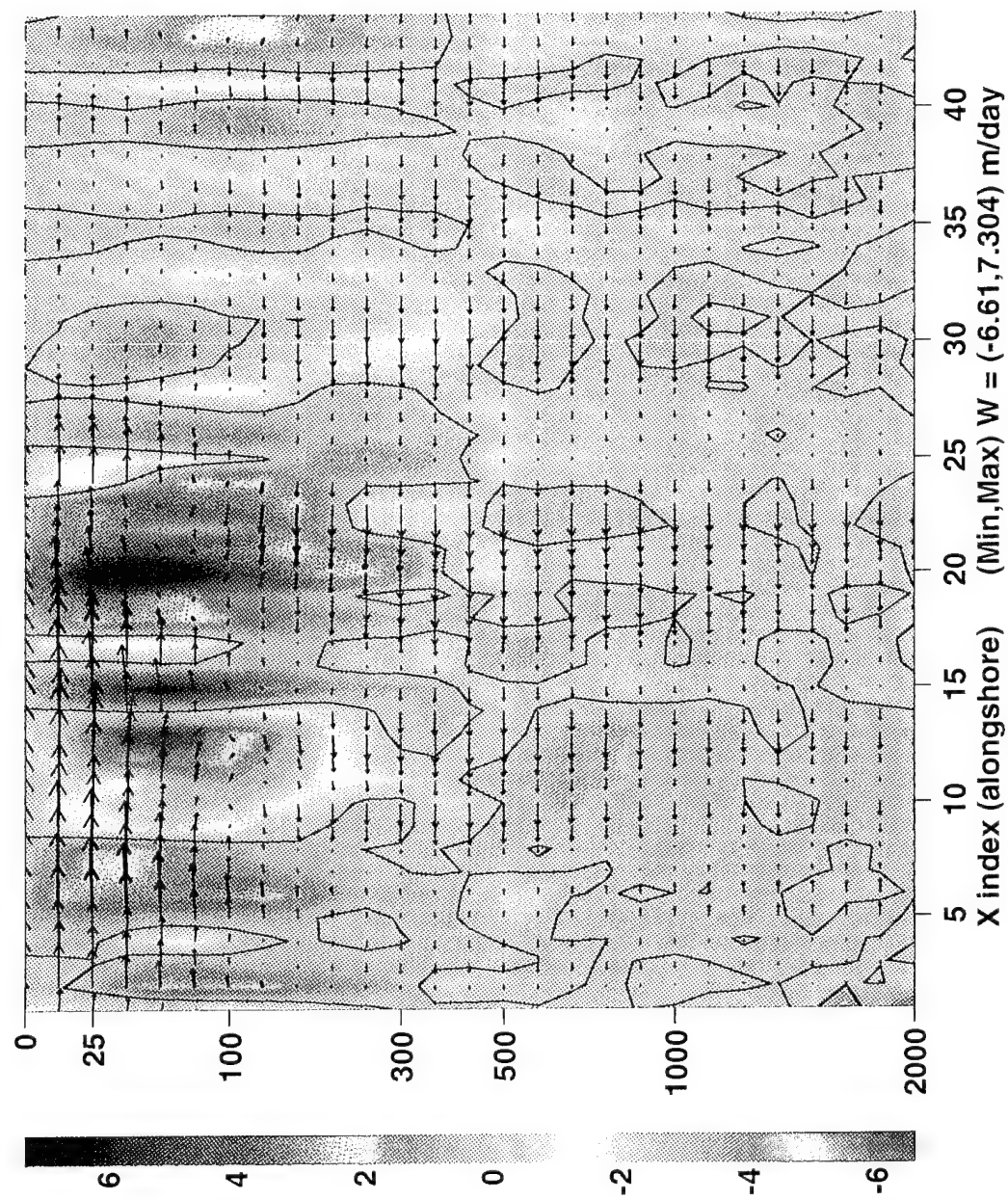


Figure 16. Same as Figure 11, but obtained with an initial velocity field with no vertical shear.

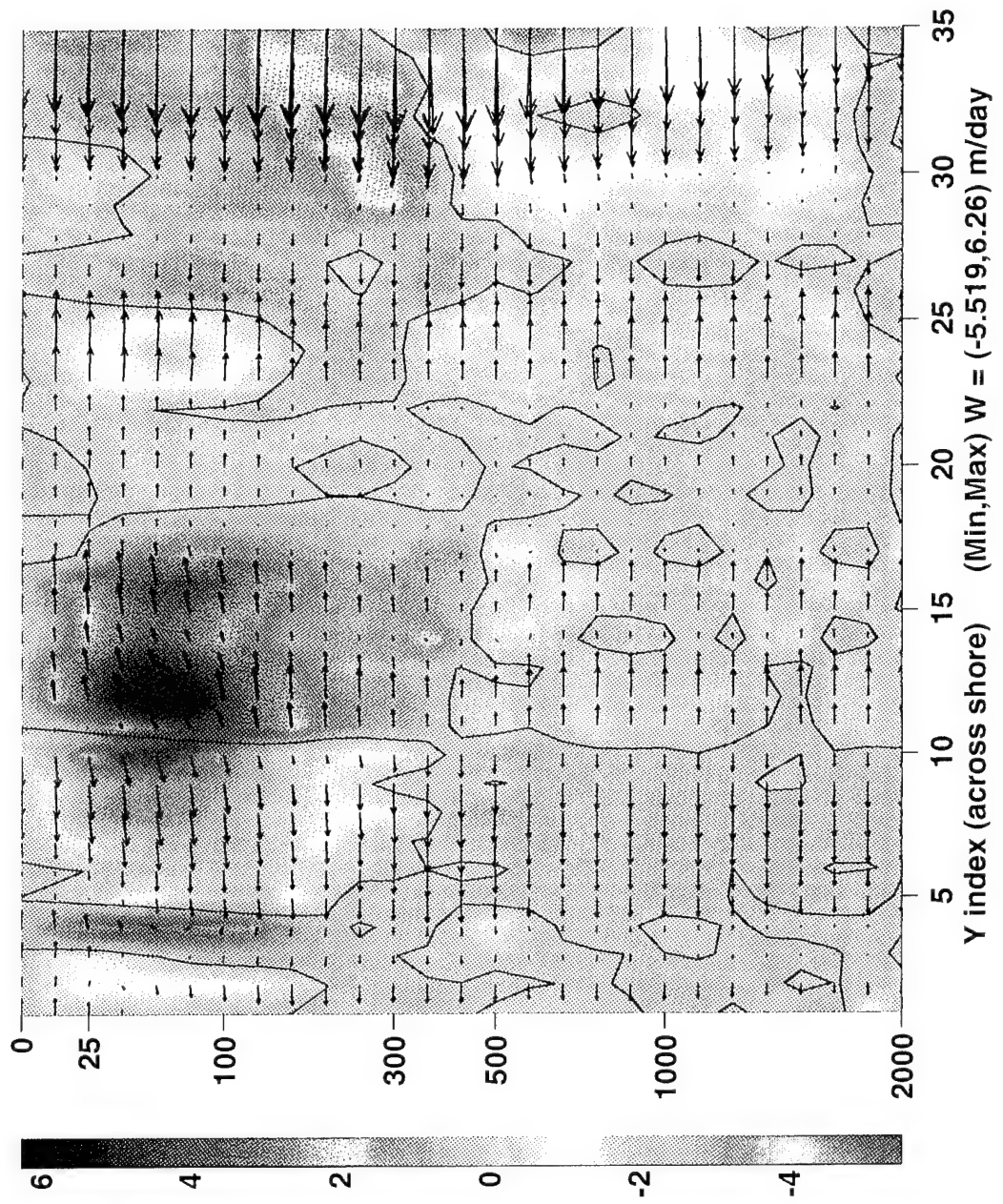


Figure 17. Same as Figure 12, but obtained with an initial velocity field with no vertical shear.

3. Data related problems

The underlying assumption in the data analysis described in section II.B is that the CTD stations (plus the four SAIL stations and the satellite data) are synoptic. This is a common assumption in oceanography, perhaps the only viable solution to the financial constraints and the difficulty of data collection in the ocean. Other authors who have studied meso- and submesoscale phenomena (Fiekas et al., 1994; Strass, 1994; Pollard and Regier, 1992; Le Groupe Tourbillon, 1983) make no particular point of the fact that this basic assumption is made, even though the observations are collected over a number of days or even a week.

The scales of the phenomena being studied are related to the more or less validity of the synopticity assumption. Data collected for large scale phenomena with Rossby numbers much smaller than unity or time scales much larger than the duration of an hydrographic cruise can be considered synoptic without any major argument to the contrary. When the scales being studied are comparable to the duration of the cruise or characteristic length scales of other signals, then the signal-to-noise ratio in the measurements becomes smaller, and aliasing and/or deformation of the scales under analysis may occur.

The CTD data in this cruise took about 3 days to collect. Figure 18 shows the cumulative time interval between the beginning of each cast. The difference in time between any two stations is found by subtracting the numbers between these stations and the immediately preceding stations (for instance, the time interval between stations 16 and 15 is $40.9 - 21.6 = 19.3$ hours. Note that the CTD number sequence –Figure 2– does *not* correspond to the order in which the stations were occupied). The worst case of possible aliasing or distortion occurs when stations are close in space but separated by several hours in time. For example, stations 16 and 15 are apart by about 20 km in space and 19 hours in time. Thus an oscillation in time, uniform over the entire grid, with a period of 38 hours has the potential to explain all of the differences between the observed values at stations 15 and 16. Note that the spatial aliasing problem in this case is solved by sampling theory, i.e., scales smaller than the separation between stations are not resolved.

This section examines two possible sources of error in the data used in this study and tries to draw some, if not quantitative, at least qualitative conclusions on their effect on the results presented in the preceding sections. These possible sources of error are a direct consequence of the lack of exact synopticity in the hydrographic data.

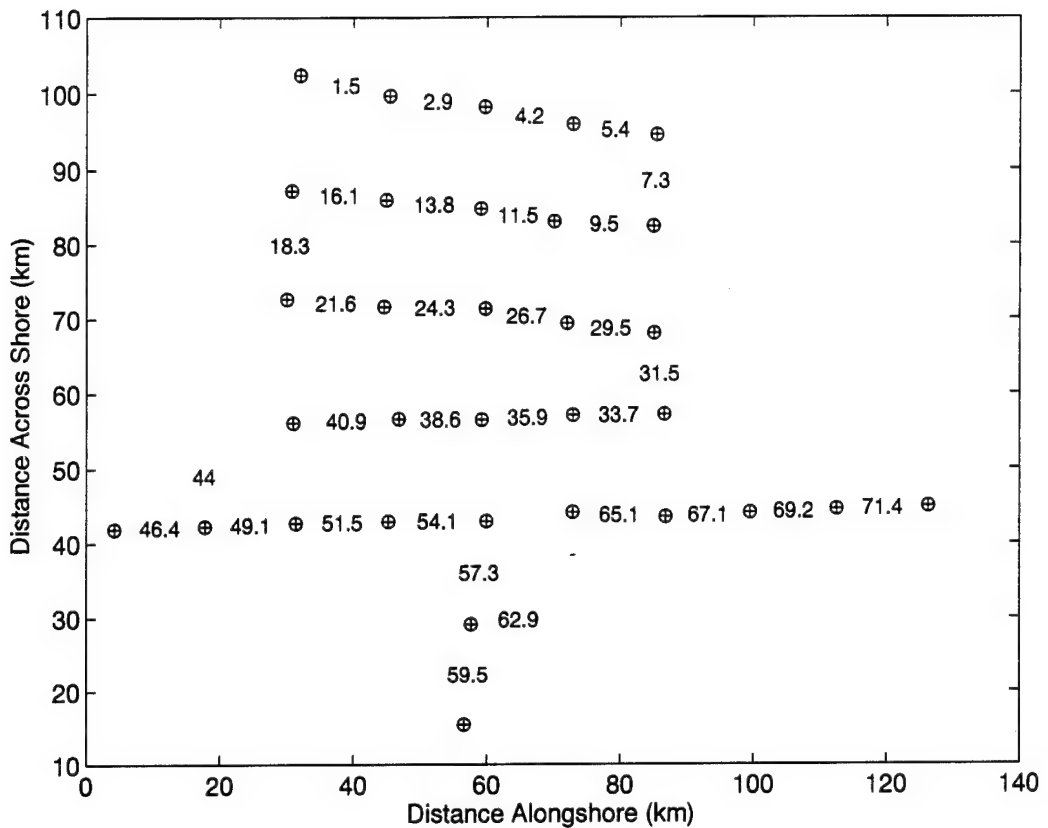


Figure 18. Cumulative time interval between CTD stations, in hours. Refer to Figure 2 for stations numbers (*not* related to the order the stations were occupied).

a. Internal tides

The interaction of the barotropic tidal motions with the coastline at the shelf or slope causes a vertical oscillation of the pycnocline with the same range of frequencies of the tides. These oscillations propagate away from the region of generation as internal waves (internal tides); the amplitude of the internal tides depends on the strength of the forcing, which in turn is a function of the bottom slope, the barotropic tide-induced across shelf velocity and the stratification of the water column (Baines, 1986). Their phase speed is a function of the buoyancy (N) and inertial (f) frequencies.

Internal waves can only exist in the range of frequencies

$$f < \omega < N. \quad (4.9)$$

Hence, the main components of the barotropic tide that are forcing internal tides are semidiurnal. Several authors (e.g., Rosenfeld, 1990) have found that the frequency associated with the largest variance in internal oscillations close to the shore is the one that corresponds to the M₂ component (about 0.08 cycles/hour).

Two theories try to explain the propagation of internal waves. One approach uses ray-like propagation, and explains important phenomena such as reflections from the bottom. Depending on a critical slope angle determined by the wave characteristic

$$c = \left(\frac{\omega^2 - f^2}{N^2 - \omega^2} \right)^{1/2} \quad (4.10)$$

the wave will be either transmitted or reflected (Pond and Pickard, 1983). This can account for the concentration of energy at some depths, as waves are forced to remain at selected levels. Another approach decomposes the oscillation into an infinity of vertical dynamic modes similar to the ones depicted in Figure 14, and can explain the difference in the amplitudes of the oscillations at different depths. Usually the first baroclinic mode describes most of the variance (Rosenfeld, 1990), but other researchers have found that it can take a combination of several of the lowest modes to explain the vertical structure of the internal tide (Chiswell, 1994).

In any case, internal wave dynamics are dependent on such a variety of contributions that the result is a fairly complex system that may or may not be causing problems in the CTD data sampling in this study. The motivation to look at this problem came from the finding of appreciable vertical oscillations in the upper 500 m of the water column, based on CTD casts taken during an anchor station about 350 km off Pt. Arena, thus much farther offshore than the present study region, in August 1993 (Michael Kosro, personal communication). These oscillations had a well marked, vertically coherent semidiurnal character, with vertical displacements of the thermocline of about 10–15 m, (30 m oscillations in the isotherms at 300 m depth). Such a large and organized oscillation at the semidiurnal period, if present in the study region, would undoubtedly affect the observations in the CTD data used in this study.

The only time series available in this study are from the current meter records. The instruments recorded velocity and temperature at several depths (section II.A.2). Unfortunately, the vertical resolution is very poor, and the period covered does not include the time of the CTD sampling. In the following analysis, therefore, only the last week of current meter data were used (spanning from 12 to 20 May 1993). Figure 19 shows

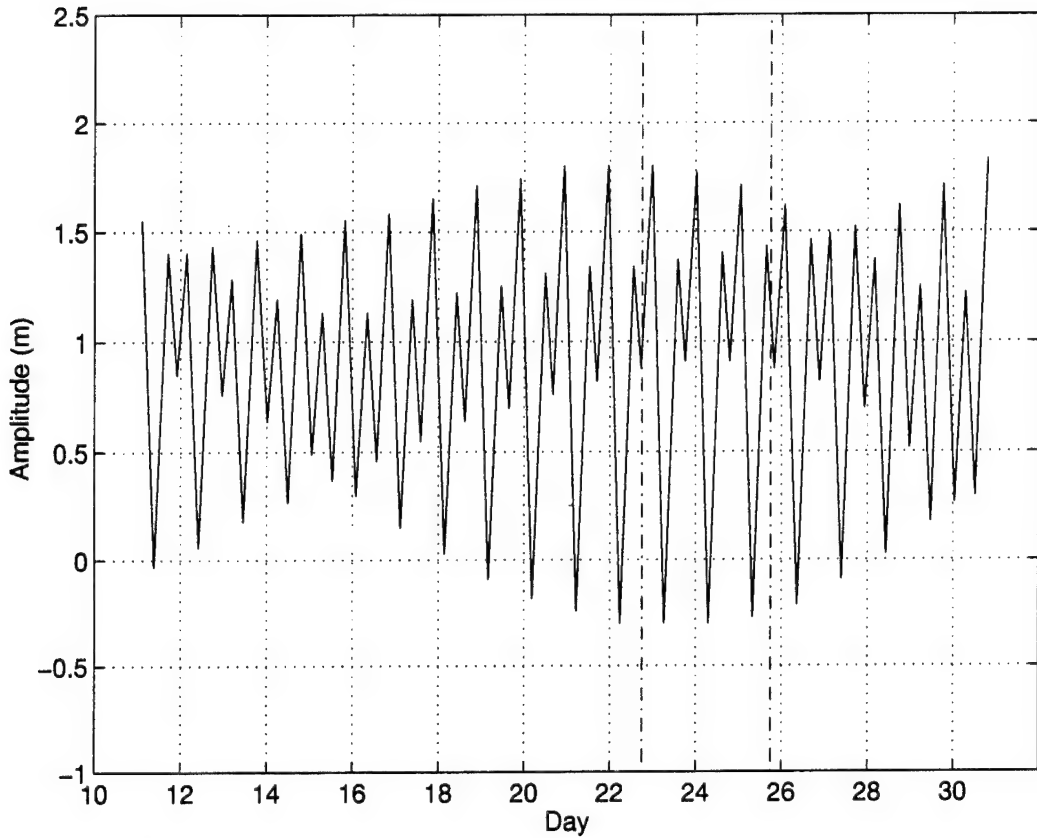


Figure 19. Predicted sea level at the San Francisco bay entrance, for May 1993, in meter. The dash-dot vertical lines mark the period of the CTD observations.

the sea level change as predicted from tide tables for the San Francisco Bay entrance for May 1993; it can be seen that the barotropic M_2 forcing is roughly the same during the CTD cruise period and the week before (the CTD period was coincident with a new moon phase, thus with small M_2 amplitudes).

A classical least-squares harmonic analysis was carried out on each of the 18 current meter time series to evaluate the spatial phase and amplitude distribution of the most important tidal constituents; by doing this at all levels and comparing the phase and amplitude differences, an idea of the modal distribution can be obtained. The harmonic analysis takes the time series and fits amplitude and phase to sinusoidal basis functions with known frequencies. With these short time series, only a few components are resolved. Longer time series are not advised because of the relatively short temporal scale of the

internal tides. In most of the cases (11 out of 18 current meters) the largest amplitude was associated with the M_2 . In the remaining cases, the largest amplitude was either located at wave-wave components, or at frequencies that are not supported by internal waves, without any dominant component.

Figure 20 shows the upper 500 m of an alongshore vertical cross section of

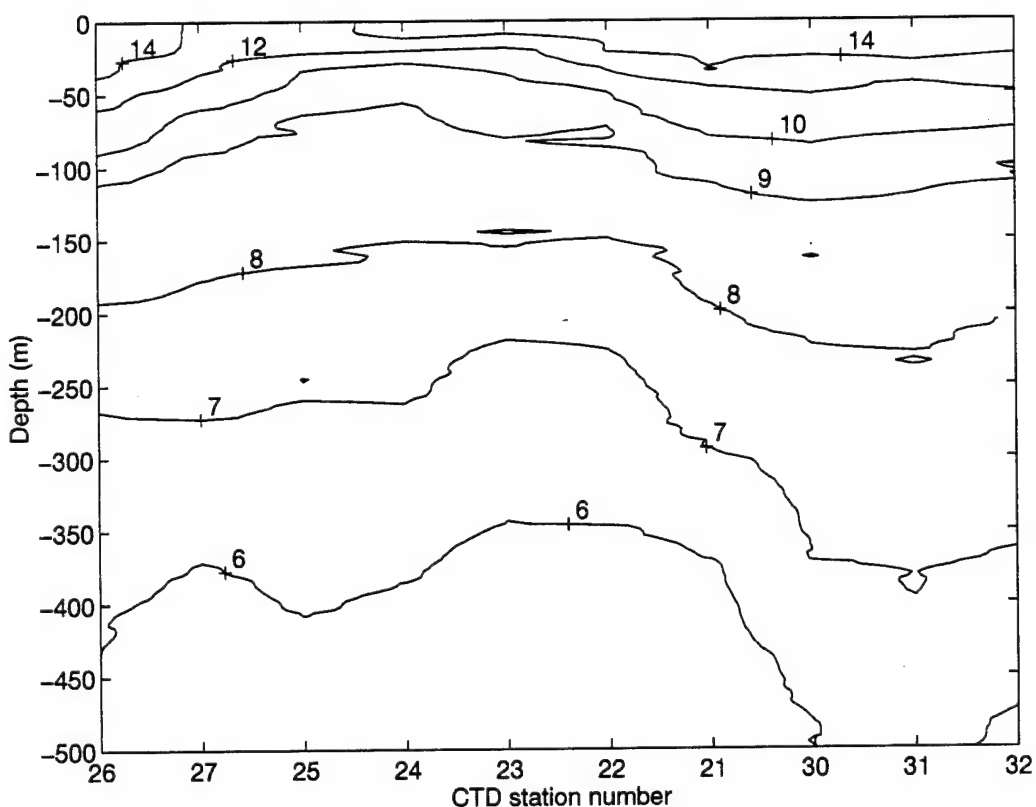


Figure 20. Alongshore vertical cross section of temperature ($^{\circ}\text{C}$) from raw CTD data. The horizontal axis is the station number in the section.

raw temperature data (not interpolated). In the vicinity of the eddy, the temperature differences observed between CTD stations are $O(10^{-1} \text{ }^{\circ}\text{C})$, being larger in the lower levels. The fitted amplitudes for the M_2 were in general one order of magnitude smaller.

The attempt to fit normal modes to the M_2 amplitudes was inconclusive due to the poor vertical resolution of the continuous records. The horizontal distribution of fitted phases appeared random, without any distinct pattern. The assumption of random, rapidly varying phase distribution of the baroclinic tides has already been used by

Noble *et al.* (1987) in their analysis of tidal currents. The results above seem to support this assumption in the present situation.

The cross-correlation between temperature and horizontal velocity time series at each instrument was also carried out to try to identify internal wave characteristics at the M_2 frequency, using cross-spectra techniques described by many data analysis references (e.g., Bendat and Piersol, 1993). According to Figure 21, the amplitude of the

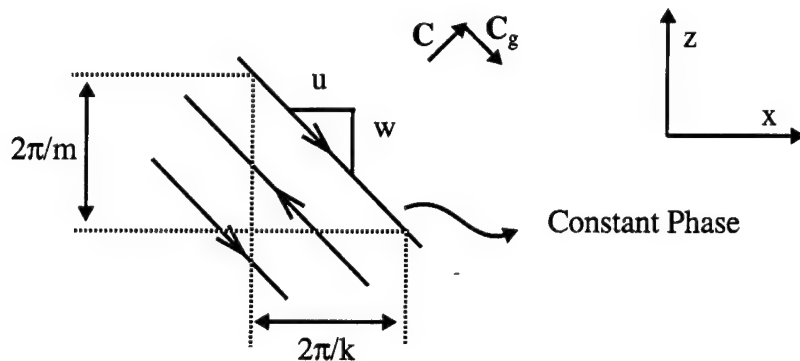


Figure 21. Relationship between the phase and group velocities and the velocity vector in a propagating internal wave (the y-axis is into the paper). \mathbf{C} is the phase velocity, \mathbf{C}_g is the group velocity, k and m are the wavenumbers (from Kundu, 1990).

temperature disturbance associated with internal waves is 90° out of phase with the u -component of velocity and in phase with the v -component. The results of the analysis of the coherence function and phase spectra for all the instruments are listed in Table 4. An

Station number (depth)	T vs. U		T vs. V	
	Coherence	Phase	Coherence	Phase
13 (100)	0.90	95	0.90	175
9 (100)	0.80	160	0.80	85
7 (100)	0.70	170	0.85	95
8 (100)	0.90	130	0.90	150
3 (150)	0.50	135	0.4	55
7 (150)	0.05	70	0.15	45

Table 4. Results of Currentmeter Cross-correlation Analysis for the M_2

Station number (depth)	<i>T</i> vs. <i>U</i>		<i>T</i> vs. <i>V</i>	
	Coherence	Phase	Coherence	Phase
13 (150)	0.65	45	0.65	130
9 (150)	0.85	180	0.75	110
8 (150)	0.20	85	0.05	160
13 (300)	0.55	35	0.90	90
9 (300)	0.05	90	0.10	120
3 (300)	0.90	150	0.70	100
7 (300)	0.35	0	0.40	45
8 (300)	0.60	135	0.60	170
13 (600)	0.25	90	0.20	150
7 (600)	0.75	170	0.90	85
8 (600)	0.90	120	0.60	120
8 (1800)	0.90	135	0.40	95

Table 4. Results of Currentmeter Cross-correlation Analysis for the M_2 (Continued)

inspection of the results shows that in only a couple of instruments are the temperature and velocities well correlated at the M_2 frequency, with phase values that match the requirements above (station 13 at 100 m and station 3 at 300 m, with an allowance made for phase uncertainty). A variety of situations occur for other instruments: relatively high values of coherence are associated with phase values that seem reversed (e.g., stations 9 and 7 at 100 m), or relatively high values of coherence are associated with meaningless phase values (e.g., station 13 at 150 m, station 8 at 600 m), or temperature and velocities are hardly or not correlated at all at this frequency (e.g., station 7 at 150 m, station 9 at 300 m). Moreover, the correlation and phase values are not consistent over an appreciable depth of the water column. These results show a complicated vertical and horizontal pattern of waves at the M_2 frequency whose influence in the sampling is very likely random.

The vertical correlation along the same water column was further investigated by computing the correlation and coherence functions between the temperature time series from the instruments in the same mooring. The values found at all the moorings were very small, even between instruments separated by only 50 m. The coherence values at the M_2 frequency were generally smaller than 0.5. The vertical

extension of the vertical motion patterns computed by the model and presented in section IV.A.1 cannot therefore be explained by an eventual aliasing of internal tides in the CTD data. Internal tides may be present, as suggested by the results of the harmonic and cross-correlation analyses, but the spatial distribution of phases and amplitudes seems random enough to cause small contributions to the field captured in the hydrographic data. The chances that these randomly varying fields would become coherent and influence the sampling in the worst possible manner seem very small.

Several factors may be contributing to this random distribution. The period of the CTD sampling was during a time of weak amplitudes in the barotropic semidiurnal frequency range, thus the forcing is minimal. Between 22 and 25 May there was a mix of relatively strong wind events and relaxations (Figure 3), causing the stratification to vary and affecting the maintenance of internal oscillations. Finally, the area where this study took place may be sufficiently close to the generation sites of the internal tides (composed of an infinity of source points along an irregular shelf or slope) for the internal wave field to be spatially incoherent and appear random. Further offshore the wave field would organize itself into a vertically and horizontally coherent set of modes of propagation, which could explain the measurements of M. Kosro away from the coast.

Some questions concerning the propagation of internal tides were raised by a study of well defined internal tide oscillations 700 km west of Santa Barbara, California (Levine and Richman, 1989). By performing an elliptical decomposition of the observed signals, they found that the predominant internal waves in that area over a period of a few days propagated in a direction *parallel* to the coast, contradicting the theories that predict propagation normal to the coast (Baines, 1986). They suggest that internal tides can be refracted by the density structure of the ocean and thus propagate in a variety of directions. Since the density structure in the eddy in the present study is fairly complex, these findings support the present assumption of small spatial coherence and highly random nature of the internal tide signal with a minimal influence on the observations.

b. Eddy rotation

This subsection is devoted to an analysis of the effect of eddy rotation on the solutions shown earlier. This is perhaps a more acute problem than the internal tides problem, because there is no way to quantify the effect of sampling a rotating body of water *while* the data is being collected. The analysis presented below assumes that *there is* a wavenumber in the eddy at least equal to two; it will be shown that a more reasonable

estimate is at least four, based solely on the time intervals between stations. The same reasoning is then applied to show that the DFI solution of a wavenumber five (Figure 7) is very reasonable. Translation of the eddy is neglected. According to Nof (1981), considering a well mixed core 300 m deep, the translation speed would be about 1.4×10^{-2} m/s westward, giving only 3 to 4 km of offshore displacement during the three days of CTD data collection.

The rotation of the eddy can be estimated by taking 40 cm/s as being representative of the tangential horizontal speed at 30 to 40 km from the center at the surface, and assuming a solid body rotation for simplification. Under these premisses the eddy takes about 6 days, or twice the period of the CTD sampling, to complete one rotation. The problem here is to determine how the sub-eddy scale features have been sampled during the half eddy rotation. Clearly, the features themselves will not propagate at the same speed of the almost circular mean flow, because there exists a potential vorticity gradient across the mean flow that acts like an equivalent *beta* effect for Rossby waves, thus retarding the propagation speed of the features relative to the mean flow.

A theoretical estimate of the phase speed of the sub-eddy meanders can be obtained by applying the results of baroclinic instability theory in the special case of a barotropic basic state (Holton, 1979, pp. 216), with the *beta* effect being replaced by its equivalent potential vorticity gradient, which amounts to the gradient of relative vorticity across the mean flow due to the flat bottom assumption. The phase speed of the disturbances is therefore estimated from:

$$C = U_m - \left(\frac{\partial \zeta}{\partial n} / k^2 \right) \quad (4.11)$$

where U_m is the mean speed of the layer, k is the azimuthal wavenumber, n is the radial coordinate in the natural coordinate system and ζ is the azimuthally averaged relative vorticity given by (in natural coordinates):

$$\zeta = \frac{V}{R} - \frac{\partial V}{\partial n} \quad (4.12)$$

R being the distance to the center of curvature and V the tangential speed. The effect of the second term on the right hand side of Equation 4.11 is expected to be small for high wavenumbers (phase speeds of about 90 to 95% of the mean azimuthal flow), in accordance with the results from the numerical experiments of McCalpin (1987).

The mean tangential velocities were computed as a function of distance to the center of the eddy, by taking azimuthal averages of horizontal speed at several radial distances from the center, and then averaging in the vertical over the first 500 m, i.e., over the mean vertical extent of the sub-eddy features. The results show mean tangential speeds of about 6 cm/s at 10 km from the center of the eddy, increasing to about 14 cm/s at 30 km and 17 cm/s at 35 km, and then decreasing to about 12 cm/s at 50 km from the center. Using these results in Equations 4.11 and 4.12, with some radial averaging over the radial scale of the disturbances, gives phase speeds for the sub-eddy features of about 14 cm/s at a distance of 30 km from the center of the eddy, that is, about 16 days to complete one rotation.

This estimate for the movement of the meanders agrees well with that observed during the model integrations; the animation of the horizontal velocity field at each time step showed an angular displacement of the sub-eddy features of about 10° about the center in 12 hours, or 18 days for a complete rotation.

Therefore, during the 3 days of CTD data collection, the meanders are estimated to have moved about 60° cyclonically. It is clear that a wavenumber two around the eddy cannot create the appearance of a wavenumber five seen in the results of section IV.A.1 by aliasing only, because the same trough (or ridge) could not be sampled three times during the cruise. Similarly, an analysis of Figure 18 shows that there is no time interval between CTD stations large enough to cause aliasing of wavenumbers smaller than the wavenumber five found in the DFI solution. Wavenumbers larger than five can theoretically be aliased, but this would imply that the length scale of the sub-eddy features would have to be smaller than the Rossby radius, which is the preferred length scale for the growth of baroclinic instabilities in a *f*-plane (Gill, 1982). Thus aliasing in the data due to meander propagation is not a cause for errors in the solution.

Comparing the time interval between CTD stations in Figure 18 with the streamline and vertical motion patterns in Figure 9, and using the new information on the propagation of these sub-eddy features, it is seen that the maximum time interval between adjacent stations is 34 hours (stations 20 and 21); these two stations are located at the edges of a sinking cell that lays upstream of a relatively broad region of upwelling. Hence, station 20 sampled the leading edge of the cyclonically rotating downwelling cell and station 21 sampled the trailing edge of the *same* cell, 34 hours later when the cell had already rotated about 30°. Therefore, the net effect of the asynoptic sampling in this instance is to decrease the apparent width of the downwelling cell. The same reasoning applies for stations 19 and

22 and others. In a global sense, this explains the decrease in the horizontal scale of the features sampled against the sense of rotation of the eddy, as exemplified, and the increase in the scales of the features sampled along the sense of rotation, such as the sequences of stations 28 to 21.

Other sequences of stations are not significantly affected by the propagation of the meanders because the time between stations was not long enough to cause an appreciable change in length scales; these include the sequence of stations 8, 7, 6, 11, 12 and 13 which, although sampled along the rotation, are apart by only about 13 hours total.

It then seems reasonable to conclude that the effect of the eddy rotation, or meander propagation, in the CTD data is to distort the horizontal scales of some of the features, namely those located on the southeast side of the eddy (right side in Figure 7). The features on the northwest side (left side in Figure 7) must have maintained their scales with minimum distortion because the time interval between stations is relatively short compared to the angular period of the meanders. Since the troughs and ridges associated with the sub-eddy scales are about 70° apart, it would require a sequence of stations with time intervals on the order of several days to cause aliasing of this wavenumber. Thus, although wavenumber five is deformed, it is an alias-free estimate of the measured field.

c. Interpolation parameters

The data analysis described in section II.B makes use of the MQ-B interpolation method to fill the model domain with the CTD and satellite data. This method makes use of several interpolation parameters, the most important of which are the interpolation constant c and the exaggeration applied to the vertical axis (see section II.B.1). In addition, it was also described in section II.B that the analysis procedure used for the temperature and salinity fields was not the same, because the number of data points for temperature and salinity are different.

At that point, the criterion for selecting the interpolation parameters was to achieve the best fit to the observed profiles (checked by plotting each observed profile against several interpolated fields) and to assure a minimum difference between extreme data values and extreme interpolated values. As noted, the application of these criteria along with the constraint in the number of observations resulted in the choice of different sets of parameters for temperature and salinity.

The process of determining the sensitivity of the circulation model/DFI results to the set of parameters chosen requires two steps: the interpolation of the data with

different parameters, yielding slightly different analyzed fields each time; and running the model with each of the newly analyzed fields to compare results. Several such runs were made. It was noticed that although the analyzed fields were very sensitive to the interpolation constant c , the dynamically balanced velocity fields maintained the same qualitative agreement in the location of the meanders and vertical motion areas; the differences were found in the magnitude of the dynamically balanced fields (either stronger or weaker velocities).

Another sensitivity test was made to estimate the influence of analyzing temperatures and salinities differently. In this case, the two-dimensional interpolation of the CTD data at each level (see section II.B.2.a) was also performed for the salinities, and the result was then three-dimensionally interpolated into the model domain using the same parameters as for the temperature interpolation. The result was a salinity field that looked better but had worse fits with the observed profiles and maxima and minima. The model DFI solution showed a weaker field of vertical motion, but in good qualitative agreement with the original results.

These considerations demonstrate the more or less dependence of the results on the MQ-B method because of the limited data available. The choice of the parameters utilized in this study was dictated by criteria that guaranteed (after a long process of trial and error) the closest possible match between observed and analyzed fields in the regions where data was available. Since the computed velocities and the observed currents from the moorings agree much better for the fields analyzed as described in II.B than they do for the other analysis made for sensitivity purposes (again with a limited set of data for comparison), it is felt that the analyzed fields from II.B and the associated results are correct within the given constraints.

B. QUASIGEOSTROPHIC OMEGA EQUATION RESULTS

The vertical motion in the study area was also diagnosed by solving the \mathbf{Q} -vector form of the QG omega equation, reproduced below for convenience:

$$(N^2 \nabla^2 + f_0^2 \frac{\partial^2}{\partial z^2}) w = 2 \nabla \cdot \mathbf{Q}, \quad (4.13)$$

where

$$\mathbf{Q} = \frac{g}{\rho_0} \begin{bmatrix} \frac{\partial \mathbf{V}_g}{\partial x} \cdot \nabla \rho \\ \frac{\partial \mathbf{V}_g}{\partial y} \cdot \nabla \rho \end{bmatrix}, \quad (4.14)$$

with zero boundary conditions, as described in section III.B.

The right hand side of Equation 4.13 (known as the *forcing*) was computed from the analyzed density field, and also from the dynamically balanced density field, for comparison purposes. The resulting \mathbf{Q} -vector divergence fields were smoothed with one pass of a smoother-desmoothen filter (Kreitzberg and Perkey, 1977; Schuman, 1957), as is common practice in similar applications (e.g., Pauley and Nieman, 1992). An example of the \mathbf{Q} -vector field in a small region of the domain at 100 m depth, obtained from the analyzed density field, is shown in Figure 22. The figure shows the spatially averaged \mathbf{Q} -vectors, dynamic height and density fields in the area of the meander located closest to the offshore boundary (lower part of Figure 9; this figure can be used for exact location of the area depicted in Figure 22). Although a complete analysis of the dynamics of this meander would require information on the same fields above and below the selected depth, Figure 22 provides enough information to assess the behavior of the forcing of the QG omega equation in this area. A trough in the dynamic height field extends southward and offshore (roughly from the point (15,14) to the point (21,7)). The geostrophic advections take place parallel to the dynamic height contours. Thus upstream of the trough axis there is a region of relatively weak cold water advection from the center of the eddy and negative vorticity advection from the upstream ridge, whereas downstream of the trough there is a region of stronger warm water advection from outside of the eddy and positive vorticity advection from the trough. Cold and warm advection by the geostrophic currents are related to downward and upward motions, respectively (second term on the right hand side of Equation 3.19). Since the currents, and associated advections, generally increase toward the surface (the first term on the right hand side of Equation 3.19), upwelling downstream and downwelling upstream of the trough should be expected. Positive and negative vorticity advection are responsible for the propagation of the meander (in the absence of divergence), and their vertical structure also contributes to the vertical motion.

The expected patterns of upwelling and downwelling cells downstream and upstream of the trough, respectively, are well represented by the \mathbf{Q} -vectors, which generally point toward regions of rising motion. On the left of the trough the vectors are in

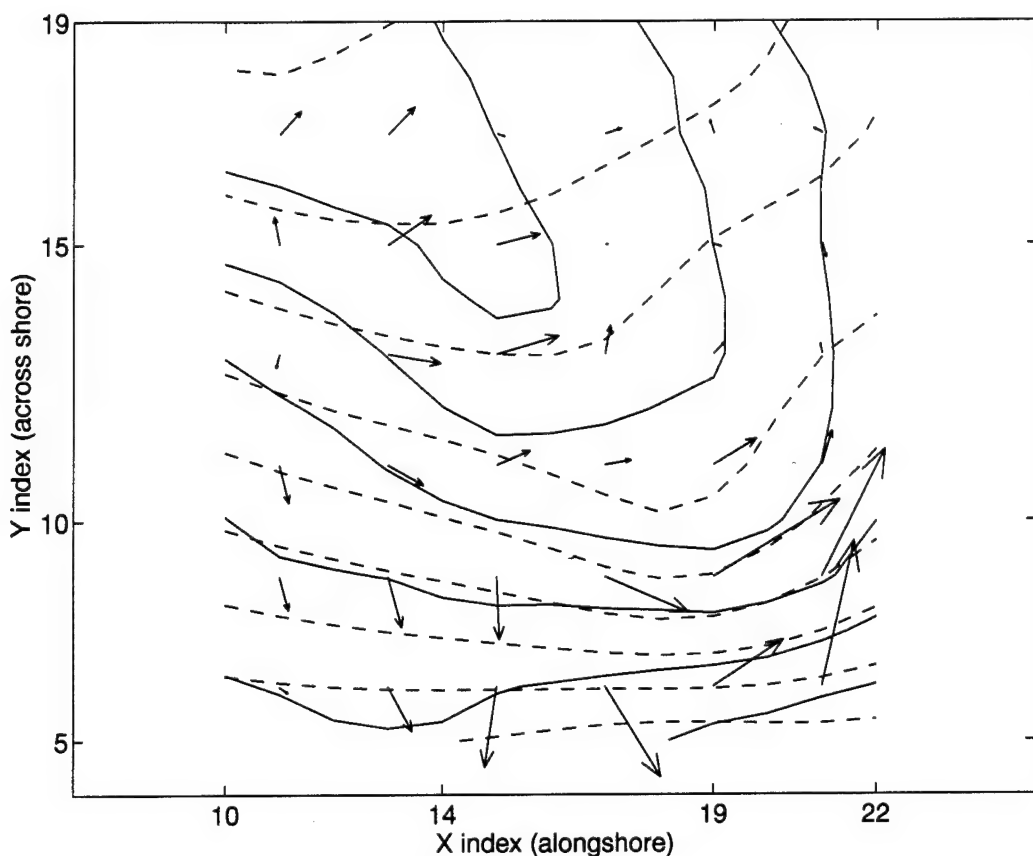


Figure 22. Field of \mathbf{Q} -vectors computed from the analyzed density field in part of the domain, at 100 m. Also shown are dynamic height (solid) and density (dashed) contours. The X and Y coordinates are the same as in Figures 9 and 23.

general oriented away (diverge) from the region of cold water advection, where the dynamic height and density contours intercept at a greater angle, thus denoting the area of sinking motion upstream of the trough. Downstream of the trough, the \mathbf{Q} -vectors are oriented with maximum convergence near the area where there is a local maximum in warm water advection (dynamic height and density contours intercepting almost at right angles) and consequent upwelling. Thus, although the effects of differential vorticity advection have not been considered, such an analysis is consistent with a similar analysis based only on the changes of relative vorticity following the motion of a parcel through the meanders (section IV.A.1).

The solution for w on the left hand side of Equation 4.13 (known as the *response*) was computed with a simultaneous over-relaxation method (Haltiner and Williams, 1980).

Figure 23 shows the field of vertical motion at 100 m depth, obtained using the analyzed density field. A very good qualitative agreement with the DFI solution depicted in Figure 9 is apparent. The two solutions reproduce the same pattern of radially aligned patches of sinking and rising motion, with remarkable precision as to the location of the vertical motions and their relative magnitudes. The patterns of rising and sinking motion deduced above from the \mathbf{Q} -vectors, dynamic height and density fields (Figure 22) near the meander in the lower part of Figure 23 are clearly represented and in agreement with the forcing.

Quantitatively, the vertical velocity solutions in Figures 9 and 23 are somewhat different. The maximum QG vertical motion is about 30% larger than the DFI solution in both rising and sinking areas. This difference can be due to two causes: the DFI procedure is appreciably affecting the initial density field, causing the resulting DFI vertical velocity field to be considerably different than that diagnosed from the initial density field, or/and the difference is due to the QG assumptions. The relative importance of the former can be estimated by comparing the QG omega equation results obtained from the analyzed and from the dynamically adjusted density fields. Figure 24 shows the latter results, which should be compared to those in Figure 23. It is seen that the two QG solutions are not significantly different, that is, the QG vertical motions diagnosed from the analyzed and from the DFI density fields are almost the same. This result is explained by the discussion of the geostrophic adjustment in section IV.A.2, where it was shown that the scales being initialized in the model are comparable to, or larger than, the Rossby radius. Therefore, the density field is hardly affected by the DFI, so the QG solutions should not be very different. Thus, the difference between the two solutions for w (PE and QG) is entirely due to the QG assumptions.

The effects of the QG assumptions in the QG solution for w can be assessed from the so-called *generalized* omega equation, which contains the higher order effects that have been neglected in the QG form, namely relative vorticity, tilting, stability, ageostrophic advection and vertical advection effects (still considering adiabatic solutions). Comparisons between the generalized and the QG omega equation have been made by Pauley and Nieman (1992). They found that the QG omega equation solution is generally too large in: 1) regions of strong stability; 2) regions of large relative vorticity; 3) regions of sinking motion in cyclonic curvatures (rising motion in cyclonic flows can either be under- or overestimated). A complete analysis of the generalized omega equation is beyond the scope of this work, but some of the ageostrophic effects can be readily identified.

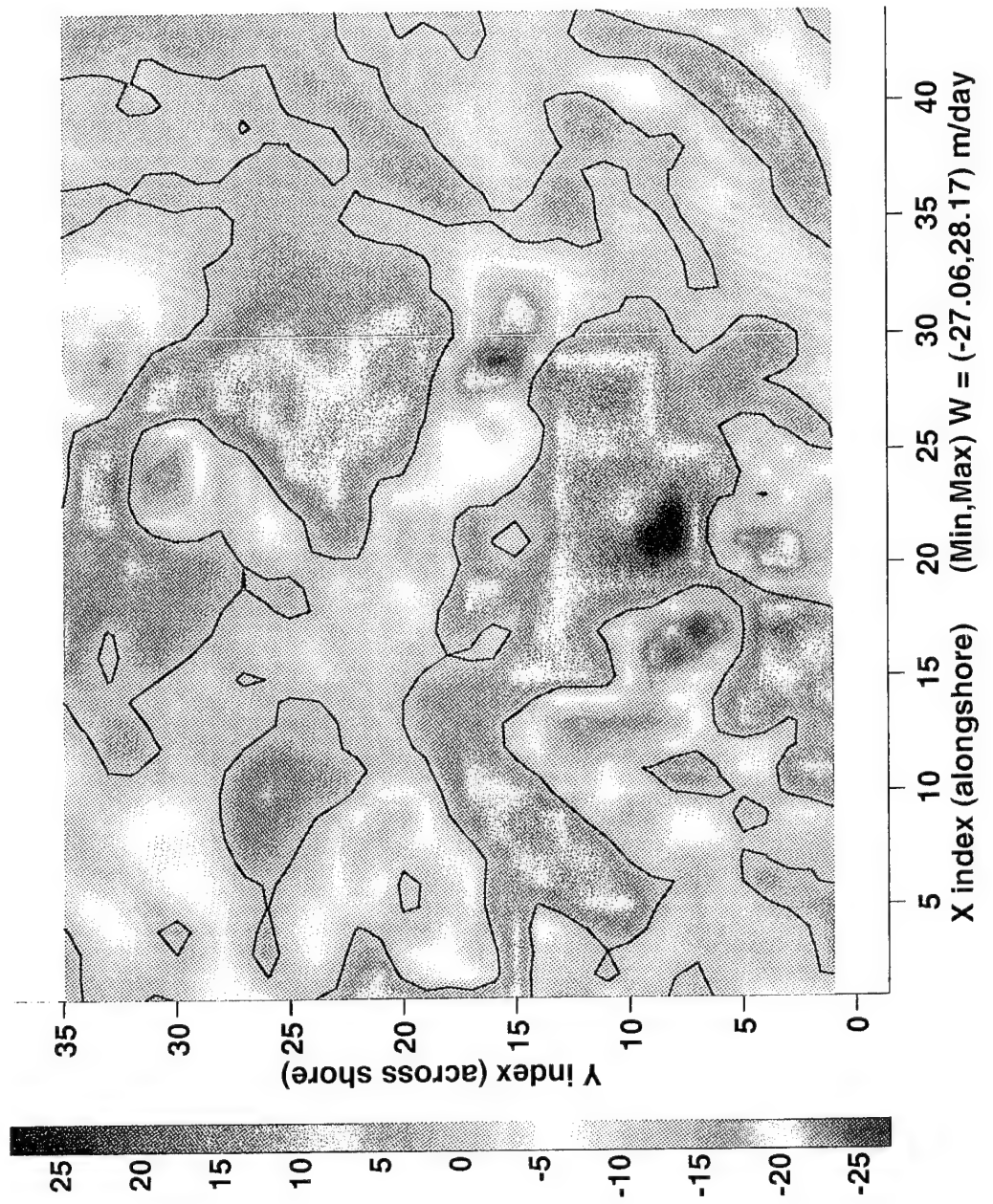


Figure 23. Horizontal cross section of the quasigeostrophic vertical velocity field at 100 m depth, in m/day, from the solution of the omega equation with the analyzed density field. The orientation and horizontal scales are the same as in Figure 9. Note that the velocity scale is different from Figure 9.

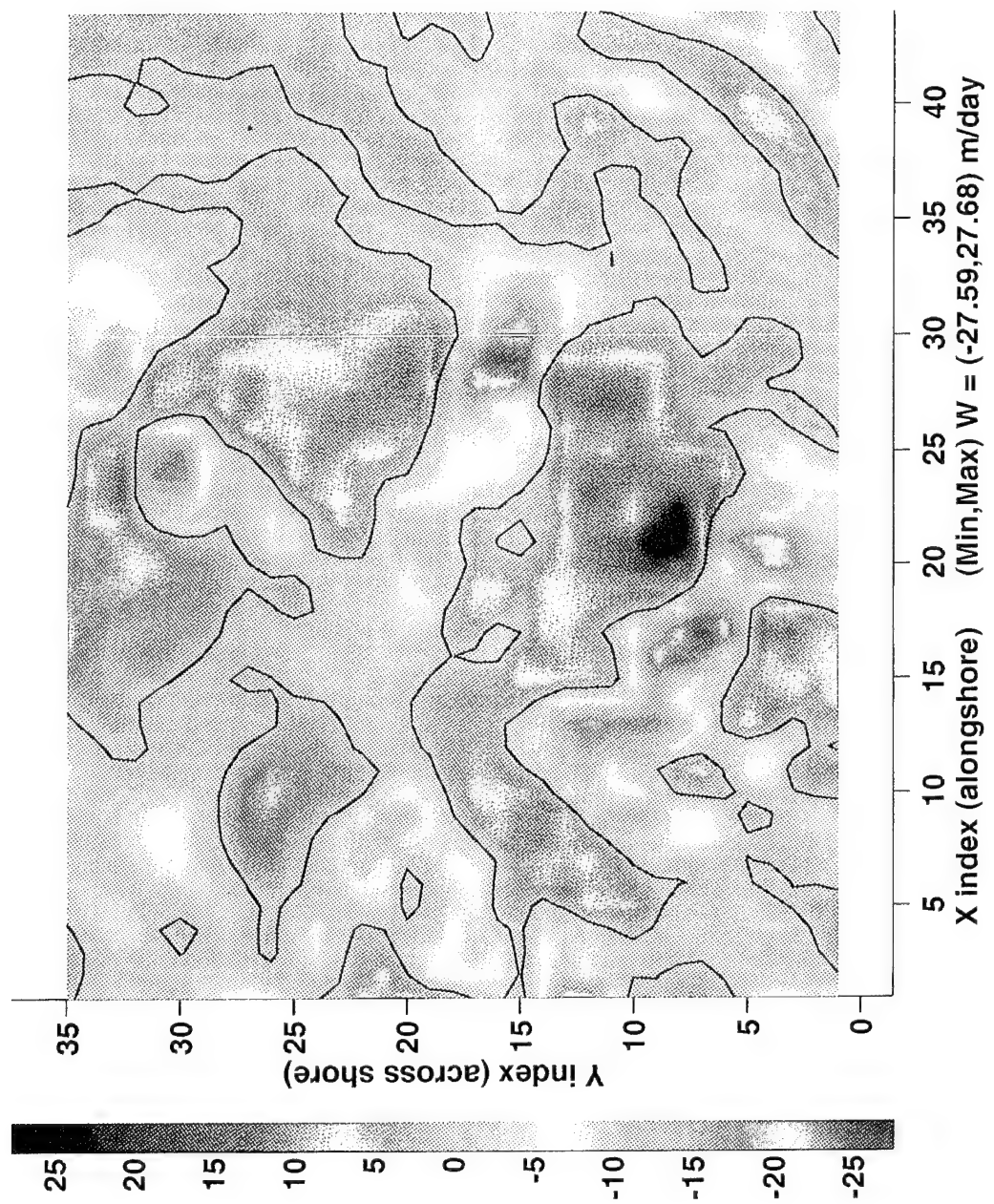


Figure 24. Same as Figure 23, but obtained from the dynamically balanced (DFI) density field.

The stability profile used in the QG solution in Figure 23 is a spatial average of all the CTD casts. The maximum stability is found around 30–40 m and below that, it decreases sharply. The eddy has a well mixed core down to 300 m, thus stability must be relatively weak in the eddy at 100 m depth.

The mean relative vorticity of the eddy is about $0.1 f$. Thus neglecting relative vorticity versus planetary vorticity in the divergence term of the vorticity equation is by itself introducing a 10% error in the response of the QG omega equation. This effect tends to be asymmetric, causing the QG solution in general to overestimate w in regions of positive relative vorticity and to underestimate w in regions of negative relative vorticity. This effect is undoubtedly contributing to some of the overestimation of w by the QG solution in the meander trough shown in Figure 22.

The QG solution for the vertical motion presented in Figure 23 seems to be strong in both rising and sinking motions. Thus the *ageostrophic* advection of vorticity and density that otherwise would be opposing the geostrophic advectons in a cyclonic flow are missing in the whole domain, and not only in the areas of sinking motion. Figure 25 shows the ageostrophic velocity field \mathbf{V}_{ag} , computed from:

$$\mathbf{V}_{ag} = \mathbf{V}_{DFI} - \mathbf{V}_g \quad (4.15)$$

where \mathbf{V}_{DFI} is the horizontal velocity vector resulting from the DFI procedure, and \mathbf{V}_g is the initial geostrophic velocity, as well as the density and dynamic height fields for the same region and depth as in Figure 22. The larger vectors shown in Figure 25 represent ageostrophic velocities that are only about 10% of the geostrophic velocities in the same area. It is seen that upstream of the trough, the ageostrophic velocity vectors generally oppose the geostrophic flow and are associated with (weak) warm water advection and positive geostrophic vorticity advection, both inducing rising motion. This region is where a maximum of sinking motion in the QG solution is related to the cold water geostrophic advection. Thus, neglecting ageostrophic advection of density and geostrophic vorticity, which is an order of the Rossby number effect, causes the sinking motion to be overestimated upstream of the trough by a factor of about 10%.

The geostrophic advection of *ageostrophic* vorticity upstream of the trough, which is also an order of the Rossby number effect, can be estimated by a careful inspection of Figure 25. It can be seen that the ageostrophic vectors tend to curl positively in two main regions, one further upstream of the trough and another just downstream of the trough. Between these two regions the ageostrophic vorticity is generally negative. Thus, the

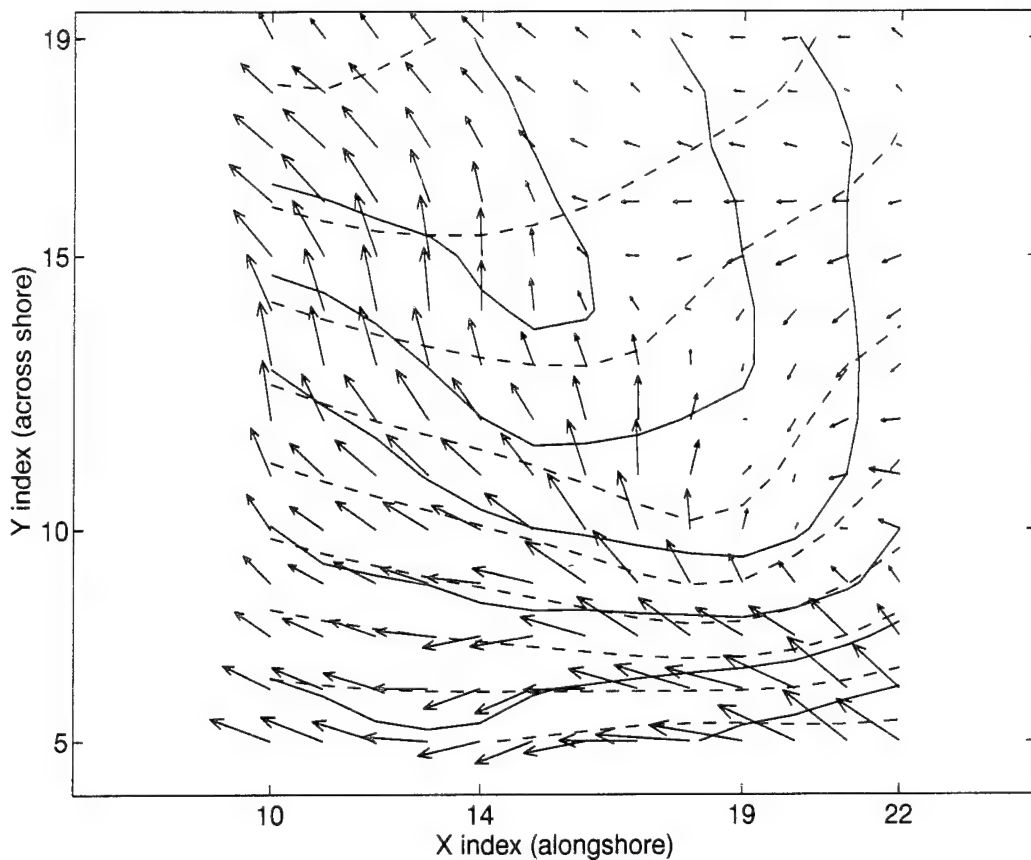


Figure 25. Field of ageostrophic velocity vectors at 100 m depth, for the same part of the domain as in Figure 22. Also shown are dynamic height (solid) and density (dashed) contours.

geostrophic advection of ageostrophic vorticity is positive upstream of the trough. Therefore, neglecting this term in the QG solution also causes an overestimate of sinking motion upstream of the trough by about 10%.

Downstream of the trough, the ageostrophic velocity vectors are smaller and the effect of the ageostrophic advection is not as evident as it is upstream of the trough. In a region immediately downstream of the trough axis, the ageostrophic advection is weakly opposing the geostrophic warm water advection and would therefore attenuate the QG estimate for rising motion there. Moreover, the geostrophic flow is advecting negative ageostrophic vorticity into the same area, with a similar contribution for the attenuation of the QG rising motion estimate. Including the neglect of relative vorticity in the QG

divergence term, these effects all indicate an overestimate of the rising motion in and immediately downstream of the trough in the QG solution. Further downstream the weak ageostrophic advections would probably slightly enhance the rising motion computed from the QG omega equation, and other effects that are also order of the Rossby number (Pauley and Nieman, 1992) may be playing a role. This mixed effect is in accordance with the results of Pauley and Nieman (1992) for regions of rising motion in cyclonic curvatures.

Another reason that could account for some of the differences between the two solutions is the high order numeric computations involved in the determination of the forcing of Equation 4.13, which makes the divergence of the \mathbf{Q} -vectors numerically sensitive to small disturbances in the density and geostrophic velocity fields.

Although the analysis above was focused on a region that shows the maximum discrepancy between PE and QG results, it can be generalized to the other meanders as well. It then seems reasonable to conclude that, in the absence of other effects, it is a combination of eliminating the relative vorticity from the divergence term in the vorticity equation, and neglecting the ageostrophic advection and vorticity, that is contributing the most to the quantitative differences between the QG and the DFI estimates of vertical velocity, with the QG values being overestimated.

The vertical structure of the QG vertical velocity solution is shown in Figures 26 and 27. These figures should be compared to the DFI solution in Figures 11 and 12, respectively. Again, a very good qualitative agreement is found between the two solutions, with the QG solution presenting larger values for maximum and minimum velocities, but with some good agreement in other areas. The vertical extent and correlation of the sinking and rising cells of vertical motion are also captured by the QG solution, but there is some variability in the deeper levels that is not found in the DFI solution. The area close to the northeastern boundary (right side in Figure 27) where the CTD profiles were extended in depth below the shallow topography also shows some unrealistic values of vertical motion.

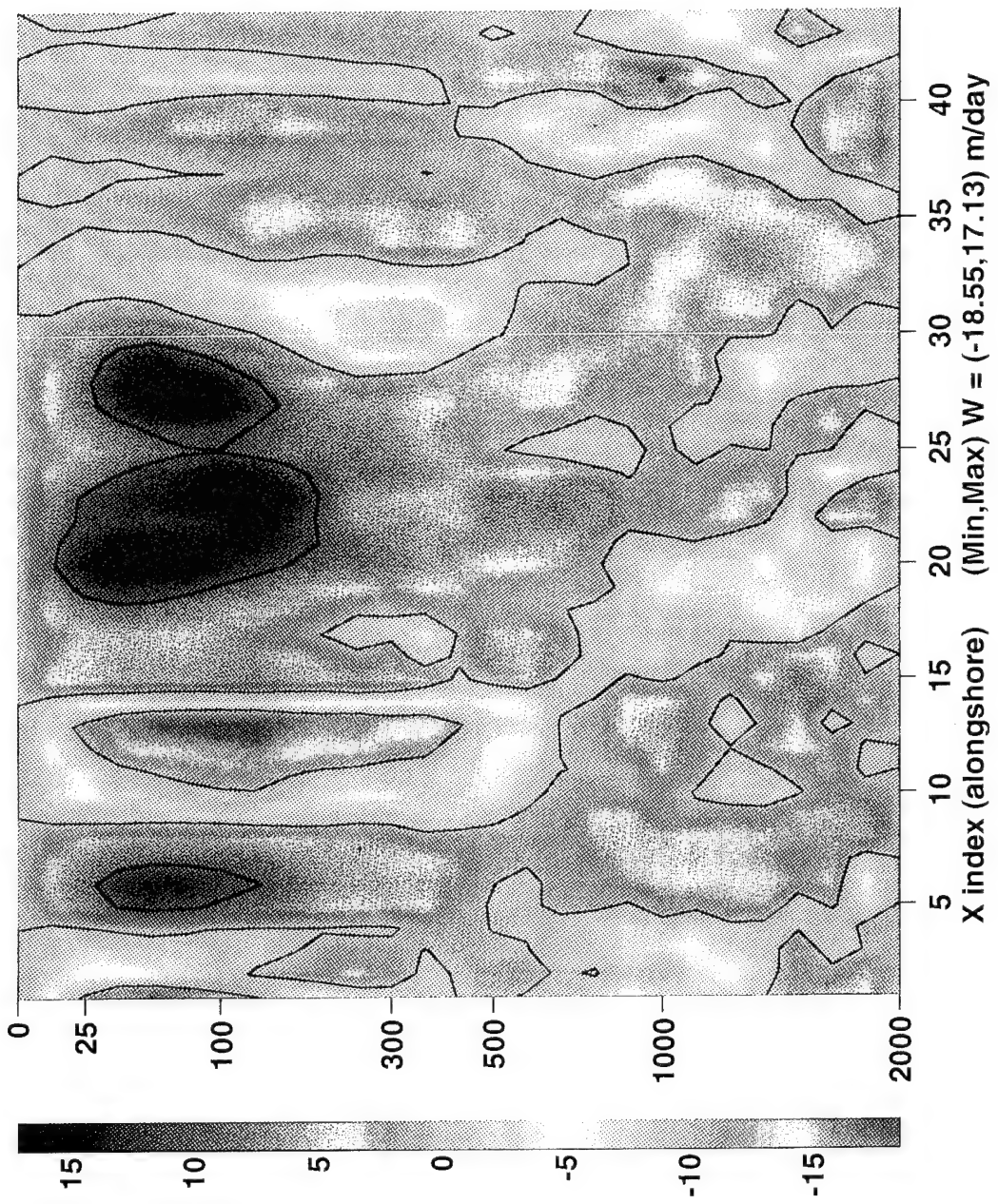


Figure 26. Vertical cross section of the quasigeostrophic vertical velocity field in the alongshore direction, in m/day, with depths in meters. The section shown is the same as in Figure 11 (the velocity scales are different). Note that the vertical axis is not linear.

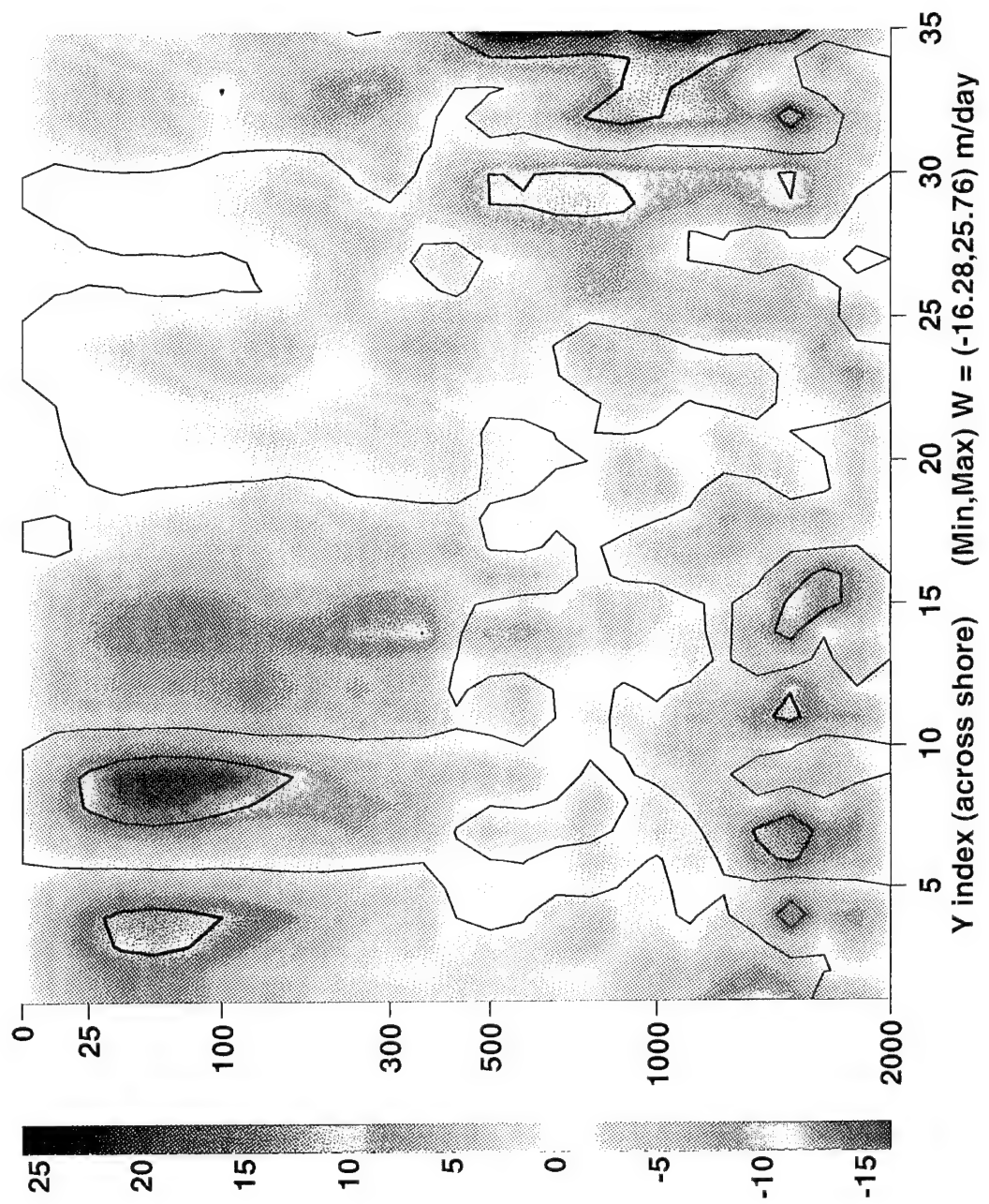


Figure 27. Vertical cross section of the quasigeostrophic vertical velocity field in the across shore direction, in m/day, with depths in meters. The section shown is the same as in Figure 12 (the velocity scales are different). Note that the vertical axis is not linear.

V. CONCLUSIONS

The main objective of this study was to achieve, for the first time, a quantitative description of the three-dimensional circulation in a coastal eddy, including the vertical velocity. The temperature and salinity data collected during one of the EBC cruises was thus first analyzed using multiquadric-biharmonic interpolation. The resulting density field was then used in a primitive equation model, to obtain three-dimensional fields of dynamically balanced currents and densities through a digital filter initialization (DFI) technique. The DFI is equivalent to a nonlinear normal mode initialization, and thus the dynamically balanced fields resulting from the model integrations under DFI are representative of the slow mode at the time of the observations.

The results from this procedure reveal a cyclonic eddy circulation (relative vorticity in the order of $0.1\text{--}0.15f$) about 90–100 km in diameter, with a total of five meanders each having a mean horizontal length scale of about 25 km, present in the flow. The maximum horizontal velocities in the eddy are about 40–50 cm/s at the surface, in good agreement with the currents observed by current meters moored in the area, and with the hull mounted ADCP currents estimates.

The meanders are associated with regions of rising and sinking motion, which are shown to be consistent with potential vorticity considerations applied to a water parcel following the motion, i.e., downwelling upstream and upwelling downstream of the troughs. These patterns of vertical motion appear to be radially aligned, distributed on either side of each trough axis, and extending coherently in the vertical for about 500 m or more. The maximum magnitudes of the vertical velocity (either rising or sinking) occur between 50 and 150 m depth, and are about 20–22 m/day.

The vertical distribution of the vertical velocity amplitudes is fairly well described by the first dynamical mode, which has a characteristic Rossby radius of 23 km. This was the basis for a discussion on the process of geostrophic adjustment and on the choice of an appropriate initial current field. It was shown that the scales determining the main patterns of vertical motion are comparable to the Rossby radius, and thus it is the observed (analyzed) density field that determines the final state of the currents at these scales. The initial velocity field was therefore assumed to be geostrophic while the depth averaged flow was computed assuming a level of known motion (2 cm/s alongshore to the northwest at

2000 m depth) based on current meter data. The exact magnitude of this bottom velocity was found not to be significant in determining the final dynamically balanced solution.

At this stage the eddy presents a closed circulation within 30 to 35 km from the center, with nearly zero average vertical velocities within this area at all levels. This means that the eddy is no longer acquiring relative vorticity by advection from other sources, and consequently it is no longer spinning up, and thus it is about to detach from the origin region near the coast and to drift westward (or southwestward, if the effect of the California Current farther offshore is taken into account). However, the effects of the poleward undercurrent close to the shore could not be resolved in this study because of the way the data were processed in the northeastern part of the domain. Therefore, allowance must be made for possible vorticity exchanges in the regions of the eddy that are more than 35 km away from the center.

Some aspects related to the lack of exact synopticity in the hydrographic data were also examined. The influence of the internal tides on the sampling is thought to be minimal, since a classical harmonic analysis and a cross-correlation analysis of the current meter time series indicate that the spatial phase distribution of the internal tides was sufficiently random. The influence of the eddy rotation, or meander propagation, during the period covered by the CTD sampling was also analyzed. It was shown that a wavenumber five disturbance in the mean flow around the eddy could not have been aliased during sampling, based on the sampling pattern and on the time intervals between the hydrographic stations.

The vertical motion was also diagnosed from the analyzed density field within the framework of quasigeostrophic (QG) dynamics by solving the **Q**-vector form of the QG omega equation. The results thus obtained are in close agreement with the PE/DFI results. The same patterns of rising and sinking motion were again found and explained using QG dynamics. The maximum discrepancy between the DFI and the QG vertical motion is a magnitude difference of about 30%, with the QG method presenting the larger values. A clear explanation for this was given, based on the terms neglected in the QG omega equation (the two most important in this study are thought to be the ageostrophic advections, and neglecting relative vorticity in the divergence term) and illustrated using an example of the actual ageostrophic velocity field in the vicinity of one of the meanders.

From all of the results summarized above, it is concluded that a robust description of the circulation in the observed cyclonic eddy, including the vertical motion, has been achieved, complementing significantly the wealth of information that has become available with recent observational programs in the Californian and Oregonian coasts. The detailed

circulation in eddies such as the one studied here, i.e., with the same temporal and horizontal scales, and at the same stage in their life span, can be inferred from the results above. The methodology used in this work can also be applied to other areas of the world ocean where appropriate quasiosynoptic data sets are available.

Future work should be directed at the inclusion of bottom topography in the PE model domain. The PE results in the region of the domain closer to shore are not reliable because the flat bottom assumption forced some of the profiles to be extended to the uniform depth of 2000 m using a similarity method. The effect of a varying bottom in the vorticity budget will surely yield a more complete understanding of the dynamics of the eddy, and eliminate the undesirable effect of the extended profiles.

Other points that can be investigated deal with the optimization of the DFI procedure, namely the optimization of the lowpass filter and of the filtering process, since it was shown that filters with fewer coefficients can better meet the constraints of the spin-up phase.

Another aspect that is worth investigation is to predict the future motion of the eddy. Once the fields have been dynamically balanced by the DFI, then the PE model can be used to integrate forward and simulate the evolution of the eddy. A potential problem in this particular data set is the absence of information on the temporal evolution of the boundaries. If the boundary conditions are chosen to remain constant at inflows (as they were during the short initialization runs), then the eddy will not be able to drift westward and the general result will perhaps be an elongated eddy that remains attached to the boundaries where inflow takes place. Thus a careful treatment of the boundaries would be necessary.

LIST OF REFERENCES

- Acoustic Doppler Current Profilers, *Principles of Operation: A Practical Primer*, RD Instruments, 1989.
- Adamec, D., Elsberry, R., Garwood, R. W. and Haney, R. L., "An Embedded Mixed-Layer-Ocean Circulation Model", *Dynamics of Atmospheres and Oceans*, V. 6, pp. 69-96, 1981.
- Andrews, J. C. and Scully-Power, P., "The Structure of an East Australian Current Anticyclonic Eddy", *Journal of Physical Oceanography*, V. 6, No. 5, pp. 756-765, September 1976.
- Arhan, M. and Colin de Verdière, A., "Dynamics of Eddy Motions in the Eastern North Atlantic", *Journal of Physical Oceanography*, V. 15, pp. 153-170, February 1985.
- Baines, P.G., "Internal Tides, Internal Waves and Near-Inertial Motions", in Baroclinic Processes on Continental Shelves, *Coastal and Estuarine Sciences*, AGU, Vol. 3, 1986.
- Batteen, M. L., Rutherford, M. J. and Bayler, E. J., "A Numerical Study of Wind- and Thermal-Forcing Effects on the Ocean Circulation off Western Australia", *Journal of Physical Oceanography*, V. 22, No. 12, pp. 1406-1433, December 1992.
- Bendat, J. S., and Piersol, A. G., *Engineering Applications of Correlation and Spectral Analysis*, John Wiley & Sons, Inc., 458 pp., 1993.
- Bower, A. S., "Potential Vorticity Balances and Horizontal Divergence along Particle Trajectories in Gulf Stream Meanders East of Cape Hatteras", *Journal of Physical Oceanography*, V. 19, pp. 1669-1681, November 1989.
- Bower, A. S., and Rossby, T., "Evidence of Cross-Frontal Exchange Processes in the Gulf Stream Based on Isopycnal RAFOS Float Data", *Journal of Physical Oceanography*, V. 19, pp. 1177-1190, September 1989.
- Bowman, M. J., "On the β -Induced Coastal Trapping of a Baroclinic Eddy", *Journal of Physical Oceanography*, V. 15, pp. 817-822, June 1985.
- Carlson, T. N., *Mid-Latitude Weather Systems*, HarperCollins Academic, 507 pp., 1991.

- Chiswell, Stephen M., "Vertical Structure of the Baroclinic Tides in the Central North Pacific Subtropical Gyre", *Journal of Physical Oceanography*, V. 24, No. 9, pp. 2032–2039, September 1994.
- Chumbinho, R., "Objective Analysis of a Coastal Ocean Eddy Using Satellite AVHRR and In Situ Hydrographic Data", MS Thesis, Naval Postgraduate School, September 1993.
- Crochiere, R. E. and Rabiner, L. R., *Multirate Digital Signal Processing*, Prentice-Hall, 411 pp., 1983.
- Fiekas, V., Leach, H., Mirbach, K.-J. and Woods, J. D., "Mesoscale Instability and Upwelling. Part 1: Observations at the North Atlantic Intergyre Front", *Journal of Physical Oceanography*, V. 24, pp. 1750-1758, August 1994.
- Geyer, W. R., and Signell, R., "Measurements of Tidal Flow Around a Headland With a Shipboard Acoustic Doppler Current Profiler", *Journal of Geophysical Research*, Vol. 95, No. C3, pp. 3189–3197, March 1990.
- Gill, Adrian. E., *Atmosphere-Ocean Dynamics*, Academic Press, Inc., 662 pp., 1982.
- Haidvogel, D. B., Beckmann, A., and Hedström, K. S., "Dynamical Simulations of Filament Formation and Evolution in the Coastal Transition Zone", *Journal of Geophysical Research*, Vol. 96, No. C8, pp. 15017–15040, August 1991.
- Haltiner, G. J., and Williams, R. T., *Numerical Prediction and Dynamic Meteorology*, John Wiley & Sons, Inc., 477 pp., 1980.
- Haney, R. L., "A Numerical Study of the Response of an Idealized Ocean to Large-Scale Surface Heat and Momentum Flux", *Journal of Physical Oceanography*, V. 4, pp. 145-167, April 1974.
- Haney, R. L., "On the Pressure Gradient Force over Steep Topography in Sigma Coordinate Ocean Models", *Journal of Physical Oceanography*, V. 21, No. 4, pp. 610-619, April 1991.
- Haney, R. L., Hale, R. A., and Collins, C. A., "Estimating Subpycnocline Density Fluctuations in the California Current Region From Upper Ocean Observations", *Journal of Atmospheric and Oceanic Technology*, in press, 1995.
- Hardy, R. L., "Multiquadric Equations for Topography and Other Irregular Surfaces", *Journal of Geophysical Research*, V. 76, pp. 1905-1915, 1971.
- Hardy, R. L., "Theory and Applications of the Multiquadric-Biharmonic Method", *Computers Math. Applic.*, V. 19, No. 8/9, pp. 163-208, 1990.

- Henrick, R. F., Jacobson, M. J., Siegmann, W. L. and Clark, J. G., "Use of Analytical Modeling and Limited Data for Prediction of Mesoscale Eddy Properties", *Journal of Physical Oceanography*, V. 9, No. 1, pp. 65-78, January 1979.
- Hickey, B. M., "The California Current System - Hypothesis and Facts", *Progress in Oceanography*, Pergamon Press, V. 8, pp. 191-279, 1979.
- Holton, J. R., *An Introduction to Dynamical Meteorology*, Academic Press, Inc., 391 pp., 1979.
- Hoskins, B. J., Draghici, I. and Davies, H. C., "A New Look at the Omega-Equation", *Quart. J. Roy. Met. Soc.*, No. 104, pp 31-38, 1978.
- Huang, X.-Y. and Lynch, P., "Diabatic Digital-Filtering Initialization: Application to the HIRLAM Model", *Monthly Weather Review*, V. 121, No. 2, pp. 589-603, February 1993.
- Huyer, A., "Coastal Upwelling in the California Current System", *Progress in Oceanography*, Pergamon Press, V. 12, pp. 259-284, 1983.
- Huyer, A., "Hydrographic Observations along the CODE Central Line off Northern California", *Journal of Physical Oceanography*, V. 14, No. 10, pp. 1647-1658, October 1984.
- Ikeda, M. and Emery, W. J., "Satellite Observations and Modeling of Meanders in the California Current System off Oregon and Northern California", *Journal of Physical Oceanography*, V. 14, No. 9, pp. 1434-1450, September 1984.
- Kundu, Pijush K., *Fluid Mechanics*, Academic Press, Inc., 638 pp., 1990.
- Kreitzberg, C. W., and Perkey, D. J., "Release of Potential Instability. Part II: The Mechanism of Convective/Mesoscale Interaction", *Journal of Atmospheric Sciences*, V. 34, pp. 1569-1595, 1977.
- Leach, H., "The Diagnosis of Synoptic-Scale Vertical Motion in the Seasonal Thermocline", *Deep-Sea Research*, V. 34, No. 12, pp. 2005-2017, 1987.
- Le Group Tourbillon, "The Tourbillon Experiment: A Study of a Mesoscale Eddy in the Eastern North Atlantic", *Deep-Sea Research*, V. 30, No. 5A, pp. 475-511, 1983.
- Levine, M. D., and Richman, J. G., "Extracting the Internal Tide From Data: Methods and Observations From the Mixed Layer Dynamics Experiment", *Journal of Geophysical Research*, Vol. 94, No. C6, pp. 8125-8134, June 1989.
- Lindstrom, S. S. and Watts, R., "Vertical Motion in the Gulf Stream near 68° W", *Journal of Physical Oceanography*, V. 24, No. 11, pp. 2321-2333, November 1994.

- Linpack*, Argonne National Laboratories, University of New Mexico, 1978.
- Lynch, P. and Huang, X.-Y., "Initialization of the HIRLAM Model Using a Digital Filter", *Monthly Weather Review*, V. 120, No. 6, pp. 1019-1034, June 1992.
- Matlab, *Matlab User's Guide*, Version 4.2, The Mathworks, 1994.
- McCalpin, J. D., "On the Adjustment of Azimuthally Perturbed Vortices", *Journal of Geophysical Research*, Vol. 92, No. C8, pp. 8213-8225, July 1987.
- Noble M., Rosenfeld, L., Smith, R., Gardner, J. and Beardsley, R., "Tidal Currents Seaward of the Northern California Continental Shelf", *Journal of Geophysical Research*, Vol. 92, No. C2, pp. 1733-1744, February 1987.
- Nof, D., "On the β -Induced Movement of Isolated Baroclinic Eddies", *Journal of Physical Oceanography*, V. 11, pp. 1662-1672, December 1981.
- Nof, D., "On the Interaction between Thin Isolated Eddies and Longshore Currents", *Journal of Physical Oceanography*, V. 14, pp. 125-137, January 1984.
- Nuss, W. A., "Three Dimensional Meteorological Analysis Using Multiquadric Interpolation", paper accepted in *Intl. Jnl. Sci. Computing and Modeling*, 1994.
- Nuss, W. A., and Titley, D. W., "Use of Multiquadric Interpolation for Meteorological Objective Analysis", paper accepted in *Monthly Weather Review*, 1994.
- Paduan, J. D., and Niiler, P. P., "Structure of Velocity and Temperature in the Northeast Pacific as Measured with Lagrangian Drifters in Fall 1987", *Journal of Physical Oceanography*, V. 23, No. 4, pp. 585-600, April 1993.
- Pares-Sierra, A., White, W. B. and Tai, C.-K., "Wind-Driven Coastal Generation of Annual Mesoscale Activity in the California Current", *Journal of Physical Oceanography*, V. 23, No. 6, pp. 1110-1121, June 1993.
- Pauley, P. M., and Nieman, S. J., "A Comparison of Quasigeostrophic and Nonquasigeostrophic Vertical Motions for a Model-simulated Rapidly Intensifying Marine Extratropical Cyclone", *Monthly Weather Review*, V. 120, No. 7, July 1992.
- Pollard, R. T., and Regier, L. A., "Vorticity and Vertical Circulation at an Ocean Front", *Journal of Physical Oceanography*, V. 22, No. 6, June 1992.
- Pond, Stephen, and Pickard, George L., *Introductory Dynamical Oceanography*, Pergamon Press, 329 pp., 2nd Edition, 1983.

- Ramp, S. R., Jessen, P. F., Brink, K. H., Niiler, P. P., Dagget, F. L. and Best, J. S., "The Physical Structure of Cold Filaments Near Point Arena, California, During June 1987", *Journal of Geophysical Research*, V. 96, No. C8, pp. 14859-14883, August 1991.
- Rienecker, M. M., and Mooers, C. N., "Mesoscale Eddies, Jets and Fronts off Point Arena, California, July 1986", *Journal of Geophysical Research*, Vol. 94, No. C9, pp. 12555-12569, September 1989.
- Rosenfeld, L., "Baroclinic Semidiurnal Tidal Currents over the Continental Shelf off Northern California", *Journal of Geophysical Research*, Vol. 95, pp. 22153-22172, 1990.
- Schmitz, J. E. and Vastano, A. C., "Entrainment and Diffusion in a Gulf Stream Cyclonic Ring", *Journal of Physical Oceanography*, V. 5, No. 1, January 1975.
- Schuman, F. G., "Numerical Methods in Weather Prediction. II: Smoothing and Filtering", *Monthly Weather Review*, V. 85, pp. 357-361, 1957.
- Sirayanone, S., "Comparative Studies of Kriging, Multiquadric-Biharmonic, and Other Methods for Solving Mineral Resource Problems", PhD Dissertation, Department of Earth Sciences, Iowa State University, 1988.
- Smith, O. P., and Morrison, J. M., "Shipboard Acoustic Doppler Current Profiling in the Eastern Caribbean Sea, 1985-1986", *Journal of Geophysical Research*, Vol. 94, No. C7, pp. 9713-9719, July 1989.
- Sousa, F. M. and Bricaud, A., "Satellite-Derived Phytoplankton Pigment Structure in the Portuguese Upwelling Area", *Journal of Geophysical Research*, V. 97, No. C7, pp. 11343-11356, July 1992.
- Strass, Volker H., "Mesoscale Instability and Upwelling. Part 2: Testing the Diagnostics of Vertical Motion with a Three-Dimensional Ocean Front Model", *Journal of Physical Oceanography*, V. 24, pp. 1759-1782, August 1994.
- Swenson, M. S., Niiler, P. P., Brink, K. H., and Abbott, M. R., "Drifter Observations of a Cold Filament off Point Arena, California, in July 1988", *Journal of Geophysical Research*, V. 97, No. C3, pp. 3593-3610, March 1992.
- Viudez, A., Haney, R. L. and Tintore, J., "Diagnosis of Mesoscale Ageostrophic Motion Through Density Dynamical Assimilation: Application to the Alboran Sea", paper submitted to *Journal of Physical Oceanography*, April 1994.
- Walstad, L. J., Allen, J. S., Kosro, P. M., and Huyer, A., "Dynamics of the Coastal Transition Zone Through Data Assimilation Studies", *Journal of Geophysical Research*, V. 96, No. C8, pp. 14959-14977, August 1991.

INITIAL DISTRIBUTION LIST

Defense Technical Information Center Cameron Station Alexandria, VA 22304-6145	2
Library Code 52 Naval Postgraduate School 411 Dyer Rd. Rm 104 Monterey, CA 93943-5101	2
Oceanography Department Code OC/Bf Naval Postgraduate School 833 Dyer Rd. Rm 331 Monterey, CA 93943-5122	1
Dr. Roland W. Garwood, Jr. Code OC/Gd Naval Postgraduate School 833 Dyer Rd. Rm 308 Monterey, CA 93943	1
Dr. Robert L. Haney Code MR/Hy Naval Postgraduate School 589 Dyer Rd. Rm 252 Monterey, CA 93943-5114	3
Dr. Newell Garfield Code OC/Gf Naval Postgraduate School 833 Dyer Rd., Rm 342D Monterey, CA 93943	1
Dr. Peter C. Chu Code OC/Cu Naval Postgraduate School 833 Dyer Rd. Rm 342A Monterey, CA 93943	1

Dr. Charles W. Therrien 1
Code EC/Ti
Naval Postgraduate School
833 Dyer Rd. Rm 458
Monterey, CA 93943

Dr. Steven R. Ramp 1
Office of Naval Research
Code 322PO
800 N. Quincy St.
Arlington, VA 22217

Dr. Supachai Sirayanone 1
Code MR/Sy
Naval Postgraduate School
589 Dyer Rd. Rm 246
Monterey, CA 93943-5114

Dr. Leslie Rosenfeld 1
Code OC/Ro
Naval Postgraduate School
833 Dyer Rd. Rm 207
Monterey, CA 93943

Dr. Manuel Fiadeiro 1
Office of Naval Research
Code 322PO
800 N. Quincy St.
Arlington, VA 22217

Dr. Rolland Hardy 1
1213 Wanda Ave.
Seaside, CA 93955

Fundação Calouste Gulbenkian 1
Serviço de Bolsas de Estudo
Av. de Berna, 45-A
1093 Lisboa Codex
Portugal

Direcção do Serviço de Formação
Administração Central da Marinha
Rua do Arsenal
1100 Lisboa
Portugal

1

Director-Geral do Instituto Hidrográfico
Instituto Hidrográfico
Rua das Trinas, 49
1200 Lisboa
Portugal

2

LT Rogério P. Chumbinho
Instituto Hidrográfico
Rua das Trinas, 49
1200 Lisboa
Portugal

3